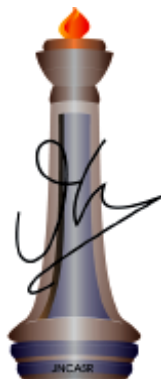

Supramolecular and Covalent Strategies to Control Pore Size, Polarity and Surface Charge of Mesoporous Silica

A Thesis Submitted for the Degree of

Doctor of Philosophy

By

B.V.V.S. Pavan Kumar



Chemistry and Physics of Materials Unit

Jawaharlal Nehru Centre for Advanced Scientific Research

(A Deemed University)

Bangalore - 560064 (INDIA)

September 2014

**Supramolecular and Covalent Strategies to
Control Pore Size, Polarity and Surface
Charge of Mesoporous Silica**

A Thesis Submitted for the Degree of

Doctor of Philosophy

By

B.V.V.S. Pavan Kumar

UNDER THE SUPERVISION OF

Prof. M. Eswaramoorthy

Chemistry and Physics of Materials Unit

Jawaharlal Nehru Centre for Advanced Scientific Research

(A Deemed University)

Bangalore-560064 (INDIA)

September 2014

DECLARATION

I hereby declare that the thesis entitled “*Supramolecular and Covalent Strategies to Control Pore Size, Philicity and Surface Charge of Mesoporous Silica*” is an authentic record of research work carried out by me at the Chemistry and Physics of Materials Unit, Jawaharlal Nehru Centre for Advanced Scientific Research, Bangalore, India under the supervision of **Prof. M. Eswaramoorthy** and that it has not been submitted elsewhere for the award of any degree or diploma.

In keeping with the general practice in reporting scientific observations, due acknowledgment has been made whenever the work described is based on the findings of other investigators. Any omission that might have occurred due to oversight or error in judgment is regretted.

B.V.V.S. Pavan Kumar



**Jawaharlal Nehru Centre for
Advanced Scientific Research**

Prof. M. Eswaramoorthy
Chemistry and Physics of Materials Unit
Jawaharlal Nehru Centre for Advanced
Scientific Research (JNCASR)
Bangalore-560064,India
Phone : +91 80 2208 2870
Fax: + 91 80 22082766
E-mail: eswar@jncasr.ac.in

Date

September 26, 2014

CERTIFICATE

I hereby certify that the work described in this thesis titled “*Supramolecular and Covalent Strategies to Control Pore Size, Philicity and Surface Charge of Mesoporous Silica*” has been carried out by **B.V.V.S. Pavan Kumar** at the Chemistry and Physics of Materials Unit, Jawaharlal Nehru Centre for Advanced Scientific Research, Bangalore, India under my supervision and it has not been submitted elsewhere for the award of any degree or diploma.

M. Eswaramoorthy

(Research Supervisor)

ACKNOWLEDGEMENTS

*During the course of my Ph.D., I have been helped by a large number of people, to whom I will always be grateful. Firstly, I would like to offer my most sincere thanks to one person who has stayed with me from the beginning to the end of Ph.D., my research supervisor, **Prof. M. Eswaramoorthy**. I am thankful to him for introducing me to the field of mesoporous silica and for giving me the freedom to work on various problems. His ever-enthusiastic nature, constant encouragement and support has helped me in successful completion of this work.*

*I would like to express my gratitude to **Prof. C. N. R. Rao, FRS** for being a constant source of inspiration. I am also grateful to him for creating such a vibrant research atmosphere to carry out this work.*

I thank the past and present chairmen of CPMU for allowing me to use the various facilities of the centre.

I am thankful to Prof. A. Sundaresan, Prof. S. Balasubramanian, Prof. U. V. Waghmare, Prof. S. M. Shiva Prasad, Prof. G. U. Kulkarni, Prof. T. K. Maji, Prof. C. Narayana, Prof. Subi J. George from JNCASR and Prof. N. Ravishankar from IISc for their coursework.

My special thanks to my labmates, The “Nanocat” group members: Dr. Dinesh, Dr. Sai Krishna, Dr. K.K.R. Datta, Josena, Piyush, Amrit, Sisir, Sonu and Dheeraj for their cooperation, useful discussions and for creating a friendly atmosphere in the lab. Working with them was a real pleasure.

It is a great pleasure to thank my collaborators: Prof. Subi J. George (JNCASR), Dr. Venkat (JNCASR) and Prof. Sampath (IISc) for fruitful collaborations.

I am thankful to my friends Mohit, Ankit, Chidambar, Satya, Nitesh, Urmi, Gayatri and Soumik for useful discussions.

I express my sincere thanks to all my teachers, especially from Sri Sathya Sai University, for their encouragement at various stages of my academic career.

I am thankful to the following people for various technical assistance: Mrs. Usha (TEM); Mrs. Selvi (FESEM); Mrs. Suma (Confocal microscopy); Mr. Mahesh (NMR); Mr. Vasu (UV, PL, IR, TGA); Mohit , Chidambar, Ankit and Bhawani (NMR); Prof. K. S. Narayan, Ravichandran and Raghesh (Voltammetry); Ritesh and Arpan (Vapor sorption); Shivakumar (HRMS).

I am grateful to Surya (SRF-2011,2012), Soumya (SRF-2012, 2013), Krishnachary (Project assistant) and Salim (POCE-2012) for working with me on various projects.

I am thankful to academic and administrative staff of JNCASR for their assistance.

I thank all my friends from JNCASR and RRI for their company in various activities.

Besides the research life, I am thankful to Prof. M. Eswaramoorthy and his family members for their hospitality and affection.

Financial assistance from Council of Scientific and Industrial Research (CSIR), India and Sheikh Saqr Junior Fellowship along with JNCASR is gratefully acknowledged.

A deep sense of gratitude to my family for their support, love and affection throughout my life.

Pavan

Preface

This thesis presents supramolecular and covalent strategies to control pore size, philicity and surface charge of mesoporous silica.

The thesis is divided into five Chapters.

Chapter 1 introduces the field of pore engineering in mesoporous silica with major emphasis given to pore structure, pore philicity and surface charge. An overview of the important developments in these areas of pore engineering and how they have found applications in a variety of fields is presented.

Chapter 2 introduces a non-covalent, reversible pore engineering approach through viologen-pyranine charge-transfer modules. The strong C-T interactions between pyranine and viologen were exploited to reversibly modify the pore size and philicity by employing alkyl derivatives of pyranine as donors. The fast binding of donors enabled quick and facile functionalization within minutes at room temperature. The modularity of the approach would allow modification of pores with custom designed compositions, components and functions.

Chapter 3, discusses the binding selectivity of different donors to the viologen acceptor immobilized on the walls of mesoporous silica. Very high adsorption selectivity factors in the range of around 45 were obtained for donors of similar charge but different charge-transfer strength. Even in flow based systems, 35% of its binding capacity was retained and a charge-transfer based breakthrough column was also fabricated to separate donors based on their charge-transfer strength. Breakthrough curves show clear separation for a three component mixture of donors of similar charge differing only in their charge-transfer strength. Non-polar environment around the viologen was found to play an important role in determining the binding selectivity.

Chapter 4, deals with surface charge reversal in mesoporous silica and is divided into three sub sections:

Chapter 4.1, discusses the application of viologen based charge transfer modules in electrostatic gating of ion transport through the nanochannels (<10 nm) in mesoporous silica. The polarity of ion transport was switched from anion selective to cation selective through ambipolar stage by controlling the extent of pyranine bound to the viologen. Further, the ion transport could be regulated with respect to pH by selecting a donor (coronene tetracarboxylate) with pH responsive functional groups. The modularity of this approach further allows facile integration of various

functional groups capable of responding to stimuli such as light and temperature to modulate the transport of ions as well as molecules.

Chapter 4.2 discusses the drawbacks of a supramolecular based strategy for charge reversal and presents a generic strategy to improve the strength of association in water based systems. Hydrophobic forces are used to improve the performance of C-T modules which are not capable of showing complete charge reversal within nanopores. The strong association aided by hydrophobic forces enabled the performance of supramolecular assemblies in achieving charge reversal and reduce the dependence on excess donors in solution.

In **Chapter 4.3**, we have shown a pH and glucose responsive charge-reversal on silica surface through heterogeneous functionalization utilizing amines and boronic acid moieties. The dual responsiveness of the charge reversal was unambiguously demonstrated through desorption of charged chromophores. A concentration dependent desorption response to glucose at physiologically relevant levels was also reported.

Chapter 5 deals with synthesis of Mesocellular hollow spheres have been synthesized using emulsion templates with a volatile solvent. Use of both octadecene and chloroform (volatile component) gave mesocellular hollow sphere whereas use of octadecene alone gave hollow spheres with no hierarchical structure. In order to enrich the functionality of the synthesized mesocellular hollow spheres, oil soluble magnetite nanoparticles (oleic acid capped) were also incorporated along with the emulsion templates. The obtained mesocellular spheres with magnetite nanoparticles entrapped would find applications in both drug delivery as well as in diagnosis (Magnetic Resonance Imaging). The described strategy can also be applied to incorporate quantum dots and gold nanoparticles to create a multifunctional composite.

TABLE OF CONTENTS

Declaration	i
Certificate	iii
Acknowledgments	v
Preface	vii
Table of contents	ix

CHAPTER-1

Introduction

Summary	1
1.1 Introduction	2
1.2 Pore Structure	2
1.3 Pore Philicity	4
1.4 Surface charge	6
1.5 References	10

CHAPTER-2

Charge-Transfer Modules for Reversible Pore Engineering in Mesoporous Silica

Summary	15
2.1 Introduction	16
2.2 Scope of the present investigation	17
2.3 Experimental section	18
2.4 Characterization	22
2.5 Results and discussion	22
2.6 Conclusions	35
2.7 References	35

CHAPTER-3

Selective Sequestration of Chromophores using Charge-transfer Interactions

Summary	39
3.1 Introduction	40
3.2 Scope of the present investigation	41
3.3 Experimental section	42
3.4 Characterization	44
3.5 Results and discussion	44

3.6	Conclusions	56
3.7	References	57

CHAPTER-4

Surface Charge Reversal

Chapter-4.1 *Supramolecular gating of Ion Transport in Nanochannels*

Summary		61
4.1.1	Introduction	62
4.1.2	Scope of the present investigation	62
4.1.3	Experimental section	64
4.1.4	Characterization	66
4.1.5	Results and discussion	66
4.1.6	Conclusions	79
4.1.7	References	80

Chapter-4.2 *A Generic Strategy to Improve the Non-covalent Gating of Ion Transport using Auxillary Hydrophobic Interactions*

Summary		83
4.2.1	Introduction	84
4.2.2	Scope of the present investigation	85
4.2.3	Experimental section	85
4.2.4	Characterization	86
4.2.5	Results and discussion	87
4.2.6	Conclusions	100
4.2.7	References	101

Chapter-4.3 *Glucose- and pH-Responsive Charge-Reversal Surfaces*

Summary		103
4.3.1	Introduction	104
4.3.2	Scope of the present investigation	104
4.3.3	Experimental section	105
4.3.4	Characterization	109
4.3.5	Results and discussion	109
4.3.6	Conclusions	118
4.3.7	References	118

CHAPTER-5***Synthesis of Mesocellular Hollow Spheres using Emulsion
Templates with a Volatile Component***

Summary		121
5.1	Introduction	122
5.2	Scope of the present investigation	123
5.3	Experimental section	123
5.4	Characterization	124
5.5	Results and discussion	124
5.6	Conclusions	129
5.7	References	129
	Conclusions and Future Outlook	131
	Comment on the nature of interaction between viologen and pyranine	132
	Appendix	133
	Curriculum vitae	135
	List of corrections	136

Chapter-1

Introduction

Summary

Ordered porous materials have found a variety of applications in various fields, such as adsorption, separation, catalysis, drug delivery, sensors, photonics, and nanodevices. The tailoring of the pore properties for such a wide range of applications has resulted in a surge of interest in pore engineering. This chapter introduces the field of pore engineering in mesoporous silica with major emphasis given to pore structure, pore philicity and surface charge. An overview of the important developments in these areas of pore engineering and how they have found applications in a variety of fields is presented.

1.1. Introduction

“Space — the final frontier” , the preface to a well-known television series not only captures the challenges encountered in space travel adventures, but also in the field of porous materials, whose mandates are to control the size, shape and regularity of the porous space and the atoms and molecules that define it. The past few decades have witnessed significant scientific advances in the fabrication of new ordered porous solids from a wide variety of materials. This has broadened the range of applications beyond their conventional use as catalysts/catalytic supports and adsorbents. It is to be noted that the term “ordered” in ordered porous materials, applies to the porosity of the material and does not necessarily imply that the materials have high structural order. These materials most commonly possess amorphous walls which enclose pore spaces which are arrayed in a regular fashion. MCM-41, is one very well-known example of such a material,^[1] which in spite of being made up of amorphous silica, exhibits a characteristic X-ray diffraction (XRD) pattern by virtue of its hexagonal array of mesopores.

There are four major classes of ordered porous materials – zeolites, ordered mesoporous materials (oxides, carbon, nitrides, etc.), metal organic frameworks and covalent organic frameworks. In this chapter, the focus will primarily be on the ordered mesoporous materials composed of oxides of silicon, commonly known as mesoporous silica. Mesoporous silica is generally obtained from the organic-inorganic assembly ^[2] of the silicate species produced by hydrolysis of silane precursors (tetraalkoxysilane) with soft matter like organic molecules or supramolecules (e.g. amphiphilic surfactants and bio-macromolecules) which act as structure directing agents. Surfactants are most commonly used as templates. The cooperative self-assembly between the surfactants and silicate species is driven by weak, non-covalent interactions such as hydrogen bonds, van der Waals forces and electrostatic interactions. Mesoporous silica is obtained on removal of the surfactant templates.

Pore engineering in mesoporous silica primarily deals with control of pore structure, pore philicity and surface charge. Surface charge in mesoporous silica can also be classified under pore philicity but has been given special mention due to the fact that surface charge in nanopores gives rise to a wealth of phenomena which find application in a variety of fields. The focus in this chapter is not on strategies of pore engineering but rather on how tuning of these pore properties has found different applications.

1.2 Pore Structure

Pore structure has typically been varied using different surfactant templates and hard templates. Use of a single surfactant gives monomodal pore systems where the pore size could

be varied by changing the size of the surfactant molecules. In the case of charged surfactants with alkyl tail groups, the increase in the chain length of the alkyl group increases the pore size.^[3] This tunability of pore size was used to control the amount of drug released and their release kinetics from within the pores.^[4] The kinetics of release and quantity of drug released were found to increase with pore size (Figure 1).

Use of dual surfactant templates allowed synthesis of mesoporous silica with bimodal pore size distribution. Dual-mesoporous silica spheres with core-shell structure having smaller pores (2.0 nm) in the shell and larger pores (~15 nm) in the core have been fabricated using an amphiphilic block copolymer (polystyrene-*b*-poly (acrylic acid), PS-*b*-PAA) and cetyltrimethylammonium bromide (CTAB) as co-templates (Figure 2a).^[5] Drug storage capacity and release profile could be efficiently modulated by changing the shell thickness. A shell thickness of around 60 nm, exhibited a three stage release profile (Figure 2b).

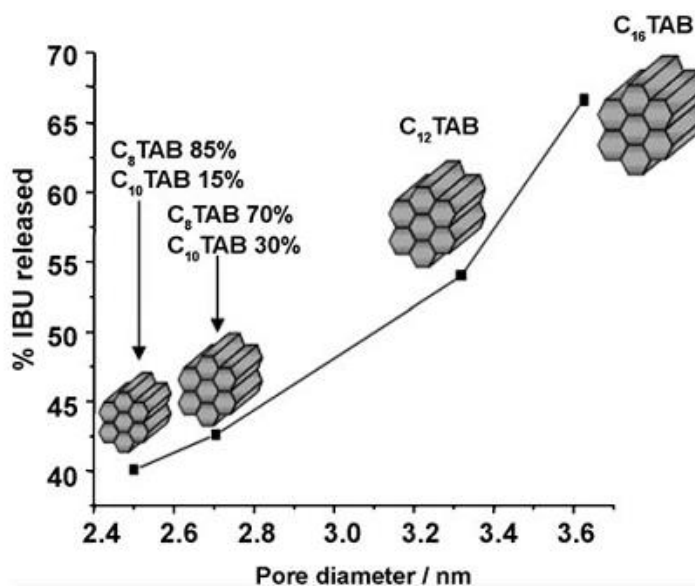


Figure 1. Monomodal/unimodal pore systems show increasing amount of drug release with increasing pore size. (Reproduced with permission from reference 4b)

Pore systems with hierarchical structure have also been synthesized which have a gradation of ordered porosity, whose dimensions lie in the different pore size regimes (micro-, meso-, macroporous), but the terminology has also been used for materials where some of the porosity may not be perfectly ordered, but which nonetheless, present a certain degree of structuring. In a hierarchical material each level of porosity serves a distinct purpose. Micropores can anchor catalytically active sites and immobilize small molecules. Mesopores provide faster access to the micropores and can also adsorb larger molecules. Macropores can enhance the diffusion properties of the material even further and could accommodate larger guests.

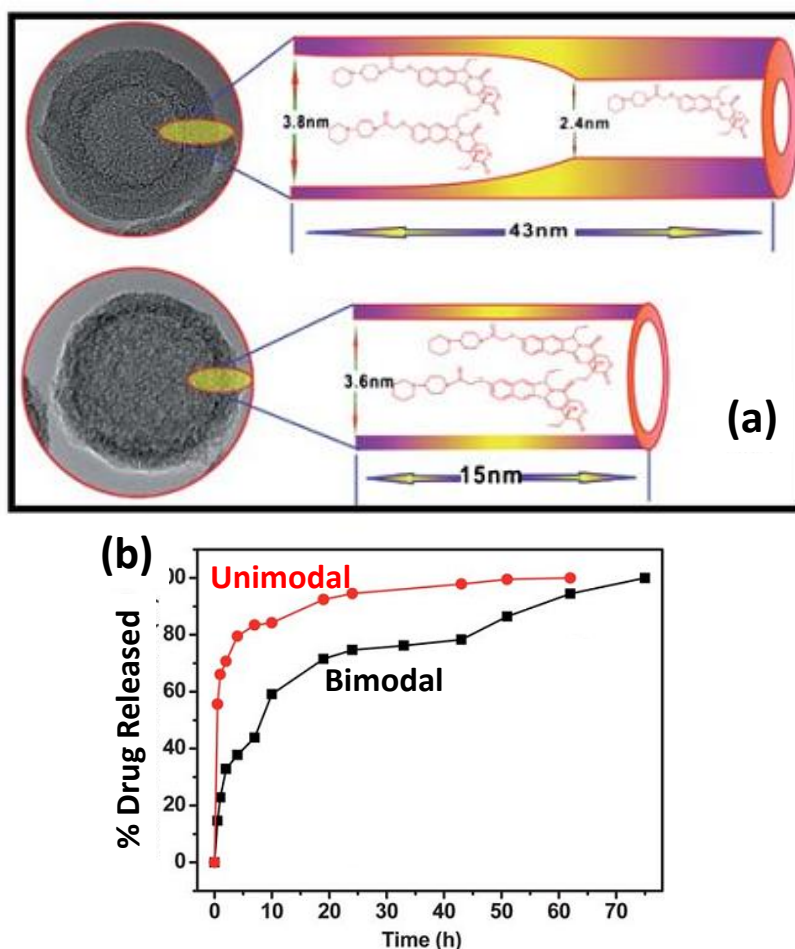


Figure 2. (a) Schematic of unimodal pore system showing a single pore size and bimodal pore system with larger pores in the core and smaller pores in the shell. (b) Drug release profiles of unimodal pore systems showing single step release and bimodal pore systems showing three stage release. (Reproduced with permission from reference 5b)

Dongyuan Zhao et al. have synthesized a hierarchical structured silica with mesopores and macropores using polymer colloidal crystals as hard template and Pluronic 123 as soft template^[6] (Figure 3a). The TEM image of the hierarchical material clearly shows the windows connecting macropores and the mesoporous nature of the walls (Figure 3b). By virtue of their hierarchical nature they could accommodate two different sizes of guests (cytochrome C and bovine serum albumin). Such hierarchical structuring has also been utilized in mesostructured zeolites for catalytic applications.

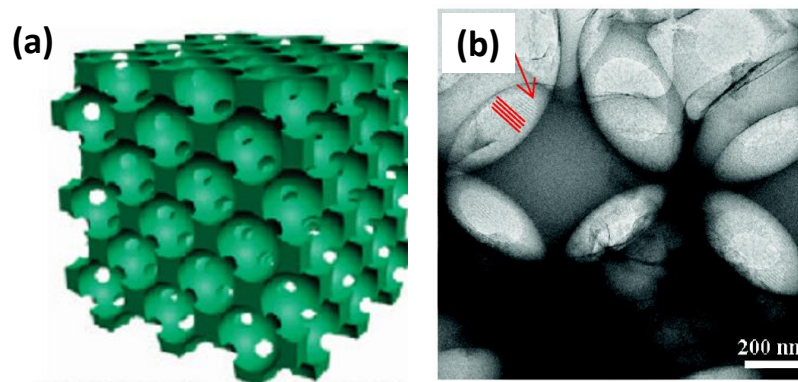


Figure 3. (a) Schematic of hierarchically structured mesoporous silica with macroporous structure and mesoporous walls. (b) TEM image showing the macropores, windows connecting the macropores and the mesoporous structure of the walls. (Reproduced with permission from reference 6)

1.3. Pore Philicity

Pore philicity has been conventionally engineered by incorporating various functional groups (organic or inorganic) to create specific interactions within the enclosed pore space. The incorporation of these functional groups in mesoporous silica has typically been achieved through three pathways^[7]:

a) Postsynthetic functionalization of silica (Grafting) - use of specialized silanes to post synthetically modify the surface.^[8]

b) Cocondensation - use of specialized silanes in the synthetic step along with conventional silane precursor, tetraethoxysilane.

c) Structural incorporation of organic linker (Periodic mesoporous organosilica^[9]) - use of bifunctional silanes to integrate organic groups not as pendants in the pore space but as linkers between the silica units, thus incorporating them into the framework of the wall itself.

The attachment of thiol^[10] and amine^[11] groups onto the pore surface enabled heavy metal ion sequestration. Amine immobilized mesoporous silica also found use as base catalysts^[12] in Knoevenagel condensation.^[13] Immobilization of sulfonic acid groups enabled their use as solid acid catalyst for aldol condensation, esterification^[14] and alkylation of phenols. Periodic mesoporous organosilica with phenyl linkers were found to be useful as good HPLC (high pressure liquid chromatography) stationary phases.^[15] They exhibited superior separation capability for mixtures of aromatic compound in comparison to conventional Nucleosil50-10 which is composed of normal silica (Figure 4).

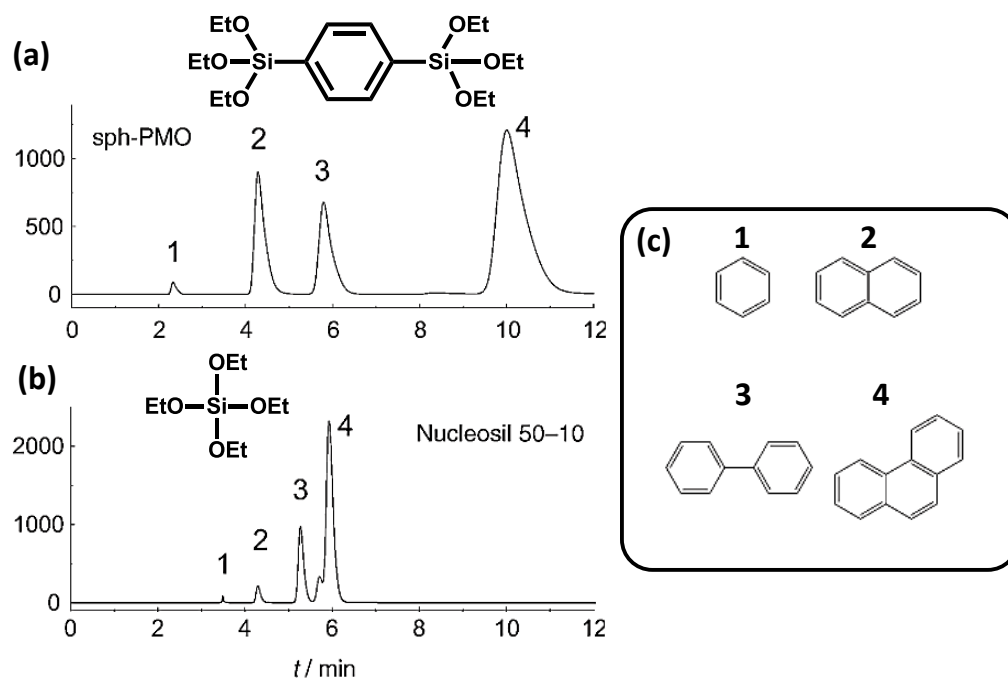


Figure 4. (a) Chromatograms showing better performance of phenylene bridged periodic mesoporous organosilica as HPLC stationary phase in contrast to the poor performance of (b) conventional HPLC stationary phase, Nucleosil 50-10, made from tetraethoxysilane precursor. (c) Chemical structures of the mixture of aromatic compounds used in the HPLC analysis. (Reproduced with permission from reference 15)

Mixed functionalization of the surface with different functional groups can give rise to interesting applications. The different functional groups can be randomly organized or can be spatially separated. The random organization has been found to be useful in cases where the two different functional groups can together exhibit cooperative catalysis.^[16] For example, thio and sulfonic acid groups were randomly functionalized on the pore surface for synthesis of ‘bisphenol A’ from acetone and phenol.^[17] Spatially separated functionalization has been found to be useful in fabrication of catalysts for tandem or cascade reactions.^[18] The asymmetric functionalization can also be used to create a hydrophilic/hydrophobic interface to enhance its use in catalysis which requires a hydrophilic/hydrophobic interface. For example, a mesoporous silica shell functionalized on the exterior with hydrophobic alkyl chains (Figure 5a) was found to exhibit greater yields for catalysis^[19] at the interface than regular organic micelle catalysts (Figure 5b). These structures have been rightly termed as “inorganic micelles” and they seem to hold promise for selective organic syntheses.

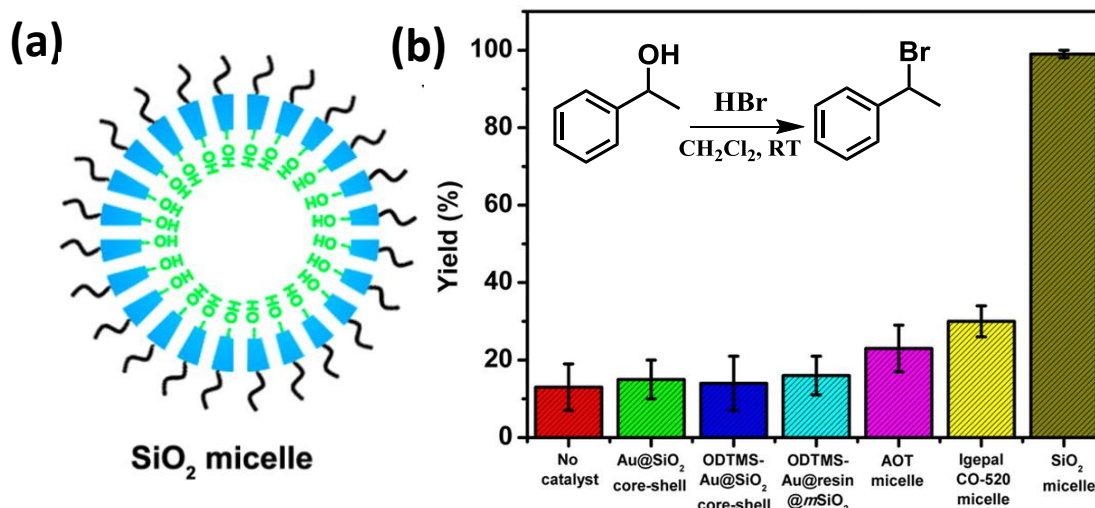


Figure 5. (a) Schematic showing the structure of SiO₂ inorganic micelles with a mesoporous silica shell functionalized on the exterior with hydrophobic alkyl chains giving a hydrophilic interior and hydrophobic exterior. (b) The yields of α -methylbenzyl bromide in the bromination of alcohols using HBr solution using various catalysts. It is important to note that the hydrophobic/hydrophilic interface is important and Au nanoparticles have no significant role to play. (Reproduced with permission from reference 19)

1.4. Surface charge

The surface charge within the mesopores plays a prominent role in defining the transport of ions through them, due to fact that the size of these nanopores/nanochannels^[20] is comparable to the Debye length.^[21] The electrostatic potential doesn't decay to the bulk values even at the centre of the nanopores which induces asymmetry in the ion distribution inside the nanopores (Figure 6a-d). The concentration of the counter-ions in nanopores is enhanced while the concentration of the co-ions is diminished due to the electrostatic repulsion between the ions and the charges on the surface of the nanopores (Figure 6e-f). The nanopores/nanochannel hence favors the passage of counter-ions, thus making them permselective with respect to ion transport properties. These unique properties open up a wide range of applications like electromechanical energy conversion,^[22] fabrication of abiotic analogues of membrane proteins,^[23] preconcentration of biomolecules^[24] and electrically mediated delivery.^[25]

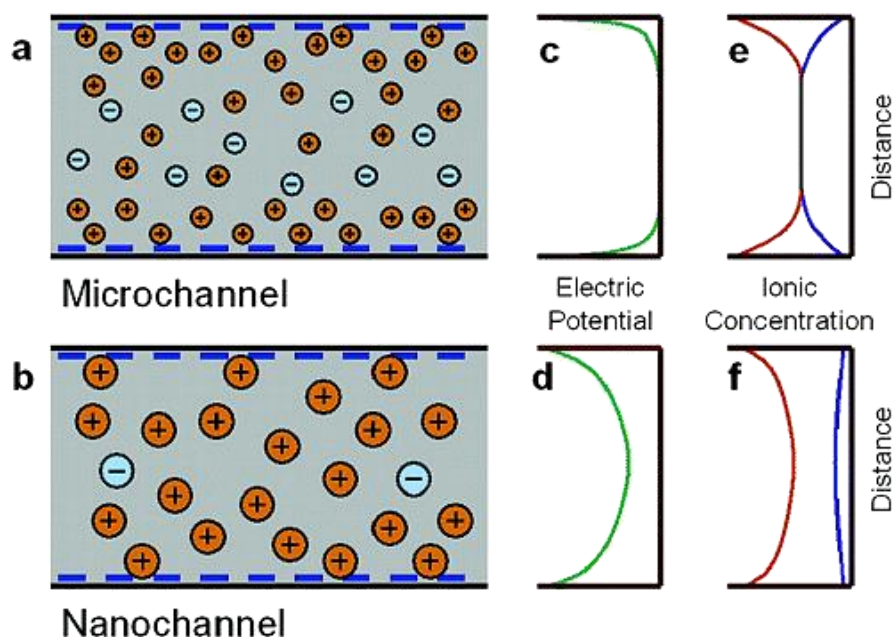


Figure 6. Schematic showing the distribution of ions (a) in a microchannel where most of the solution is neutral and (b) in a nanochannel which is almost unipolar in nature since its dimensions are smaller than the Debye length. The plot of electric potential along the cross section of a (c) microchannel showing rapid decay to its bulk value, and (d) in case of a nanochannel the electric potential even at the center of the nanochannel is influenced by the surface charge. The concentration of cations (orange) and anions (blue) in a (e) microchannel and a (f) nanochannel showing a deviation from bulk concentration with a much higher counterion concentration (orange) than the coion concentration (blue). (Reproduced with permission from reference 21)

The surface charge in nanopores has been typically controlled by attaching functional groups capable of charging and discharging in response to various stimuli like pH^[26] and light.^[27] Omar Azzaroni et al. have used polyelectrolyte brushes^[28] to modulate the surface charge inside the nanopores of SBA-16 to switch their ion permselective properties. Amine functionalization of the pores gave anion selective transport which on further modification with sulphonate brushes switched over to cation selective transport (Figure 7).

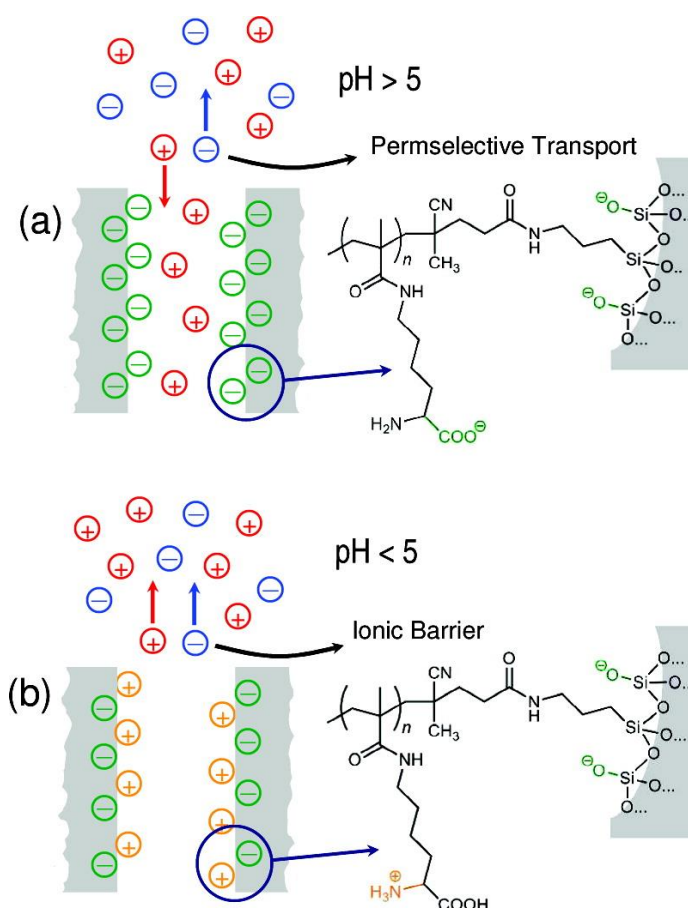


Figure 8. Schematic representation of the ion transport characteristics of the hybrid mesoporous silica film at different pH values: (a) $\text{pH} > 5$, cation selective transport and (b) $\text{pH} < 5$, ionic barrier (exclusion of ionic species). The expanded view of the pore wall shows both the polymer brushes and the surface silanols contributing to the surface charge of the nanopore. (Reproduced with permission from reference 29)

The surface charge in the nanopores can also be used to modulate the release kinetics of drug molecules which are charged. Chung-shi Yang et al. had partially functionalized the pore surface with trimethylammonium groups^[30] (Figure 9a). The positive charge of the trimethylammonium groups enabled adsorption of negatively charged drug molecules at pH 4-6 (Figure 9b). On raising the pH to 7, the negative charging of the silanol groups repelled the drug molecules causing a burst release (Figure 9c). On the other hand, under acidic conditions, slow release of drug occurred through ion exchange giving a sustained release response (Figure 9d). This would find application in oral drug delivery where the drug needs to be held back in acidic conditions of the stomach and released at a later stage in the alimentary canal.

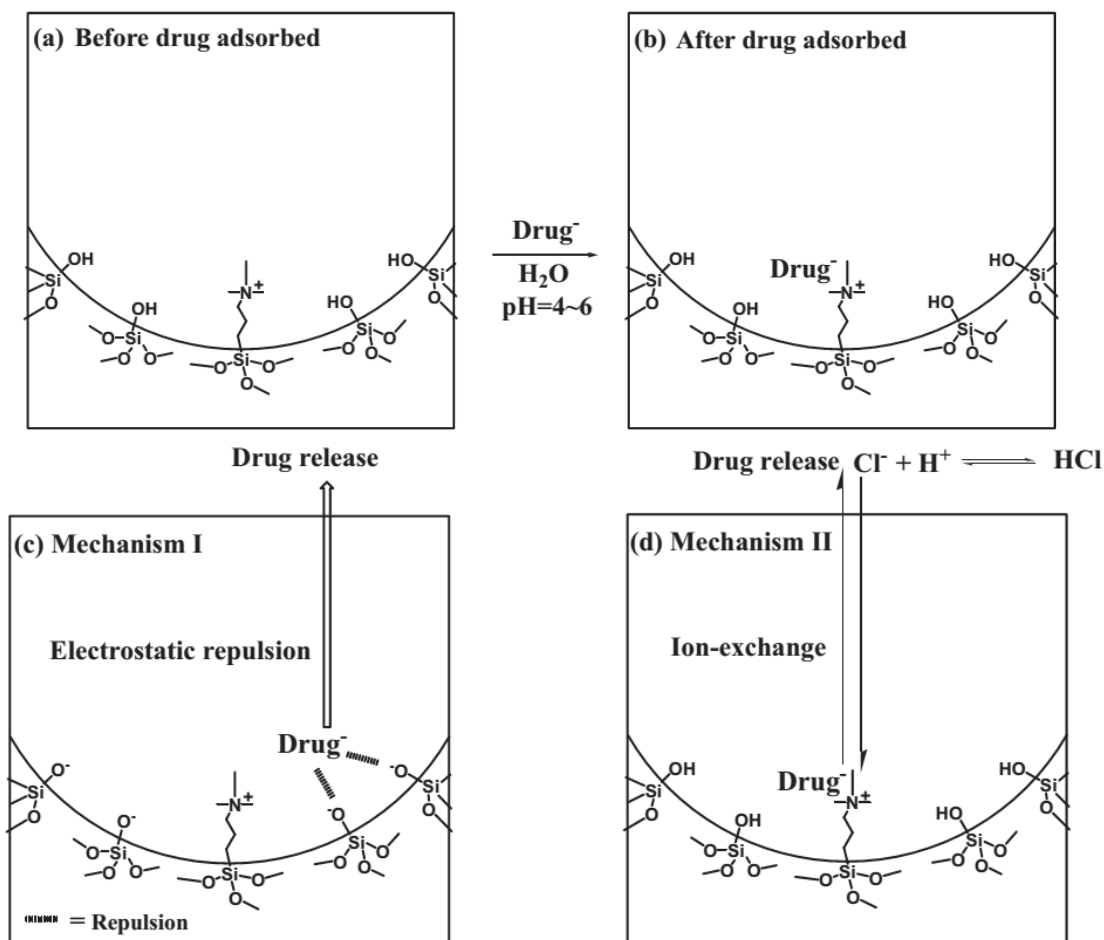


Figure 9. The schematic representation of the various release mechanisms of anionic drug adsorbed in mesoporous silica modified with trimethylammonium groups. a) Before adsorption of drug, b) after adsorption of drug, c) burst release of drug by electrostatic repulsion from the negatively charged silanols at neutral pH, and d) sustained release of drug by anion exchange. (Reproduced with permission from reference 30)

Thus, functionalization of mesoporous silica has broadened the scope of applications in various fields such as adsorption, separation, catalysis, photonics, sensors and drug delivery. Most of the approaches described above are covalent in nature and utilize the conventional silane strategy which modifies the pores irreversibly giving no room for further maneuverability with custom designed functionalities. In our work, as detailed in the later chapters, we try to explore the possibilities of a non-covalent route of functionalization for tuning the pore size, philicity and surface charge.

1.5. References

- [1] a) J. S. Beck, J. C. Vartuli, W. J. Roth, M. E. Leonowicz, C. T. Kresge, K. D. Schmitt, C. T. W. Chu, D. H. Olson, E. W. Sheppard, a. et, *J. Am. Chem. Soc.* **1992**, *114*, 10834-

- 10843; b) C. T. Kresge, M. E. Leonowicz, W. J. Roth, J. C. Vartuli, J. S. Beck, *Nature (London)* **1992**, 359, 710-712.
- [2] a) Q. Huo, D. I. Margolese, U. Ciesla, P. Feng, T. E. Gier, P. Sieger, R. Leon, P. M. Petroff, F. Schueth, G. D. Stucky, *Nature (London)* **1994**, 368, 317-321; b) Q. Huo, D. I. Margolese, U. Ciesla, D. G. Demuth, P. Feng, T. E. Gier, P. Sieger, A. Firouzi, B. F. Chmelka, a. et, *Chem. Mater.* **1994**, 6, 1176-1191; c) G. S. Attard, J. C. Glyde, C. G. Goltner, *Nature (London)* **1995**, 378, 366-368; d) A. Monnier, F. Schuth, Q. Huo, D. Kumar, D. Margolese, R. S. Maxwell, G. D. Stucky, M. Krishnamurty, P. Petroff, a. et, *Science (Washington, D. C., 1883-)* **1993**, 261, 1299-1303.
- [3] S. K. Jana, A. Mochizuki, S. Namba, *Catal. Surv. Asia* **2004**, 8, 1-13.
- [4] a) P. Horcajada, A. Ramila, J. Perez-Pariente, M. Vallet-Regi, *Microporous Mesoporous Mater.* **2004**, 68, 105-109; b) M. Vallet-Regí, F. Balas, D. Arcos, *Angew. Chem. Int. Ed.* **2007**, 46, 7548-7558.
- [5] a) D. Niu, Z. Ma, Y. Li, J. Shi, *J. Am. Chem. Soc.* **2010**, 132, 15144-15147; b) Y. Chen, H. Chen, M. Ma, F. Chen, L. Guo, L. Zhang, J. Shi, *J. Mater. Chem.* **2011**, 21, 5290-5298.
- [6] Z. Sun, Y. Deng, J. Wei, D. Gu, B. Tu, D. Zhao, *Chem. Mater.* **2011**, 23, 2176-2184.
- [7] F. Hoffmann, M. Cornelius, J. Morell, M. Fröba, *Angew. Chem. Int. Ed.* **2006**, 45, 3216-3251.
- [8] D. Bruhwiler, *Nanoscale* **2010**, 2, 887-892.
- [9] a) S. Inagaki, S. Guan, Y. Fukushima, T. Ohsuna, O. Terasaki, *J. Am. Chem. Soc.* **1999**, 121, 9611-9614; b) B. J. Melde, B. T. Holland, C. F. Blanford, A. Stein, *Chem. Mater.* **1999**, 11, 3302-3308; c) T. Asefa, M. J. MacLachlan, N. Coombs, G. A. Ozin, *Nature (London)* **1999**, 402, 867-871.
- [10] a) X. Feng, G. E. Fryxell, L.-Q. Wang, A. Y. Kim, J. Liu, K. M. Kemner, *Science* **1997**, 276, 923-926; b) L. Mercier, T. J. Pinnavaia, *Adv. Mater.* **1997**, 9, 500-503; c) J. Brown, R. Richer, L. Mercier, *Microporous Mesoporous Mater.* **2000**, 37, 41-48; d) A. Walcarius, C. Delacôte, *Chem. Mater.* **2003**, 15, 4181-4192; e) S. V. Mattigod, X.

- Feng, G. E. Fryxell, J. U. N. Liu, M. Gong, *Sep. Sci. Technol.* **1999**, *34*, 2329-2345; f) J. Liu, X. Feng, G. E. Fryxell, L.-Q. Wang, A. Y. Kim, M. Gong, *Adv. Mater.* **1998**, *10*, 161-165.
- [11] a) S. Hamid, W.-H. Syed, G.-M. Mohammad, *Chin. J. Chem.* **2009**, *27*, 915-919; b) A. Heidari, H. Younesi, Z. Mehraban, *Chemical Engineering Journal* **2009**, *153*, 70-79; c) M. Etienne, J. Bessiere, A. Walcarius, *Sensors and Actuators B: Chemical* **2001**, *76*, 531-538; d) T. Yokoi, H. Yoshitake, T. Yamada, Y. Kubota, T. Tatsumi, *J. Mater. Chem.* **2006**, *16*, 1125-1135.
- [12] D. J. Macquarrie, R. Maggi, A. Mazzacani, G. Sartori, R. Sartorio, *Applied Catalysis A: General* **2003**, *246*, 183-188.
- [13] D. J. Macquarrie, D. B. Jackson, *Chem. Commun.* **1997**, 1781-1782.
- [14] D. Das, J.-F. Lee, S. Cheng, *J. Catal.* **2004**, *223*, 152-160.
- [15] V. Rebbin, R. Schmidt, M. Fröba, *Angew. Chem. Int. Ed.* **2006**, *45*, 5210-5214.
- [16] E. L. Margelefsky, R. K. Zeidan, M. E. Davis, *Chem. Soc. Rev.* **2008**, *37*, 1118-1126.
- [17] R. K. Zeidan, V. Dufaud, M. E. Davis, *J. Catal.* **2006**, *239*, 299-306.
- [18] Y. Yang, X. Liu, X. Li, J. Zhao, S. Bai, J. Liu, Q. Yang, *Angew. Chem. Int. Ed.* **2012**, *51*, 9164-9168.
- [19] Q. Zhang, X.-Z. Shu, J. M. Lucas, F. D. Toste, G. A. Somorjai, A. P. Alivisatos, *Nano Lett.* **2013**, *14*, 379-383.
- [20] a) W. Sparreboom, A. van den Berg, J. C. T. Eijkel, *Nat Nano* **2009**, *4*, 713-720; b) D. Stein, M. Kruithof, C. Dekker, *Phys. Rev. Lett.* **2004**, *93*, 035901; c) K. Zhou, J. M. Perry, S. C. Jacobson, *Annual Review of Analytical Chemistry* **2011**, *4*, 321-341.
- [21] R. Karnik, R. Fan, M. Yue, D. Li, P. Yang, A. Majumdar, *Nano Lett.* **2005**, *5*, 943-948.
- [22] H. Daiguji, P. Yang, A. J. Szeri, A. Majumdar, *Nano Lett.* **2004**, *4*, 2315-2321.
- [23] M. Li, R. L. Harbron, J. V. M. Weaver, B. P. Binks, S. Mann, *Nat Chem* **2013**, *5*, 529-536.
- [24] Y.-C. Wang, A. L. Stevens, J. Han, *Anal. Chem.* **2005**, *77*, 4293-4299.

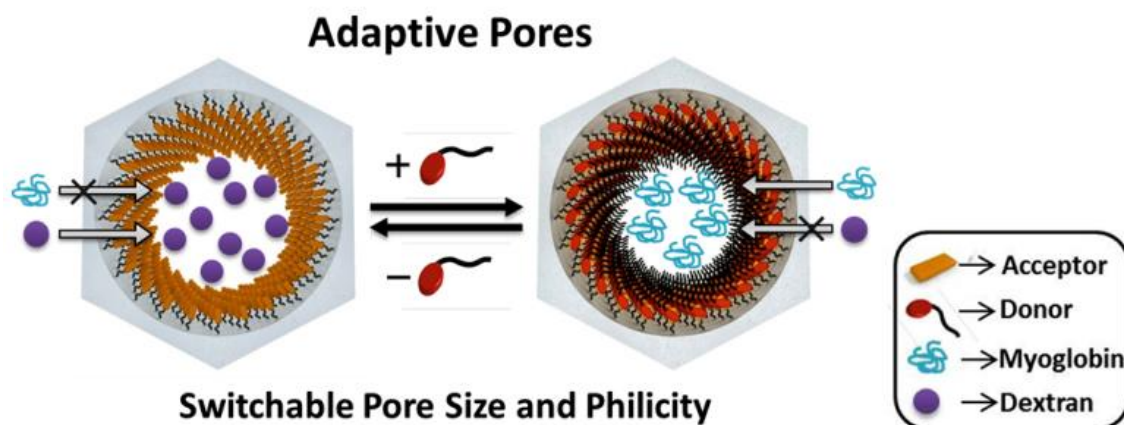
- [25] K. Tybrandt, E. O. Gabrielsson, M. Berggren, *J. Am. Chem. Soc.* **2011**, *133*, 10141-10145.
- [26] a) B. Yameen, M. Ali, R. Neumann, W. Ensinger, W. Knoll, O. Azzaroni, *Nano Lett.* **2009**, *9*, 2788-2793; b) M. Ali, P. Ramirez, S. Mafé, R. Neumann, W. Ensinger, *ACS Nano* **2009**, *3*, 603-608; c) S. B. Lee, C. R. Martin, *Anal. Chem.* **2001**, *73*, 768-775; d) B. Yameen, M. Ali, R. Neumann, W. Ensinger, W. Knoll, O. Azzaroni, *J. Am. Chem. Soc.* **2009**, *131*, 2070-2071.
- [27] a) A. Brunsen, J. Cui, M. Ceolin, A. d. Campo, G. J. A. A. Soler-Illia, O. Azzaroni, *Chem. Commun.* **2012**, *48*, 1422-1424; b) L. Wen, Q. Liu, J. Ma, Y. Tian, C. Li, Z. Bo, L. Jiang, *Adv. Mater.* **2012**, *24*, 6193-6198; c) G. Wang, A. K. Bohaty, I. Zharov, H. S. White, *J. Am. Chem. Soc.* **2006**, *128*, 13553-13558; d) M. Zhang, X. Hou, J. Wang, Y. Tian, X. Fan, J. Zhai, L. Jiang, *Adv. Mater.* **2012**, *24*, 2424-2428.
- [28] A. Calvo, B. Yameen, F. J. Williams, O. Azzaroni, G. J. A. A. Soler-Illia, *Chem. Commun.* **2009**, 2553-2555.
- [29] A. Calvo, B. Yameen, F. J. Williams, G. J. A. A. Soler-Illia, O. Azzaroni, *J. Am. Chem. Soc.* **2009**, *131*, 10866-10868.
- [30] C.-H. Lee, L.-W. Lo, C.-Y. Mou, C.-S. Yang, *Adv. Funct. Mater.* **2008**, *18*, 3283-3292.

Chapter-2

Charge-Transfer Modules for Reversible Pore Engineering in Mesoporous Silica

Summary

Mesoporous silicas form an important class of nanoporous materials complementary to their microporous analogues with large pore size, fast molecular transport and chemically modifiable surface. However, the chemical modification is largely restricted to covalent silane strategy leading to irreversible functionalization. Herein, we introduce a non-covalent pore engineering approach to achieve exceptional reversibility in functionalization through viologen-pyranine charge-transfer modules. By employing alkyl derivatives of pyranine as donors we could exploit the strong C-T interactions between pyranine and viologen to reversibly modify the pore size and philicity. The fast binding of donors enables quick and facile functionalization within minutes at room temperature. The modularity of the approach enables modification of pores with custom designed compositions, components and functions.



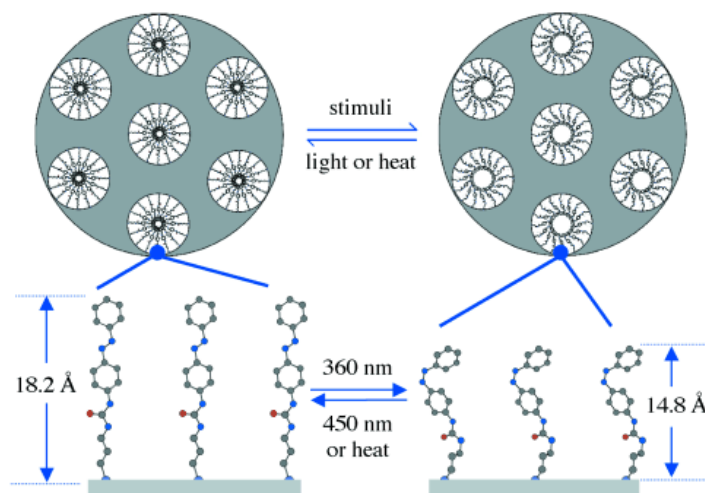
Publication based on this work has appeared in *J. Am. Chem. Soc.*, **2013**, 135, 10902.

2.1. Introduction

Functionalized mesoporous silicas have generated a great deal of attention by virtue of their application in catalysis^[1], adsorption^[2], drug delivery^[3], sensing^[4] and separation^[5]. Pore engineering is of paramount importance in realising many of their applications in the frontier areas and has been focus of research for quite some time now.^[6] It involves control of both pore size and philicity. Pore size has been controlled primarily through the synthetic approach. The synthesis relies on self-assembly of the liquid crystal /block copolymer template with silica precursors to form the mesostructured material.^[7] The pores are constituted by the empty space generated on removal of the template. Hence the pore size was controlled by varying the surfactant chain length^[8] as well as by use of pore swelling agents. In the case of block copolymer (PEO-PPO-PEO) templated mesoporous silicas like SBA-15,^[9] hydrothermal treatment temperature played a major role in defining the pore size and also the thickness of the pore wall. The PEO block of the template becomes more hydrophobic with increase in temperature due to which the hydrophobic domains grow larger resulting in increase in pore size.^[10] The increase in hydrothermal temperature from 35 °C to 150 °C changes the pore size from 6.8 nm to 13.2 nm^[11] (Figure 1a). To increase the pore diameter to 30 nm and beyond, pore swelling agents like trimethylbenzene (TMB) were used.^[11] These pore swelling agents localise in the hydrophobic core of template to increase its volume and thus increase the pore size. Pore size is controlled by varying the ratio between the pore swelling agent (auxillary organics) and the surfactant template. Controlled silanization was also recently used to achieve angstrom precision in controlling pore size.^[12] Pore philicity, on the other hand was primarily modulated using grafting^[13] or co-condensation^[6c] approach. In grafting, silanes are used to post synthetically modify the pore surface and in co-condensation, the silane is condensed along with the silica precursor during the synthesis. More recently, periodic mesoporous organosilicas^[14] (PMO) have been synthesised wherein the bis-silanes are used to condense around the template. The bis-silane has an organic functional linker between the silane moieties and hence in this case the functional groups are everywhere in the walls rather than just at the surface like in grafting and cocondensation. Most of these approaches to control pore size and philicity are passive, i.e. they cannot respond to stimuli or be modified after synthesis. On the other hand, use of active functionalities capable of responding to different stimuli leave room for post synthetic flexibility to modulate pore properties.

The immobilisation of active functionalities onto mesoporous silica would enable dynamic control of the pore properties using external stimuli like light, temperature and pH. Brinker et al. functionalised the pores with azobenzene moieties to control the pore size and philicity in response to light (Scheme 1).^[15] This enabled photoregulation^[16] of mass transport through the pores. Garcia et. al. synthesised a PMO with 1,2-bis(4-pyridyl)ethylene as the

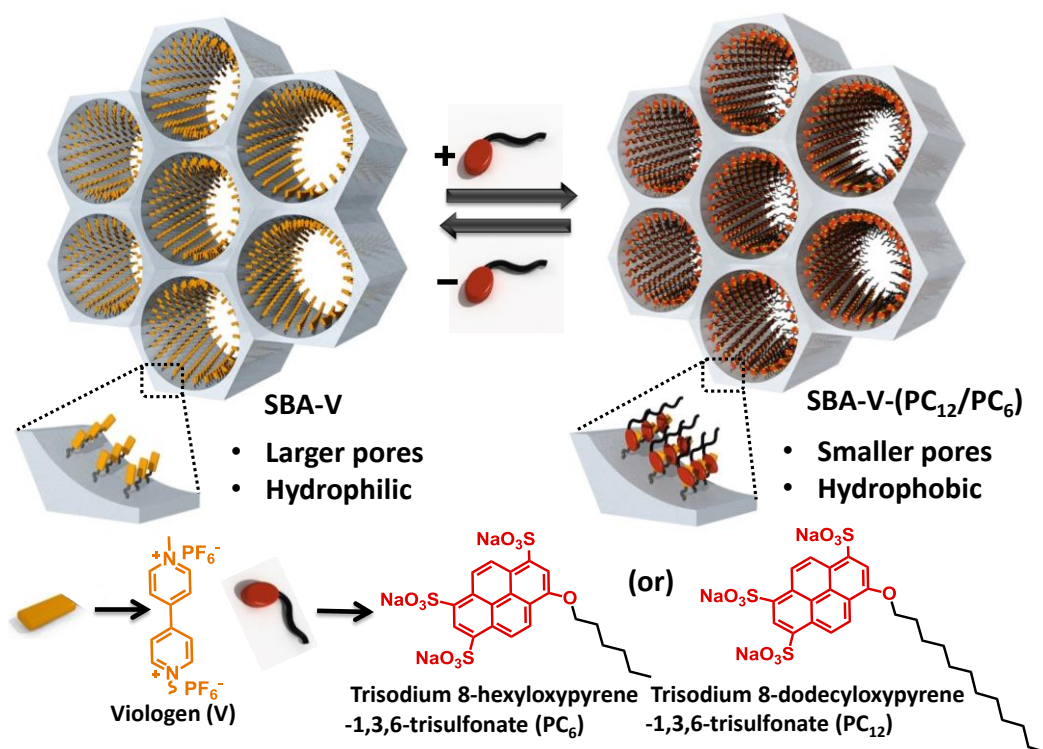
organic linker to actively control the pore volume and surface area.^[17] The active functionalities used so far, confer two state flexibility, i.e. they switch between two states to control the properties of the pore. In order to further increase the flexibility of control it is necessary to have a modular design where the components can be assembled reversibly in multiple ways.



Scheme 1. Photoresponsive composites prepared by Brinker et al. showing change in pore size on irradiation with light. (Reproduced with permission from reference 15)

2.2. Scope of the present investigation

As a proof of concept, we used non-covalent charge-transfer (C-T) interactions^[18] between donor-acceptor molecules as a means to reversibly modify the nature of the pores of mesoporous silica, SBA-15^[9](SBA). Viologen, an electron acceptor, was first directly linked to the pore walls of SBA-15 through silane chemistry and then by employing pyranine and its hexyl (PC₆) and dodecyl (PC₁₂) substituted derivatives as donors, we were able to show the change in pore size and philicity of functionalized mesoporous silica (Scheme 2). The fast kinetics of binding enabled facile functionalization by simple room temperature soaking in the donor solution for a few minutes. Remarkable reversibility of functionalization was also demonstrated by the removal of donor molecules by breaking the C-T interactions through the reduction of viologen. The key to successful non-covalent modification of surfaces lies in the strength of the binding between the non-covalent motifs. The viologens immobilized on the mesoporous silica surface show Langmuir binding constants (10^5 - 10^6 M⁻¹) one-to-two orders in magnitude greater than their solution state analogues which enabled strong and stable supramolecular functionalization. The non-covalently modified pores show selectivity for hydrophilic and hydrophobic macromolecules depending upon the philicity of non-covalent motif used.



Scheme 2. Non-covalent functionalization of viologen modified mesopores of SBA-15 with pyranine derivatives to reversibly engineer the pore environment. Hexyl and dodecyl derivatives of pyranine have been used to complex with viologen to modify the pore wall with alkyl chains to vary the pore size as well as philicity. Reversibility of this modular approach was shown by the reduction of viologen moieties to break the charge-transfer interactions between pyranine and viologen enabling re-engineering of the pore.

2.3. Experimental section

Synthesis of viologen functionalized SBA

(i) Iodopropyl functionalized SBA (SBA-I). Monodispersed SBA-15 (referred as SBA) rods were synthesized using a reported procedure^[19]. 1 g of calcined mesoporous silica rods were degassed and then hydrated in a controlled fashion till the relative humidity of 50% and added into degassed toluene along with 2.5 ml (12.7 mmol) of (3-iodopropyl)trimethoxysilane (IPTMS) and stirred overnight. The experimental setup used for the controlled hydration of SBA has been discussed separately below. The temperature was increased to 110 °C and held for 6 h to complete the reaction. The obtained SBA-I was washed with toluene (3×40 ml), and ethanol (1×40 ml) and finally subjected to soxhlet extraction in ethanol to completely wash away uncondensed silane from the pores.

Controlled hydration of SBA. A simple apparatus^[20] was used to hydrate mesoporous silica, SBA, in a precise and controlled fashion. A two necked round bottom flask, half filled with

water was connected to a nitrogen line through a gas adaptor on one end and a specially fabricated glass apparatus with a frit on the other end (Figure 1). The degassed SBA to be hydrated was placed on the frit and nitrogen was passed (100 ml min^{-1}) over the water through the frit to hydrate the SBA. The humidity of the gas exiting the setup was monitored using a humidity meter. Initially, the humidity level of the gas falls to around 25-30 % RH on passing through the degassed SBA. As more gas passes through the SBA, the humidity levels rises slowly as the surface of SBA is slowly getting saturated with adsorbed water vapor. When the humidity reached the desired level, the nitrogen flow was discontinued and the hydrated silica was immediately transferred into toluene to prevent change in its state of hydration.

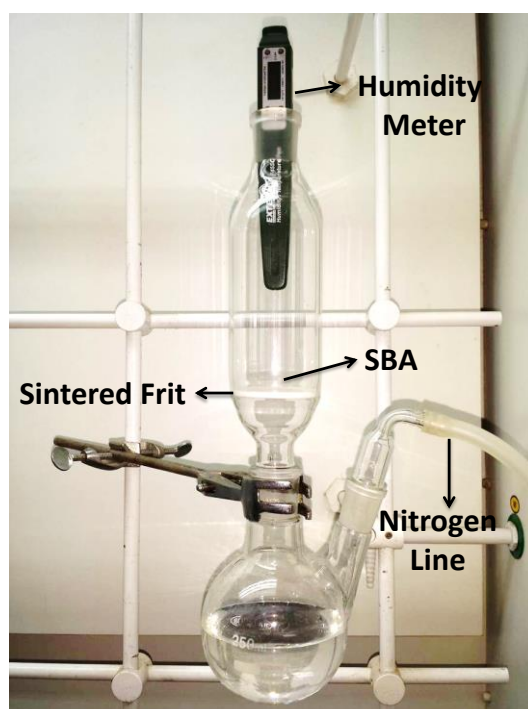


Figure 1. Digital photography image showing the experimental setup used for hydration of SBA.

(ii) Viologen functionalized SBA (SBA-V). 1 g of SBA-I degassed at $80 \text{ }^\circ\text{C}$ for 6 h was added to 120 ml of degassed CH_3CN (purged with argon for 15 minutes) along with 2.5 g (8.3 mmol) of N-methyl-4,4'-bipyridinium iodide and refluxed for 3-4 days. The SBA-V obtained was washed with CH_3CN ($2 \times 40 \text{ ml}$), water ($2 \times 40 \text{ ml}$) and finally ethanol. It was subjected to ion exchange by stirring with 50 ml of 0.5 M ammonium hexafluorophosphate solution for 5 h at room temperature and then raising the temperature to $60 \text{ }^\circ\text{C}$ for 0.5 h. It was then washed with water ($3 \times 40 \text{ ml}$), and ethanol ($1 \times 40 \text{ ml}$) and dried at $80 \text{ }^\circ\text{C}$.

Synthesis of ionic hybrid control (SBA-B)

1 g of SBA-I degassed at 80 °C was added to 50 ml of degassed acetonitrile along with 0.93 g (8.3 mmol) of 1,4-diazabicyclo[2.2.2]octane (DABCO) and refluxed for 3-4 days (8 mmol of a quaternary ammonium salt was also added). It was then washed with excess acetonitrile and then reacted with excess methyl iodide (40 mmol) in 25 ml acetonitrile for 6 h at 60 °C to obtain SBA-B. Protocol for workup was similar to SBA-V.

Hexyl functionalized SBA (SBA-C₆)

0.5 g of degassed SBA at 80 °C was added into 50 ml of n-hexane under a nitrogen blanket along with 1 g of hexyltrichlorosilane and stirred at room temperature for 24 h. It was then washed thoroughly with hexane and dried at 60 °C.

Digestive estimation of viologen

Loading of viologen in SBA-V was determined by UV-visible spectroscopy as follows. 4 mg of SBA-V and 15 mg of NH₄F was heated at 50 °C for 3 h in 1 ml of conc. aq. HCl (11 M), and diluted to 40 ml with water for UV-visible spectroscopy in 1 cm cell at 258 nm. A calibration curve at [1 to 10] x 10⁻⁵ M range for viologen was prepared by treating methyl viologen ($\lambda_{\max} = 258 \text{ nm}$, $\epsilon = 17600 \text{ M}^{-1}\text{cm}^{-1}$) under similar conditions as used for digestion of SBA-V.

Donor binding studies

(i) Binding titration. 15 mg of SBA-V or SBA-B was weighed into separate vials. Increasing amounts of pyranine were added into the vials and the volume was made up to 5 ml. They were stirred for 4 h, centrifuged and the supernatant analysed using UV-Vis spectroscopy to determine the amount of donor left behind in the solution. The supernatant containing pyranine was analyzed with the use of a calibration curve at [1 to 5] x 10⁻⁴ range ($\lambda_{\max} = 403 \text{ nm}$, $\epsilon = 2300 \text{ M}^{-1}\text{mm}^{-1}$). From this, the amount of donor taken up by SBA-V or SBA-B was back calculated.

(ii) Competitive binding (SBA-V vs. methyl viologen in solution). 15 mg of SBA-V was added to a pre-complexed solution of methyl viologen (8.4 μmol) and pyranine (4 μmol) and stirred for 4 h. The supernatant was then analysed using UV-Vis spectroscopy.

Langmuir model for calculating binding constant

To calculate the binding constant for the interaction of pyranine with SBA-V, Langmuir model of adsorption was used. Langmuir model is a good approximation in this case because of the following reasons:

1. The interaction between viologen and pyranine is very specific and hence a monolayer adsorption model taking into account strong binding interactions between the adsorbent and adsorbate would be ideal.
2. Though the approximation of uniformity of binding sites is not realistic in case of functionalized silica where clustering of silanes functionalization^[21] is known, but it would serve to provide a mean value which could be of significance.

The model doesn't take into account the adsorbate-adsorbate interactions which in this case are strong due to the charged nature of pyranine. Regardless, we chose to use it to gain a rough estimate of the binding constant.

The Langmuir binding constant is calculated by plotting the inverse of the amount adsorbed against the inverse of the concentration of the adsorbate at equilibrium in solution. The intercept of this plot divided by the slope gives the Langmuir binding constant. The Langmuir equation for the adsorption from solution is:

$$\frac{1}{x} = \frac{1}{Kcx_m} + \frac{1}{x_m}$$

x – Moles adsorbed per gram of adsorbate

x_m – Moles adsorbed for one monolayer per gram of adsorbate

K – Binding constant

C – Concentration of the adsorbate in equilibrium

Reversible non-covalent functionalization

The donors for non-covalent functionalization were prepared by following a reported procedure^[22] and purified using HPLC. 50 mg of SBA-V was stirred with 1.35 ml of 10 mM solution of donor (PC₆ or PC₁₂) for 4 h and centrifuged and washed twice with water to remove unbound donors. To regenerate SBA-V, a solution of sodium dithionate (60 mM) and sodium sulphate (0.5 M) at pH 8.2 was used as reducing agent to break the C-T and wash away the donors. After 3-4 washings, oxygen was bubbled for a minute through the dispersion to reform viologen on the pore walls. Alternatively, a milder oxidising agent, K₃[Fe(CN)₆], can be used to oxidise the viologen radical cation back to viologen without any degradation of viologen. For the complete removal of donors from SBA-V, a column based strategy was applied wherein the SBA-V to be regenerated is packed into a column and the solution of sodium dithionate and sodium sulphate was passed until the donor levels in the eluent were sparingly small. A degassed 10 mM solution of K₃[Fe(CN)₆] was eluted through the column to oxidise the

viologen radical cation into viologen. The retention of the active viologen moieties after every reduction-oxidation cycle was confirmed via pyranine binding capacity. The pore size was measured through nitrogen adsorption isotherms after every addition and removal of PC₆ with a correction made for exposure of SBA-V to the buffer.

Macromolecule Adsorption

(i) Individual adsorption. 15 mg of SBA-V, SBA-V-PC₆, SBA-C₆ and SBA-V-PC₁₂ were weighed into separate vials and 3 mg of macromolecules (dextran^[23] or myoglobin^[24]) were added and the volume was made up to 3 ml using 25 mM phosphate buffer (pH = 7.2) solution. They were stirred with the macromolecule solutions for a period of 48 h at 25 °C and the extent of sorption was determined by spectroscopic analysis of the supernatant at the absorption maxima of the macromolecules (myoglobin-409 nm, FITC-dextran-493 nm). HPLC (High pressure liquid chromatography) was also carried out to analyze the amount of myoglobin left in the supernatant.

(ii) Mixed Adsorption. 3 mg of both dextran and myoglobin were added into vials containing 15 mg of SBA-V, SBA-V-PC₆, SBA-C₆ or SBA-V-PC₁₂ and the volume was made up to 3 ml using 25 mM phosphate buffer (pH=7.2) solution. Rest of the protocol is same as the individual adsorption studies.

2.4. Characterization

Please refer to the appendix for the instrumental details of UV-visible spectroscopy, X-ray diffraction, Field emission scanning electron microscopy (FESEM), infra-red spectroscopy, nitrogen sorption analysis and thermogravimetric analysis.

2.5. Results and discussion

Short SBA rods of size 1-2 μm have been synthesised using a non-ionic block copolymer, P123 as surfactant template at 130 °C following a reported procedure^[19] (Figure 2). The as-prepared SBA rods were extracted for 48 h with ethanol using a soxhlet apparatus to remove the P123 surfactant templates. High temperature calcination pathway to remove surfactant templates was not used since calcined SBA have poor silanol density which are not favourable for post synthetic functionalization. The pores were functionalized with (3-iodopropyl)trimethoxysilane through surface polymerization approach^[25] to form SBA-I. This involves pre-hydration of the SBA before silanization in order to aid the controlled hydrolysis of the silane to form a self-assembled monolayer of the silane on the surface of the pores. The pre-hydration of SBA (before iodopropyl silanization) was carried out by passing nitrogen saturated with water vapour through the sample (see experimental section). The degree of

hydration of SBA was controlled by stopping the flow of nitrogen saturated with water vapour once the humidity level in the sensor reached the desired level (40 %, 50 % or 80 %). The silanization of SBA was carried out over the samples hydrated upto 40 %, 50 % and 80 % relative humidity (RH) to understand the effect of hydration on the extent of iodopropyl functionalization. The functionalization of the pores with and without hydration treatment was followed by using nitrogen adsorption isotherms recorded at 77 K (Figure 3a). All the nitrogen adsorption isotherms were of type IV according to the IUPAC classification^[26] and are characteristic of mesoporous materials with a narrow pore size distribution.^[27] The pore size distributions calculated using the Barrett-Joyner-Halenda (BJH) method^[28] show a decrease in pore size on functionalization with iodopropylsilane (Figure 3b). The more the functionalization density the smaller the pore size of the functionalised SBA. The decrease in pore size almost leveled off at SBA hydrated upto 50 % RH before functionalization. The SBA pre-hydrated to 80 % RH, resulted only in a small decrease in pore size on iodopropyl silanization. In order to avoid the vertical polymerisation^[20] of silane on pore surfaces due to excess hydration, SBA-I synthesised from SBA pre-hydrated upto 50 % RH was used for further functionalization.

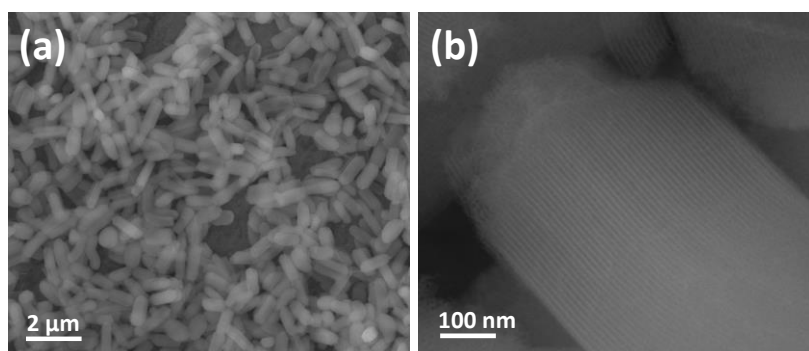


Figure 2. FESEM images of SBA-15 at (a) low magnification showing monodisperse short rod like morphology, and (b) high magnification showing the structurally ordered mesopores.

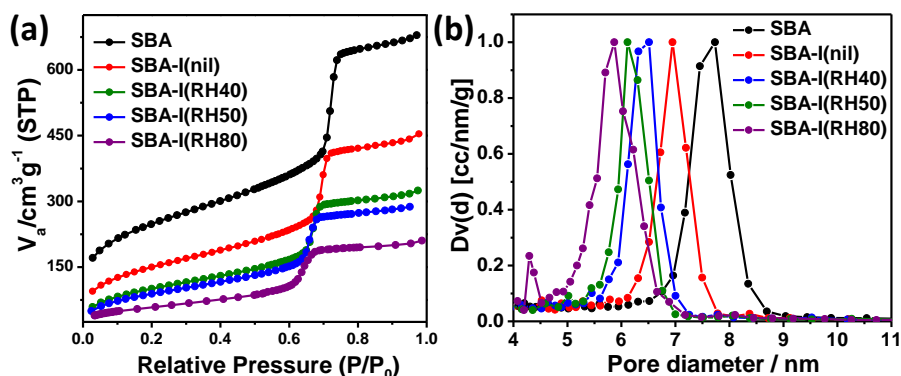
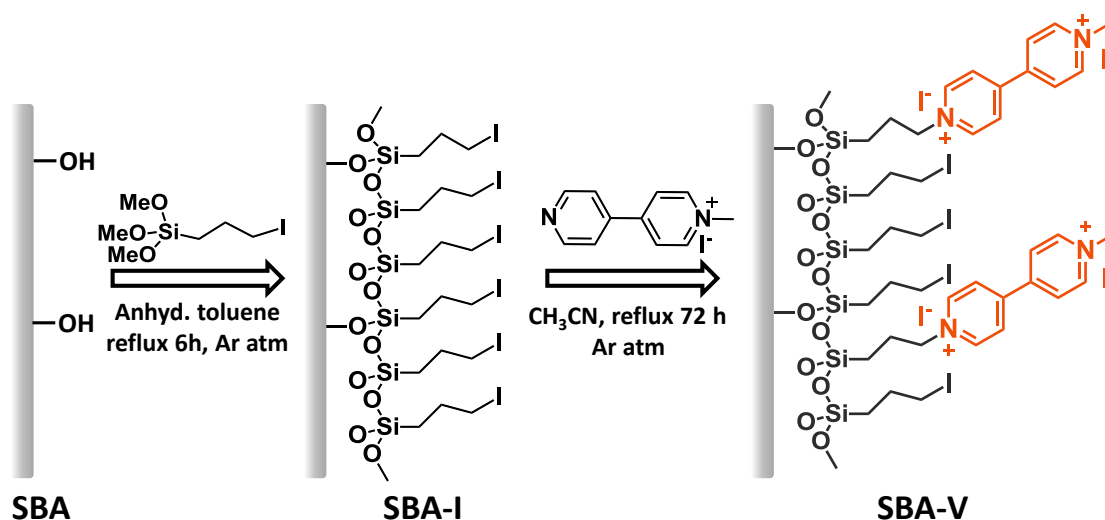


Figure 3. (a) Nitrogen adsorption isotherms recorded at 77 K on SBA and SBA-I prepared without and with pre-hydration treatment and (b) their respective normalized pore size

distributions calculated using the BJH method. Note: The SBA used for functionalization here has been synthesized at 100 °C and hence the pore size is 7.8 nm unlike the SBA used for making SBA-V, which had a pore size of 10.3 nm.

SBA-I was then reacted with excess N-methyl-4,4'-bipyridinium iodide to form covalently linked viologen moieties on the pore wall (SBA-V) (Scheme 3). The electrostatic repulsion between the di-positive moieties formed on the pore wall limits the reactivity of the remaining iodopropyl groups towards N-methyl-4,4'-bipyridinium iodide leading to their partial coverage on the pore wall. The amount of iodopropyl functional groups within SBA-I estimated from thermogravimetric analysis was ~1.8 mmol/g (Figure 4a). The amount of viologen estimated from digestive analysis of SBA-V samples was found to be ~0.6 mmol/g, (Figure 4b) which is substantial enough to influence the pore properties. Infra-red spectra of SBA-I shows sp^3 C–H stretches (2940 cm^{-1} and 2850 cm^{-1}) and SBA-V shows a peak at 1631 cm^{-1} characteristic of viologen in addition to sp^2 C–H and sp^3 C–H stretching vibrations (Figure 5).



Scheme 3. Schematic showing the synthetic strategy followed for SBA-V.

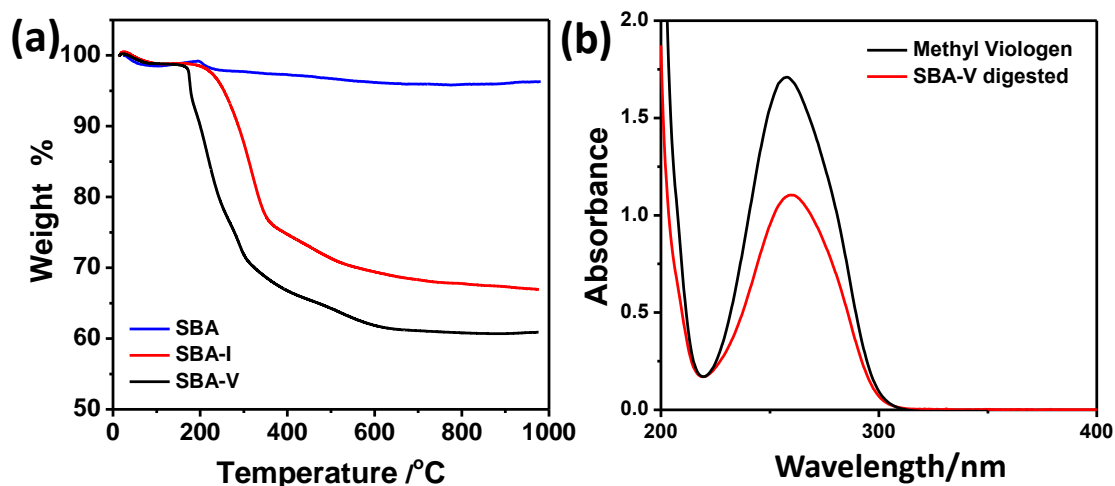


Figure 4. (a) Thermogravimetric analysis curves of SBA, SBA-I and SBA-V. (b) UV-visible spectra of methyl viologen used as reference (1×10^{-4} M) and the digested SBA-V sample. Note: A calibration curve at $(1-10) \times 10^{-5}$ M range for methyl viologen was obtained at the similar conditions as for digestion of SBA-V in order to quantify the amount of viologen in solution.

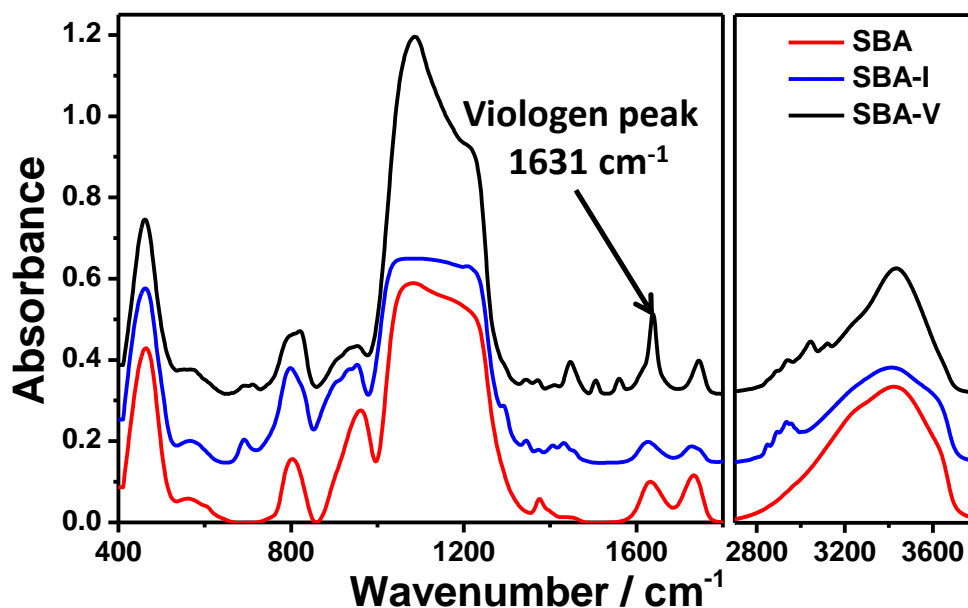


Figure 5. Infra-red spectra of SBA and its functionalized derivatives, SBA-I and SBA-V. Note: The Si—O—Si bending vibration at 460 cm^{-1} was used for intensity calibration.

X-ray diffraction (XRD) patterns of SBA and SBA-V show that the hexagonal structure of SBA is retained all through the functionalization steps (Figure 6a). The nitrogen adsorption isotherms of SBA, SBA-I and SBA-V (Figure 6b) recorded at 77 K are type IV indicating a narrow pore size distribution. The pore size distributions calculated using the Barrett-Joyner-Halenda (BJH) method^[28] reveal a shift of average pore size from 10.3 nm for SBA to 8.3 nm for SBA-I (Figure 6b). Functionalization with viologen further reduces its pore size to 8.0 nm

(Table 1). The small decrease as against its large molecular dimensions (~ 0.9 nm) suggests that the viologen moieties are possibly placed in a tilted orientation inside the pores though more conclusive evidence is necessary to confirm it.

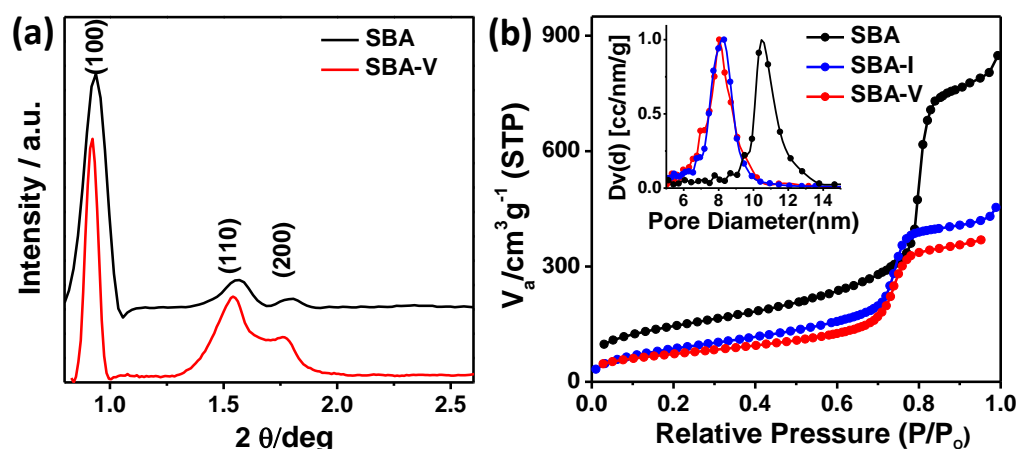


Figure 6. (a) XRD patterns of SBA and SBA-V, showing retention of mesostructural ordering with progress of functionalization. Low angle background scattering was subtracted from both the XRD patterns. (b) Nitrogen adsorption-desorption isotherms and (inset) normalized Barrett-Joyner-Halenda (BJH) pore size distributions of SBA, SBA-I and SBA-V.

Sample	BET SSA* (m ² /g)	D _p (BJH)** (nm)	V _p [#] (cc/g)	BET 'C'### constant
SBA	510	10.3	1.25	148
SBA-I	330	8.3	0.66	37
SBA-V	260	8.0	0.59	89
SBA-V-PC ₆	270	6.7	0.50	54
SBA-V-PC ₁₂	230	6.1	0.43	39
SBA-V _R	300	8.0	0.63	67
SBA-V _R -PC ₆	310	7.1	0.56	57

Table 1. Textural parameters of SBA and its functionalized analogues

*Brunauer-Emmett-Teller Specific Surface Area (Calculated using data points from 0.05 to 0.25 P/P₀)

**Average pore diameter according to the Barrett-Joyner-Halenda pore size distribution calculated from the adsorption branch

[#]Total Pore Volume calculated using data point at 0.98 P/P₀

^{##}BET C values were calculated from the intercept and slope of the BET plot:

$$\text{Slope} = C-1/(V_m C); \text{ Intercept} = 1/V_m C$$

All the above values were computed with the help of Quantachrome Software (ASiQwin).

The UV-visible diffuse reflectance spectrum of the SBA-V shows an intense peak at 265 nm corresponding to the aromatic $\pi - \pi^*$ transition in pyridinium rings (Figure 7a). Addition of pyranine (P) to SBA-V gave a distinct C-T band at 450-600 nm (Figure 7a) and an intense coloration to the resulting SBA-V-P hybrid, providing visual confirmation of the formation of C-T complex between viologen moieties and pyranine (Figure 7b).

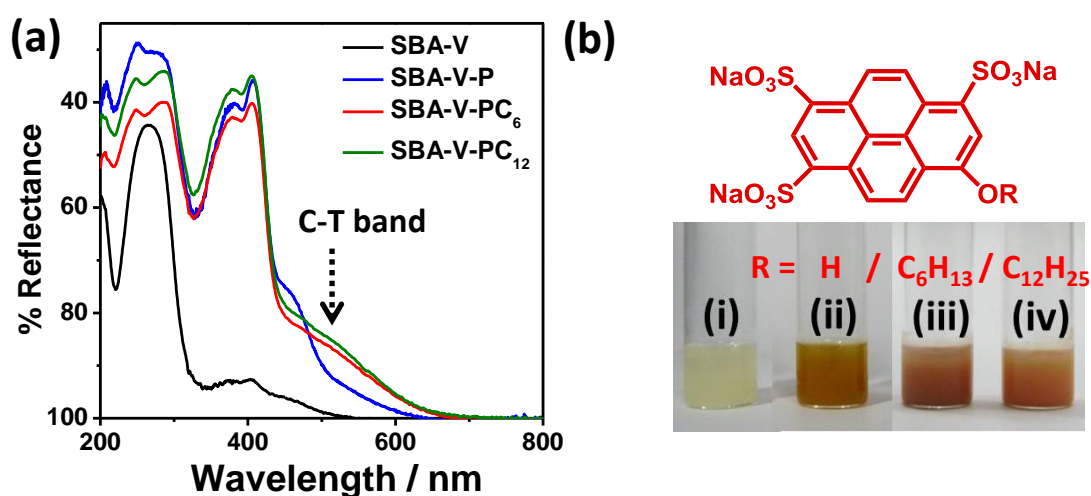


Figure 7. (a) UV-visible diffuse reflectance spectra of SBA-V, SBA-V-P, SBA-V-PC₆ and SBA-V-PC₁₂, showing a C-T band at 450-600 nm. (b) General structure of pyranine (P) and its derivatives. R = H (P), C₆H₁₃ (PC₆) and C₁₂H₂₅ (PC₁₂). Photograph of the dispersions of (i) SBA-V, (ii) SBA-V-P, (iii) SBA-V-PC₆ and (iv) SBA-V-PC₁₂ in water (10 mg/ml).

The strong binding of SBA-V to donors is vital for its effective use in functionalization of the mesopores. The binding titrations of SBA-V with pyranine revealed strong binding behaviour, an enhancement of an order of magnitude (Langmuir binding constant = $1.4 \times 10^5 \text{ M}^{-1}$, Figure 8) for viologen confined to the pores compared to the solution state binding constant obtained by titrating pyranine with methyl viologen^[29] ($1 \times 10^4 \text{ M}^{-1}$). The difference in binding affinities is further evident from the complete uptake of pyranine by the hybrid viologen scaffold, SBA-V, from the pre-associated C-T complexes of pyranine-methyl viologen in solution (Figure 9). The binding curve, plotted as mmol of pyranine uptake versus mmol of pyranine added per gram of SBA-V (Figure 10a), shows an initial strong uptake up to 0.27 mmol/g followed by immediate saturation usually associated with strong receptor mediated binding. A kinetic study of binding revealed that 98% of the binding was complete within two minutes of addition of pyranine to pre-dispersed SBA-V (Figure 10b). The steep uptake by

SBA-V for pyranine can be attributed to both C-T interactions as well as the electrostatic interactions resulting from the di-positively charged viologen moieties.

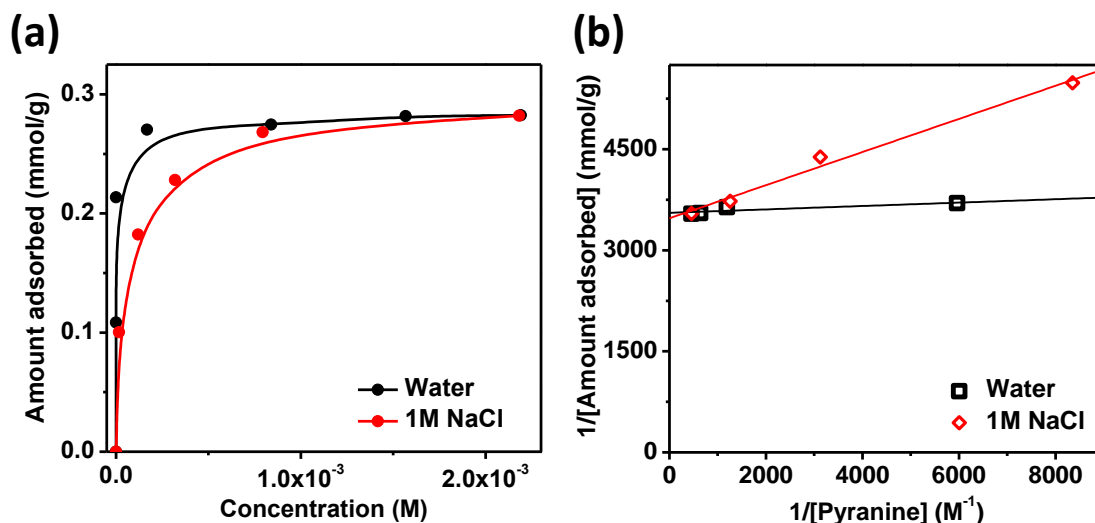


Figure 8. (a) Adsorption isotherms, and (b) linear Langmuir plots for the adsorption of pyranine onto SBA-V in water and in 1M NaCl solution.

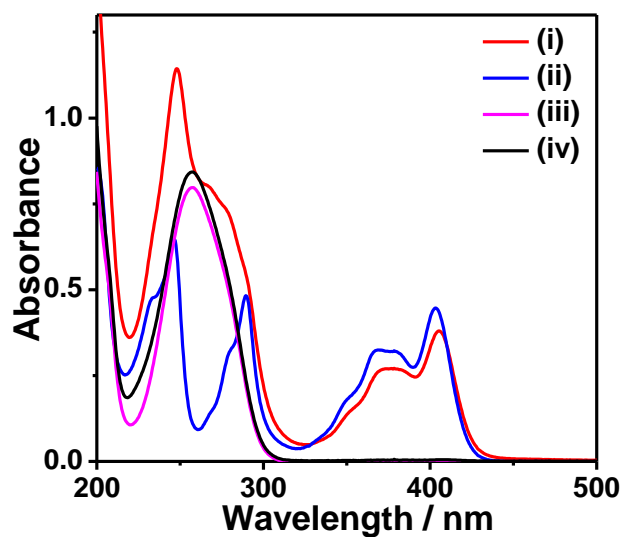


Figure 9. UV-Visible spectra of (i) pre-complexed methyl viologen and pyranine [individual spectra of pyranine and methyl viologen are shown as (ii) and (iii)] used for competitive binding against SBA-V, and (iv) supernatant after competitive binding, showing that only methyl viologen is left behind in the solution and all of the pyranine has complexed with the viologen moieties in the pores of SBA-V.

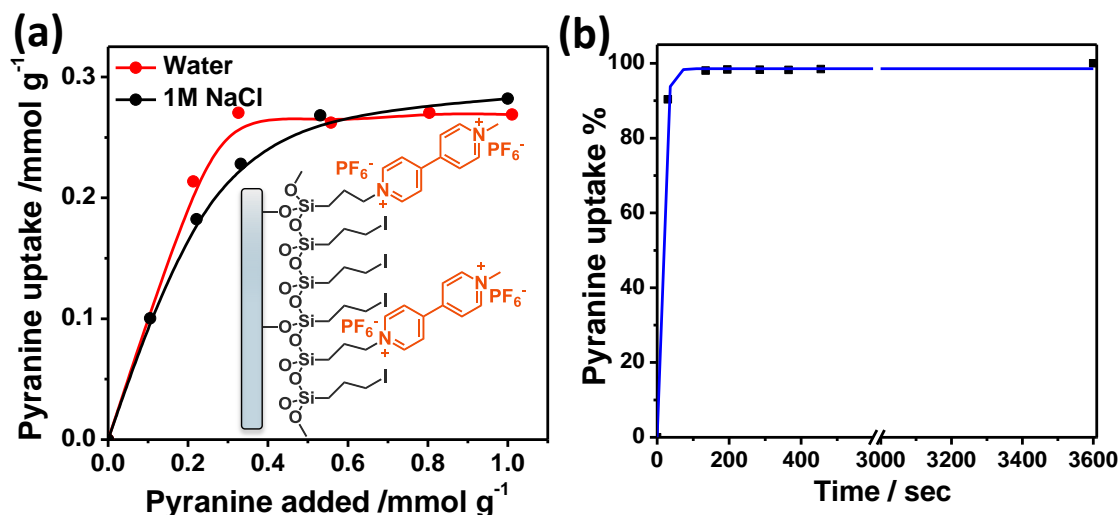
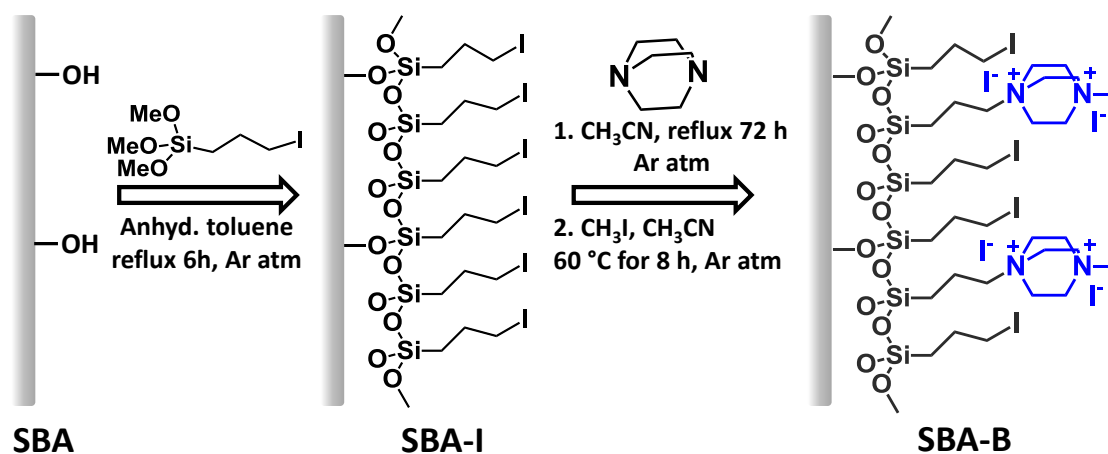


Figure 10. (a) Pyranine binding curves of SBA-V in water and 1M NaCl solution, plotted as mmol of pyranine uptake against mmol of pyranine added per gram of SBA-V. Inset shows a schematic representation of the pore wall of SBA-V. (b) Kinetics of the binding of pyranine to SBA-V was carried out by centrifuging and analyzing the supernatant. In both cases, colorimetric analysis of supernatant for pyranine at its absorption maxima (403 nm) was carried out.

To understand the extent of contribution by electrostatic interactions, an ionic hybrid control, SBA-B, was prepared by reacting SBA-I with 1,4-diazabicyclo[2.2.2]octane (DABCO) (Scheme 4) and then subsequently reacted with excess methyl iodide to form a di-positive ammonium salt on the pore wall. The binding titration of SBA-B with pyranine (Figure 11a) shows uptake till 0.2 mmol/g and a gradual saturation indicating weaker binding. These observations suggest that the electrostatic forces between viologen and pyranine also aid in the uptake for SBA-V. However, when the binding titration was carried out in 1M NaCl solution the SBA-B shows negligible uptake for pyranine (Figure 11a) due to screening of electrostatic forces in high ionic strength media. On the other hand, SBA-V did not show any significant decrease in uptake for pyranine in 1M NaCl solution (Figure 10a). The Langmuir binding constant is weakened only by an order of magnitude in 1M NaCl solution ($1.4 \times 10^4 \text{ M}^{-1}$, Figure 10) indicating a significant contribution from C-T interactions in the uptake of pyranine. It should also be noted that the monolayer capacity (intercept) of SBA-V is the same in both conditions (water as well as 1M NaCl solution) indicating same degree of binding. In contrast to the intense brown color of pyranine bound SBA-V (SBA-V-P), SBA-B bound to pyranine has the same color as that of pyranine indicating absence of charge-transfer interactions with pyranine (Figure 11b).



Scheme 4. Schematic showing the synthetic strategy followed for SBA-B. Note: The dipositive ammonium salt of DABCO could also be attached to the pore wall through both nitrogens and not necessarily as shown.

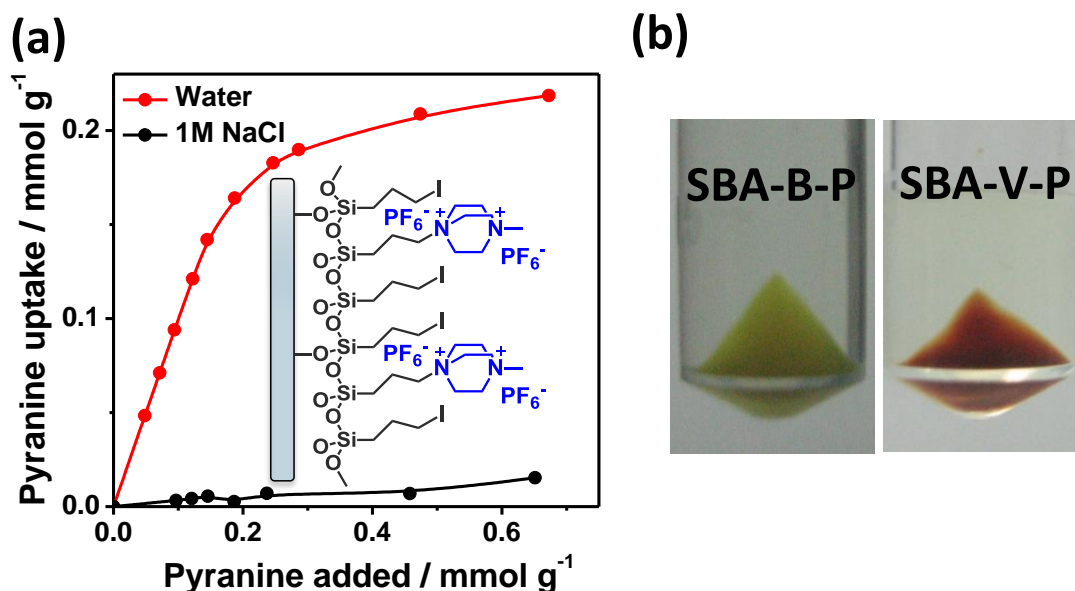


Figure 11. (a) Pyranine binding curves of SBA-B in water and 1M NaCl solution, plotted as mmol of pyranine uptake against mmol of pyranine added per gram of SBA-B. They were obtained by UV-visible spectroscopy analysis of the supernatant for pyranine at its absorption maxima (403 nm). Inset shows a schematic representation of the pore wall of SBA-B. (b) Photographs of SBA-B and SBA-V after pyranine binding.

The strong C-T interactions displayed between the hybrid viologen scaffold and pyranine were then utilized to reversibly modify the pore size and philicity. Pyranine derivatives containing hexyl (PC₆) and dodecyl (PC₁₂) substituents have been chosen as donors for non-covalent functionalization of SBA-V. The initial solution state studies with methyl viologen show charge-transfer complex formation and a stronger charge-transfer absorption band for the viologen-PC₁₂ charge-transfer complex (Figure 12). When SBA-V was soaked in

PC₆ and PC₁₂, the viologens on the pore walls complexed with them to form colored complexes and give C-T bands just as in the case of pyranine (Figure 7a-b). The nitrogen adsorption isotherms of SBA-V containing non-covalently functionalized pyranine derivatives retain type IV behavior (Figure 13a). However, the spinodal condensation transition shifted to lower P/Po implying reduction of the pore size. Noticeably, the pore size reduced from 8.0 nm for SBA-V to 6.7 nm for SBA-V-PC₆ and to 6.0 nm for SBA-V-PC₁₂ (Table 1, Figure 13b,c), a reduction in conformance with the alkyl chain length. The pore size distributions SBA-V-PC₆ and SBA-V-PC₁₂ have similar full width at half maximum (FWHM) as that of SBA-V, indicating uniform supramolecular functionalization (Figure 13b). The pyranine derivatives can be removed by breaking the C-T interactions through reduction of viologen followed by washing with salt solution and oxidation using molecular oxygen to give SBA-V_R. Remarkably, the removal of PC₆ derivative brought back the pore size to 8.0 nm and further addition of PC₆ again reduced the pore size to about 7 nm. The incomplete reversal of pore size on addition of PC₆ is probably due the degradation of some viologen moieties during oxidation through the superoxide mechanism^[30]. This degradation was overcome by the use of a milder oxidizing agent, K₃[Fe(CN)₆]. The recyclability of viologen was monitored through the pyranine binding capacity of SBA-V (Figure 14). The use of degassed solution of K₃[Fe(CN)₆] allowed recycling of viologens with less than 10% degradation over three cycles which enabled reversible switching of pore size.

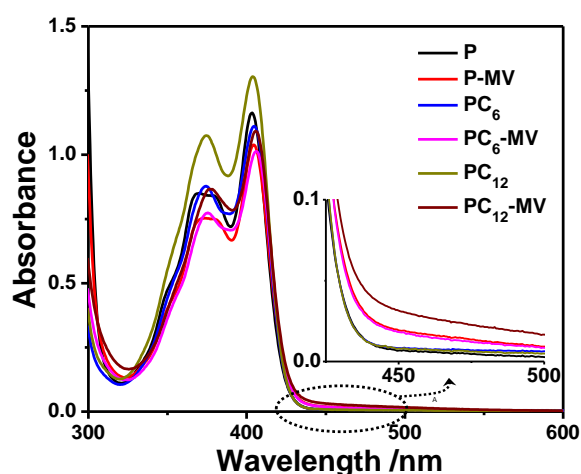


Figure 12. UV-Vis spectra of pyranine (P), hexyl appended pyranine (PC₆) and dodecyl appended pyranine (PC₁₂) and their charge-transfer complexes (1:1) with methyl viologen (MV) in solution. The inset showing C-T bands of P-MV, PC₆-MV and PC₁₂-MV from 440 – 500 nm. It can be seen that the C-T bands are stronger for PC₁₂-MV than for P-MV and PC₆-MV.

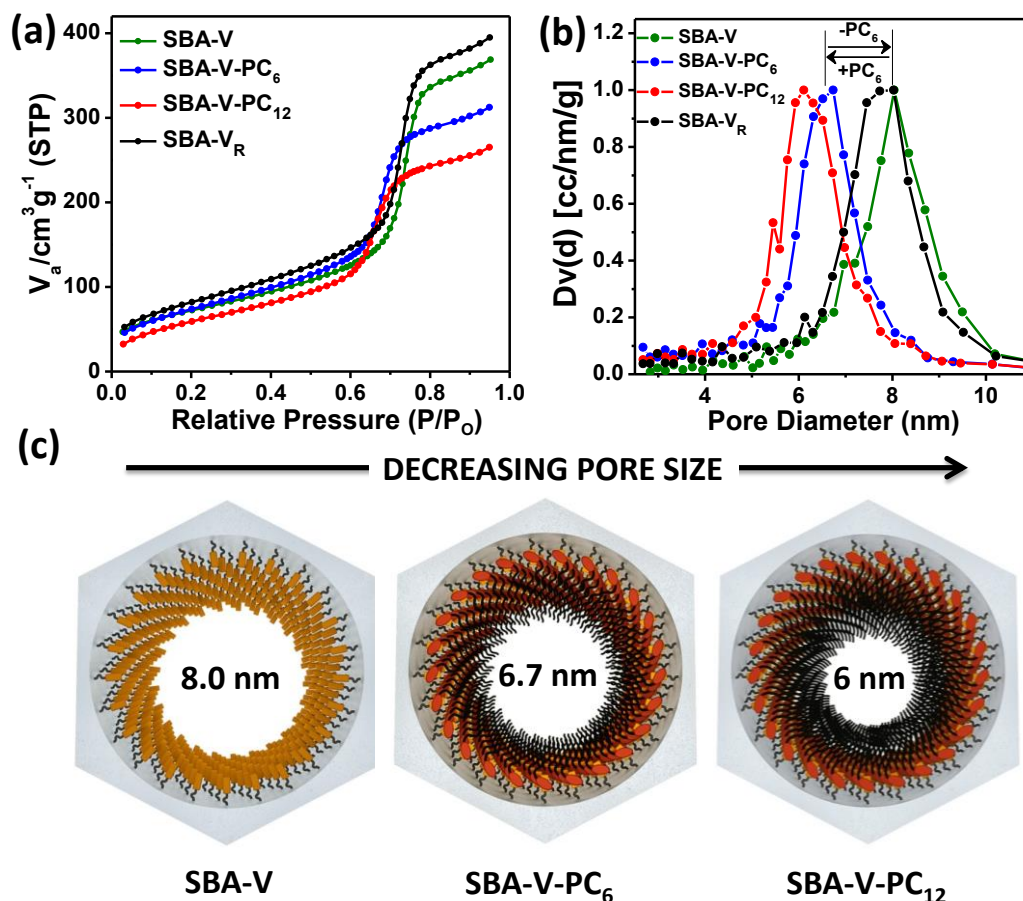


Figure 13. (a) Nitrogen adsorption isotherms at 77K and (b) normalized Barrett-Joyner-Halenda (BJH) pore size distributions of SBA-V, SBA-V-PC₆ and SBA-V-PC₁₂ showing the gradual decrease in pore size on addition of PC₆ and PC₁₂. The removal of PC₆ from SBA-V-PC₆ gives SBA-V_R which shows a reversal of pore size back to SBA-V. [SBA-V (8.0 nm) to SBA-V-PC₆ (6.7 nm) to SBA-V_R (8.0 nm)] (c) Schematic showing decrease in pore size on functionalization with PC₆ and PC₁₂, (alkyl chains shown in black) [Schematic not drawn to scale].

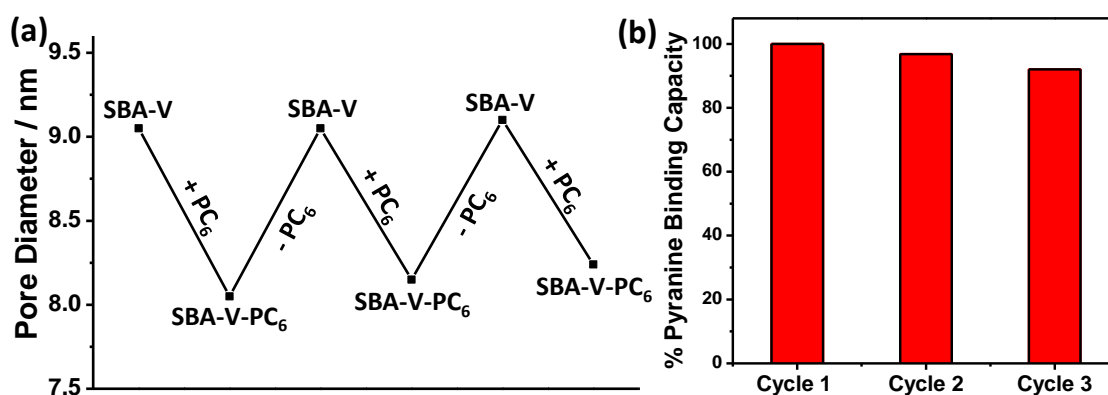


Figure 14. (a) The variation of pore size (monitored through nitrogen adsorption isotherms) on addition and removal of pyranine derivative, PC₆, to SBA-V (with initial pore diameter of 9.0

nm) showing good reversibility. (b) The variation in pyranine binding capacity of SBA-V exposed to three consecutive reduction-oxidation cycles shows that SBA-V retains > 90% of its native binding capacity.

The non-covalent attachment of the pyranine derivatives to SBA-V not only modifies the pore size but also the philicity, due to the presence of hydrophobic alkyl chains. Water sorption isotherms were recorded to follow the change in philicity of the pore^[31] (Figure 15). Functionalization of SBA with viologen shifts the pore filling transition of SBA from $P/P_0 \sim 0.8$ to $P/P_0 \sim 0.7$ for SBA-V. Complexation of these viologen moieties with PC_6 shifts the pore condensation to higher P/P_0 (~ 0.85). It should be noted that there is a concomitant decrease in pore size as well, which would shift the pore filling transition to lower P/P_0 . Nonetheless, there is a shift of pore condensation from 0.7 to 0.85 indicating that the increase in hydrophobicity is more than what is apparent from the shift of transition. This change is more prominent for SBA-V- PC_{12} , which shows very poor uptake of water. The values of BET constant 'C', derived from the nitrogen adsorption isotherms for SBA-V containing pyranine derivatives are small, indicating low heats of adsorption which agree well with the water sorption behaviour^[32] (Table 1).

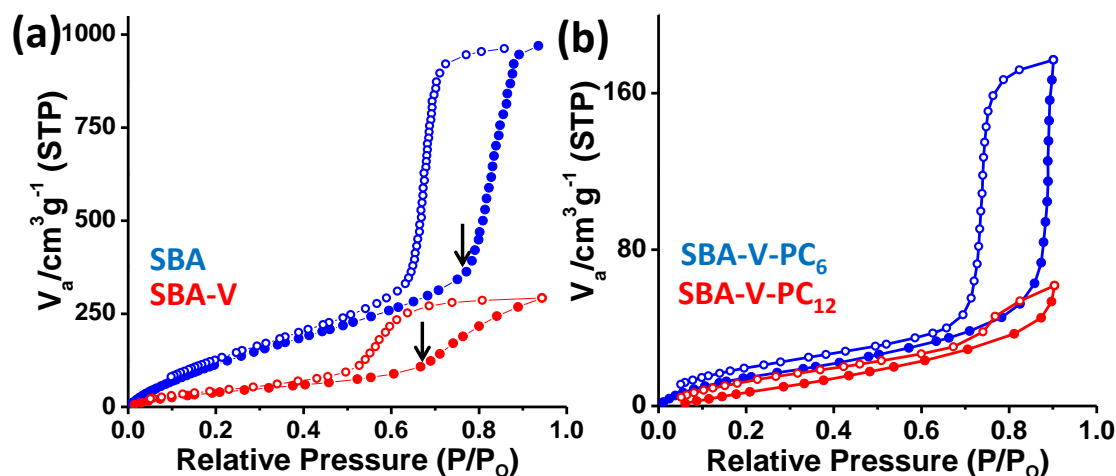


Figure 15. Water sorption isotherms of (a) SBA and SBA-V and (b) SBA-V- PC_6 and SBA-V- PC_{12} recorded at 298 K.

This variation in the philicity between SBA-V, SBA-V- PC_6 and SBA-V- PC_{12} has further been demonstrated by their selective uptake towards hydrophilic FITC labeled dextran and hydrophobic protein myoglobin, respectively. The adsorption of protein was carried out at its isoelectric pH (7.2) so as to avoid any influence of pore surface charge. The molecular dimensions of myoglobin^[24] and 4 kDa dextran^[23] are $2.9 \times 3.6 \times 6.4$ nm and 3 nm respectively. The SBA-V- PC_{12} and SBA-V- PC_6 exhibited stronger uptake for myoglobin than dextran (hydrophilic) indicating hydrophobicity driven uptake. However, SBA-V shows a higher uptake

for dextran than myoglobin implying hydrophilicity driven uptake (Figure 16a). The same trend was observed in the mixed adsorption study as well, where both dextran and myoglobin were added together. (Figure 16b).

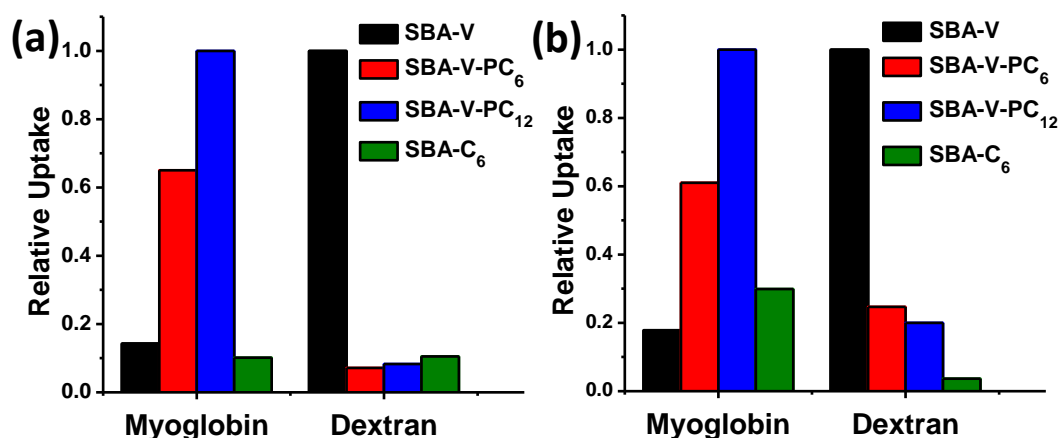


Figure 16. Relative uptakes of myoglobin and FITC-dextran (4 kDa) by SBA-V, SBA-V-PC₆ and SBA-V-PC₁₂ in (a) individual and (b) in mixed adsorption experiments, showing philicity-driven uptake.

In order to compare the non-covalently functionalised SBA with a covalent analogue, hexyltrichlorosilane was used to covalently modify SBA with hexyl chains (SBA-C₆). Covalently modified SBA-C₆ shows type IV nitrogen adsorption isotherm and a narrow pore size distribution indicating uniform functionalization of hexyl pendants (Figure 17a). thermogravimetric analysis shows significant amount (20%) of organic functionalization (Figure 17b).

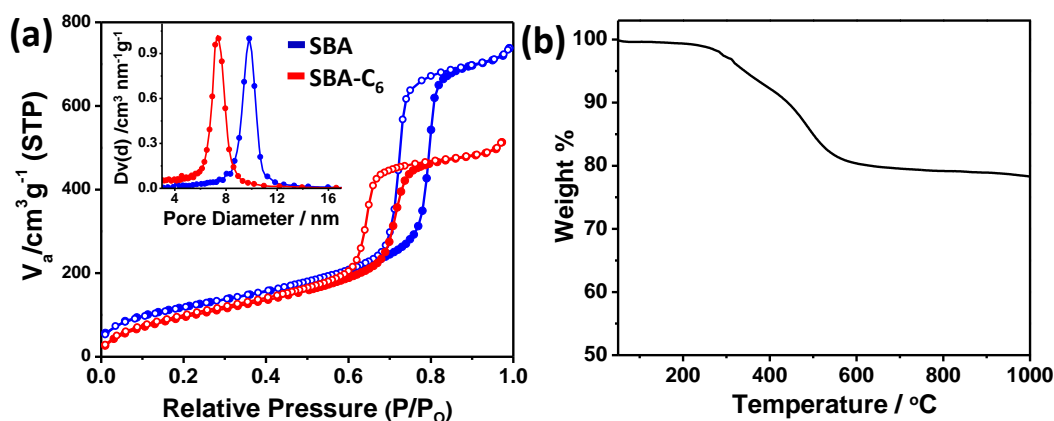


Figure 17. (a) Nitrogen adsorption-desorption isotherms and (inset) normalized Barrett-Joyner-Halenda (BJH) pore size distributions of SBA and SBA-C₆. (b) Thermogravimetric analysis of SBA-C₆.

Macromolecule adsorption studies showed that the uptake of myoglobin in SBA-V-PC₆ is two-three times greater than SBA-C₆, probably due to its better dispersibility in water owing to the polar C-T anchors on the pore wall (Figure 16). SBA-C₆ on the other hand, is very poorly dispersible in water resulting in its poor uptake.

2.6. Conclusions

In conclusion, we have shown a novel non-covalent strategy for the modular and reversible functionalization of mesopores by making use of charge-transfer interactions. The adaptive nature of the pores in mesoporous silica was clearly demonstrated through nitrogen and water sorption studies as well as selective uptake of macromolecules. The increased strength and fast dynamics of pyranine binding to viologen on the pore wall make them ideal modules for non-covalently modifying the pore size and philicity. Incorporation of multiple functionalities into mesopores through the conventional covalent silane pathway has no direct control because different silanes have varying hydrolysis rate in solution. The modularity of the approach enables modification of pores with custom designed compositions, components and functions. We envisage that this non-covalent methodology would enable uniform distribution of functional groups by virtue of its reversible nature. Further, it is also conceivable that these non-covalent modules within the confines of the pores can be designed to undergo non-equilibrium and dynamic redistribution in response to external stimuli akin to biological systems^[33].

2.7. References

- [1] a) T. Maschmeyer, F. Rey, G. Sankar, J. M. Thomas, *Nature* **1995**, *378*, 159-162; b) A. Corma, *Chem. Rev.* **1997**, *97*, 2373-2420; c) M. Choi, H. S. Cho, R. Srivastava, C. Venkatesan, D.-H. Choi, R. Ryoo, *Nat. Mater.* **2006**, *5*, 718-723.
- [2] a) Y. Kuwahara, D.-Y. Kang, J. R. Copeland, N. A. Brunelli, S. A. Didas, P. Bollini, C. Sievers, T. Kamegawa, H. Yamashita, C. W. Jones, *J. Am. Chem. Soc.* **2012**, *134*, 10757-10760; b) A. Walcarius, L. Mercier, *J. Mater. Chem.* **2010**, *20*, 4478-4511.
- [3] a) V. Mamaeva, J. M. Rosenholm, L. T. Bate-Eya, L. Bergman, E. Peuhu, A. Duchanoy, L. E. Fortelius, S. Landor, D. M. Toivola, M. Linden, C. Sahlgren, *Mol. Ther.* **2011**, *19*, 1538-1546; b) C. Coll, A. Bernardos, R. Martínez-Máñez, F. Sancenón, *Acc. Chem. Res.* **2012**, doi: 10.1021/ar3001469; c) J. L. Vivero-Escoto, R. C. Huxford-Phillips, W. Lin, *Chem. Soc. Rev.* **2012**, *41*, 2673-2685.

- [4] a) D. R. Radu, C.-Y. Lai, J. W. Wiench, M. Pruski, V. S. Y. Lin, *J. Am. Chem. Soc.* **2004**, *126*, 1640-1641; b) V. S. Y. Lin, C.-Y. Lai, J. Huang, S.-A. Song, S. Xu, *J. Am. Chem. Soc.* **2001**, *123*, 11510-11511.
- [5] a) A. Yamaguchi, N. Teramae, *Anal. Sci.* **2008**, *24*, 25-30; b) X. Ma, X. Wang, C. Song, *J. Am. Chem. Soc.* **2009**, *131*, 5777-5783.
- [6] a) S. Inagaki, S. Guan, T. Ohsuna, O. Terasaki, *Nature* **2002**, *416*, 304-307; b) X. Feng, *Science* **1997**, *276*, 923-926; c) F. Hoffmann, M. Cornelius, J. Morell, M. Fröba, *Angew. Chem. Int. Ed.* **2006**, *45*, 3216-3251; d) N. Linares, E. Serrano, M. Rico, A. Mariana Balu, E. Losada, R. Luque, J. Garcia-Martinez, *Chem. Commun.* **2011**, *47*, 9024-9035.
- [7] a) Q. Huo, D. I. Margolese, U. Ciesla, P. Feng, T. E. Gier, P. Sieger, R. Leon, P. M. Petroff, F. Schuth, G. D. Stucky, *Nature* **1994**, *368*, 317-321; b) C. Jung, P. Schwaderer, M. Dethlefsen, R. Kohn, J. Michaelis, C. Brauchle, *Nat Nano* **2011**, *6*, 87-92; c) Q. Huo, D. I. Margolese, U. Ciesla, D. G. Demuth, P. Feng, T. E. Gier, P. Sieger, A. Firouzi, B. F. Chmelka, *Chem. Mater.* **1994**, *6*, 1176-1191.
- [8] M. Widenmeyer, R. Anwender, *Chem. Mater.* **2002**, *14*, 1827-1831.
- [9] D. Zhao, J. Feng, Q. Huo, N. Melosh, G. H. Fredrickson, B. F. Chmelka, G. D. Stucky, *Science* **1998**, *279*, 548-552.
- [10] P. F. Fulvio, S. Pikus, M. Jaroniec, *J. Mater. Chem.* **2005**, *15*, 5049-5053.
- [11] S.-Y. Chen, Y.-T. Chen, J.-J. Lee, S. Cheng, *J. Mater. Chem.* **2011**, *21*, 5693-5703.
- [12] S. Jambhrunkar, M. Yu, J. Yang, J. Zhang, A. Shrotri, L. Endo-Munoz, J. Moreau, G. Lu, C. Yu, *J. Am. Chem. Soc.* **2013**, *135*, 8444-8447.
- [13] D. Bruhwiler, *Nanoscale* **2010**, *2*, 887-892.
- [14] P. Van Der Voort, D. Esquivel, E. De Canck, F. Goethals, I. Van Driessche, F. J. Romero-Salguero, *Chem. Soc. Rev.* **2013**, *42*, 3913-3955.
- [15] N. Liu, Z. Chen, D. R. Dunphy, Y.-B. Jiang, R. A. Assink, C. J. Brinker, *Angew. Chem. Int. Ed.* **2003**, *42*, 1731-1734.

- [16] Liu, D. R. Dunphy, P. Atanassov, S. D. Bunge, Z. Chen, G. P. López, T. J. Boyle, C. J. Brinker, *Nano Lett.* **2004**, *4*, 551-554.
- [17] M. Alvaro, B. Ferrer, H. Garcia, F. Rey, *Chem. Commun.* **2002**, 2012-2013.
- [18] a) H. Y. Au-Yeung, G. D. Pantoş, J. K. M. Sanders, *Proc. Natl. Acad. Sci. U. S. A.* **2009**, *106*, 10466-10470; b) F. Tian, D. Jiao, F. Biedermann, O. A. Scherman, *Nat. Commun.* **2012**, *3*, doi: 10.1038/ncomms2198; c) U. Rauwald, O. A. Scherman, *Angew. Chem. Int. Ed.* **2008**, *47*, 3950-3953; d) S. Shimomura, R. Matsuda, T. Tsujino, T. Kawamura, S. Kitagawa, *J. Am. Chem. Soc.* **2006**, *128*, 16416-16417; e) A. Okabe, T. Fukushima, K. Ariga, T. Aida, *Angew. Chem.* **2002**, *114*, 3564-3567; f) K. V. Rao, K. Jayaramulu, T. K. Maji, S. J. George, *Angew. Chem. Int. Ed.* **2010**, *49*, 4218-4222.
- [19] A. Sayari, B.-H. Han, Y. Yang, *J. Am. Chem. Soc.* **2004**, *126*, 14348-14349.
- [20] M. J. Wirth, H. O. Fatunmbi, *Anal. Chem.* **1993**, *65*, 822-826.
- [21] J. Nakazawa, B. J. Smith, T. D. P. Stack, *J. Am. Chem. Soc.* **2012**, *134*, 2750-2759.
- [22] R. Sasaki, S. Murata, *Langmuir* **2008**, *24*, 2387-2394.
- [23] M. S. Toprak, B. J. McKenna, J. H. Waite, G. D. Stucky, *Chem. Mater.* **2007**, *19*.
- [24] L.-C. Sang, A. Vinu, M.-O. Coppens, *Langmuir* **2011**, *27*, 13828-13837.
- [25] T. G. Carter, W. Yantasee, T. Sangvanich, G. E. Fryxell, D. W. Johnson, R. S. Addleman, *Chem. Commun.* **2008**, 5583-5585.
- [26] K. S. W. Sing, D. H. Everett, R. A. W. Haul, L. Moscou, R. A. Pierotti, J. Rouquerol, T. Siemieniewska, *Pure Appl. Chem.* **1985**, *57*, 603-619.
- [27] J. S. Beck, J. C. Vartuli, W. J. Roth, M. E. Leonowicz, C. T. Kresge, K. D. Schmitt, C. T. W. Chu, D. H. Olson, E. W. Sheppard, *J. Am. Chem. Soc.* **1992**, *114*, 10834-10843.
- [28] E. P. Barrett, L. G. Joyner, P. P. Halenda, *J. Am. Chem. Soc.* **1951**, *73*, 373-380.
- [29] E. B. de Borba, C. L. C. Amaral, M. J. Politi, R. Villalobos, M. S. Baptista, *Langmuir* **2000**, *16*, 5900-5907.
- [30] M. Tagliacruzchi, V. A. Amin, S. T. Schneebeli, J. F. Stoddart, E. A. Weiss, *Adv. Mater.* **2012**, *24*, 3617-3621.

- [31] T. Kimura, M. Suzuki, M. Maeda, S. Tomura, *Microporous Mesoporous Mater.* **2006**, 95, 213-219.
- [32] J. A. Osaheni, S. T. Buddle (General Electric Company, USA .), US6193412B1, **2001**
- [33] S. Mann, *Nat. Mater.* **2009**, 8, 781-792.

Chapter-3

Selective Sequestration of Chromophores using Charge-transfer Interactions

Summary

The viologen immobilized on the walls of mesoporous silica showed very high selectivity of binding to donors. The adsorption selectivity factor for donors of similar charge but different charge-transfer strength was in the range of 42-48. A charge-transfer based breakthrough column could be fabricated using viologen modified silica to separate donors based on their molecular charge and charge-transfer strength. Clear breakthrough curves were obtained for a three component mixture of donors of similar charge but differing only in their charge-transfer strength. Non polar environment around the viologens was found to play an important role in determining the binding selectivity.

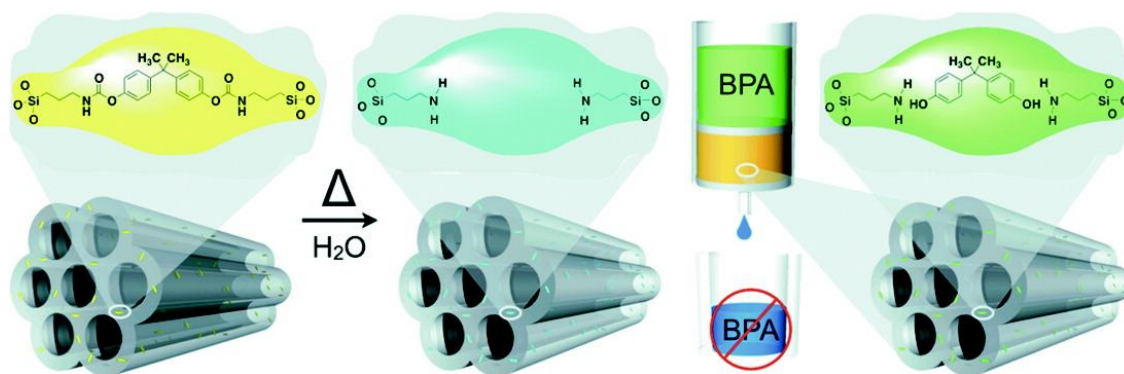
Manuscript based on this work is under preparation.

3.1. Introduction

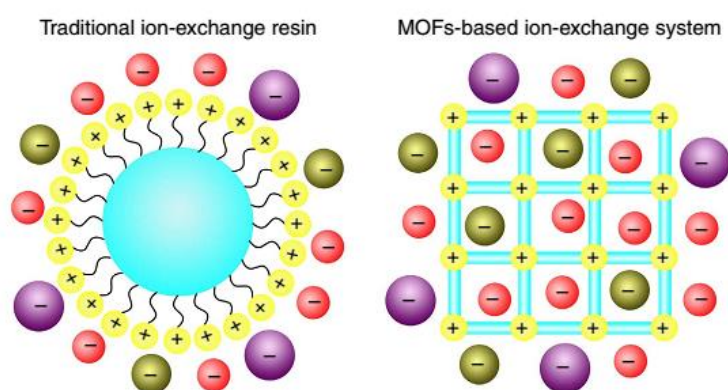
Host materials exhibiting highly selective binding for specific molecules have attracted significant research interest by virtue of their applications in separation, recognition and sensing of these molecules. Materials such as porous carbon,^[1] hydrogels,^[2] metal organic frameworks (MOF),^[3] mesoporous silica^[4] and polymers^[5] have been used for adsorption based separation. The selectivity of adsorption in these materials is mediated by charge,^[6] size,^[1] philicity and other spatially specific interactions like in molecular imprinted polymers.^[5] Charge based selectivity stems from the fact that the adsorbent has a charged surface and hence the adsorption of oppositely charged species is encouraged. Size based selectivity is seen in materials with very uniform pore sizes and hence, capable of restricting entry into the porous space for adsorption based on size or molecular dimensions. Selectivity based on philicity is the result of any kind of favourable interactions between the adsorbent and adsorbate. In this context, it has been used to indicate selectivity due to hydrophilic or hydrophobic character. Molecular imprinting^[7] on the other hand, is a specific recognition technique wherein the interacting groups are spatially organised with the help of imprint molecules during polymerisation of the host material. This technique can distinguish between enantiomers^[8] as well due to its spatial component. Though molecular imprinting was pioneered in silica,^[9] it has been explored extensively in polymers due to the problems of rigidity and mass transport in microporous silica.^[10] The issue of mass transport was addressed by using the walls of mesoporous silica^[11] (MCM-41) for imprinting.

Recently, Ozin et al.^[4] used SBA-15 for molecular imprinting which has larger pore size and thicker pore walls to better maintain the shape of the template cavity (Scheme 1). To attain greater selectivity, a combination of factors can be employed. For example, Feng et al.^[3a] synthesised a charged MOF capable of ion exchange exhibiting selective dye adsorption based on size and charge (Scheme 2). Ariga et al.^[12] reported a highly selective sensor based on cooperative nanopore filling due to pore size matching with the adsorbate and enhanced interactions between the adsorbate molecules themselves. Muthusamy et al.^[1] used switching of pore size in porous carbon to manipulate the selectivity of dye adsorption.

In a different approach from the above strategies, we demonstrate the selective uptake of donors by viologen modified mesoporous silica induced by charge-transfer interactions.



Scheme 1. Molecularly imprinted mesoporous organosilica prepared by Ozin et al^[4]. showing high selectivity of binding to bisphenol A (BPA). (Reproduced with permission from reference 4)



Scheme 2. Illustration showing the size based exclusion exhibited by an ion-exchange system based on MOF with respect to a traditional ion-exchange resin. (Reproduced with permission from reference 3a)

3.2. Scope of the present investigation

The present study looks at the selectivity of binding exhibited by the viologen modified SBA (SBA-V) described in chapter 2. We examined the selectivity of SBA-V for two different donors, coronene tetracarboxylate (CS) and perylene tetracarboxylate (PS), which bear similar molecular charge but differ in the strength of the charge-transfer interaction with viologen. Very high selectivity factors (CS to PS) in the range of 42-48 were obtained in contrast to the solution state selectivity factor which was 1.2. Breakthrough experiments were conducted on a bed of SBA-V to check for the separation in a flow-based system. They showed very clean breakthrough curves showing good separation capability. We have also demonstrated clear breakthrough curves for a three-component equimolar mixture of CS, PS, and pyrene tetrasulfonate (P4), all of which have the same molecular charge but different charge-transfer (C-T) properties. To further understand the factors governing the high selectivity, the functional

groups around viologen moieties were modified and their selectivity factors for CS and PS were studied.

3.3. Experimental section

Synthesis of viologen functionalized SBA

It involves two steps: (i) iodopropyl functionalization and (ii) viologen functionalization.

(i) Iodopropyl functionalization (SBA-I). Monodispersed SBA-15 (referred to as SBA) rods were synthesized using a reported procedure^[13]. 1 g of calcined mesoporous silica rods were degassed and then pre-hydrated in a controlled fashion till the relative humidity of 50% and added into dry toluene along with 2.5 mL of IPTMS (12.7 mmol) and stirred overnight. The temperature was increased to 110 °C and held for 6 h to complete the reaction. The obtained SBA-I was washed with toluene (3×40 mL) and ethanol (1×40 mL) before finally subjecting to soxhlet extraction in ethanol to completely wash away uncondensed silane from the pores.

(ii) Viologen functionalization (SBA-V). 1 g of SBA-I degassed at 80 °C for 6 h was added to 120 mL of dry acetonitrile (CH₃CN) along with 2.5 g (8.3 mmol) of N-methyl-4,4'-bipyridinium iodide and refluxed for 3-4 days. The SBA-V obtained was washed with acetonitrile (2×40 mL), water (2×40 mL) and finally ethanol. It was subjected to ion exchange by stirring with 50 mL of 0.5 M ammonium hexafluorophosphate solution for 5 h at room temperature and then raising the temperature to 60 °C for 0.5 h. It was then washed with water (3×40 mL) and ethanol (1×40 mL) before drying in the oven at 80 °C.

Synthesis of azide functionalized SBA-V (SBA-V_{AZ})

1 g of SBA-V (before subjecting to ion exchange) degassed at 80 °C for 6 h was reacted with 0.4 g sodium azide in presence of tetrabutylammonium bromide (0.23 g) in 20 mL of dimethyl sulphoxide (DMSO) for 2 days at 95 °C. The solution was then centrifuged and washed with DMSO three times and finally with ethanol. It was subjected to ion exchange by stirring with 50 mL of 0.5 M ammonium hexafluorophosphate solution for 5 h at room temperature and then raising the temperature to 60 °C for 0.5 h. It was then washed with water (3×40 mL), and ethanol (1×40 mL) and dried at 80 °C. (Refer to scheme 3 for structural details of SBA-V_{AZ})

Amine functionalized SBA-V (SBA-V_{AM})

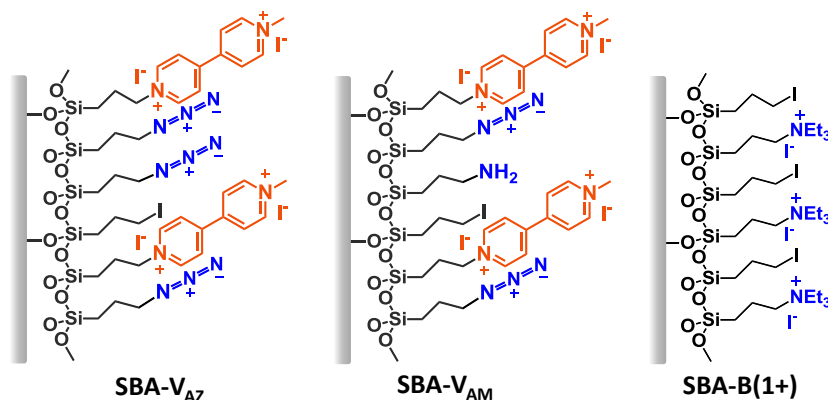
0.35 g azide functionalized SBA-V (before ion exchange) was stirred at room temperature with 0.4 g (1.5 mmol) triphenylphosphine in dry THF for 2 days. Excess water was then added to it and stirring was continued for 15 more minutes. The solution was then centrifuged and washed

with dimethylformamide and chloroform. It was then subjected to ion exchange with ammonium hexafluorophosphate. (Refer to scheme 3 for structural details of SBA-V_{AM})

Synthesis of electrostatic blanks

(i) **SBA-B(1+)**. 0.3 g of SBA-I degassed at 80 °C for 6 h was added to 40 mL of acetonitrile along with 3.0 mL of triethylamine (2.2 mmol) and 1.0 g of tetrabutylammonium bromide and heated at 60 °C for 2 days under inert atmosphere. The SBA-B(1+) obtained was washed with CH₃CN (2×40 mL), water (2×40 mL) and finally ethanol. It was subjected to ion exchange by stirring with 50 mL of 0.5 M ammonium hexafluorophosphate solution for 5 h at room temperature and then raising the temperature to 60 °C for 0.5 h. It was then washed with water (3×40 mL), and ethanol (1×40 mL) and dried at 80 °C. [Refer to scheme 3 for structural details of SBA-B(1+)]

(ii) **SBA-N**. 0.5 g of SBA was degassed at 80 °C for 6 h and pre-hydrated till 50 % relative humidity was reached. It was then added into 30 mL of dry and degassed toluene along with 1.5 mL of aminopropyltriethoxysilane and refluxed for 24 h under argon atmosphere. The product was then washed with toluene (3×40 mL) and ethanol (3×40 mL), and finally dried at 60 °C.



Scheme 3. Illustration showing the chemical functionalities on the pore walls of SBA-V_{AZ}, SBA-V_{AM} and SBA-B(1+).

Donor binding stoichiometry studies

10 mg of SBA-V was weighed into separate vials and appropriate amounts of donors (CS/Pyranine/Eosin) were added. The dispersions were stirred for 6 h and centrifuged. The supernatant was analyzed using UV-Vis spectroscopy to determine the amount of donors left behind in the solution. For each donor a separate calibration curve was obtained in order to back calculate the amount of donor bound by SBA-V.

CS: [2 to 10] × 10⁻⁵ M (λ_{\max} = 312 nm, ϵ = 11180 M⁻¹mm⁻¹)

Pyranine: $[1 \text{ to } 5] \times 10^{-4} \text{ M}$ ($\lambda_{\text{max}} = 403 \text{ nm}$, $\epsilon = 2300 \text{ M}^{-1}\text{mm}^{-1}$)

Eosin: $[2 \text{ to } 10] \times 10^{-5} \text{ M}$ ($\lambda_{\text{max}} = 516 \text{ nm}$, $\epsilon = 8360 \text{ M}^{-1}\text{mm}^{-1}$)

Selectivity studies

10 mg of the sample to be studied was weighed into separate vials. Appropriate amounts of equimolar mixture of CS and PS were added, stirred for 6 h and centrifuged. The supernatant was analysed using UV-Vis spectroscopy to determine the amount of CS and PS left behind in the solution. A calibration curve for CS was obtained in the range $[2 \text{ to } 10] \times 10^{-5} \text{ M}$ ($\lambda_{\text{max}} = 312 \text{ nm}$, $\epsilon = 11180 \text{ M}^{-1}\text{mm}^{-1}$) and for PS in the range $[1 \text{ to } 5] \times 10^{-4} \text{ M}$ ($\lambda_{\text{max}} = 467 \text{ nm}$, $\epsilon = 3660 \text{ M}^{-1}\text{mm}^{-1}$). From this, the amount of donor taken up by the sample was back calculated. For the sake of reducing error, a stock solution containing equal amounts of donors was used and a blank vial (not containing sample) accompanied every vial of sample used for this study.

Breakthrough Column^[14]

(i) CS/PS Breakthrough. A 100 mg mixture of SBA-V and SBA (1:3 by weight) [SBA was used as a filler material as it doesn't show any selectivity] was packed into a column and an equimolar mixture of CS and PS ($1 \times 10^{-3} \text{ M}$) was passed through the column at the rate of 0.1 mL per minute. 0.1 ml fractions were collected and analyzed using UV-visible spectroscopy. The feed solution was passed till the outlet composition reached equimolar ratio and then a water purge was applied to elute the contents adsorbed in the column.

(ii) CS/PS/P4 Breakthrough. A 160 mg mixture of SBA-V and SBA (1:3 by weight) [SBA was used as a filler material as it was not showing any selectivity] was packed into a column and an equimolar mixture ($5 \times 10^{-4} \text{ M}$) of CS, PS and pyrene tetrasulfonate (P4) was passed through the column at rate of 0.1 mL per minute. The rest of the protocol is same as the CS/PS breakthrough.

3.4. Characterization

Please refer to the appendix for the instrumental details of UV-visible spectroscopy, fluorescence spectroscopy, infra-red spectroscopy, nitrogen sorption analysis and zeta potential measurements.

3.5. Results and discussion

Nano-confinement leads to drastic changes in properties of molecules. For example, pK_a of the functional groups can change by 3-4 units upon confinement.^[15] The viologen immobilised on the pore walls of SBA-15 was found to bind strongly to pyranine (donor)

exhibiting an increase in the binding constant upto two orders in magnitude in comparison to its solution state analogue (Chapter 2). In this chapter, we study the effects of local environment of viologen within the pores of SBA-V on its binding selectivity.

Mesoporous silica, SBA-15, was synthesised and modified with viologen moieties using the iodopropylsilane route to form SBA-V (Chapter 2). As described in chapter 2, an electrostatic blank was also synthesised by functionalising SBA with dipositive ammonium moieties of DABCO to form SBA-B. The binding of various donors to SBA-V was studied in order to establish the binding stoichiometry. The donors chosen are given below (Figure 1a): Coronene tetracarboxylate (CS) – Four negative charges; Perylene tetracarboxylate (PS) – Four negative charges; Pyranine (PYR) – Three negative charges; Eosin (ES) – Two negative charges

The binding of these donors (Figure 1b) to SBA-V gave strongly coloured dispersions to the otherwise colourless SBA-V (Figure 1c). The UV-visible reflectance spectra of the SBA-V bound to various donors (Figure 1e) showing the features of individual donors (Figure 1d) along with charge transfer bands at 400-600 nm (SBA-V-CS), 450-650 nm (SBA-V-PYR), 500-650 nm (SBA-V-PS) and 600-700 nm (SBA-V-ES).

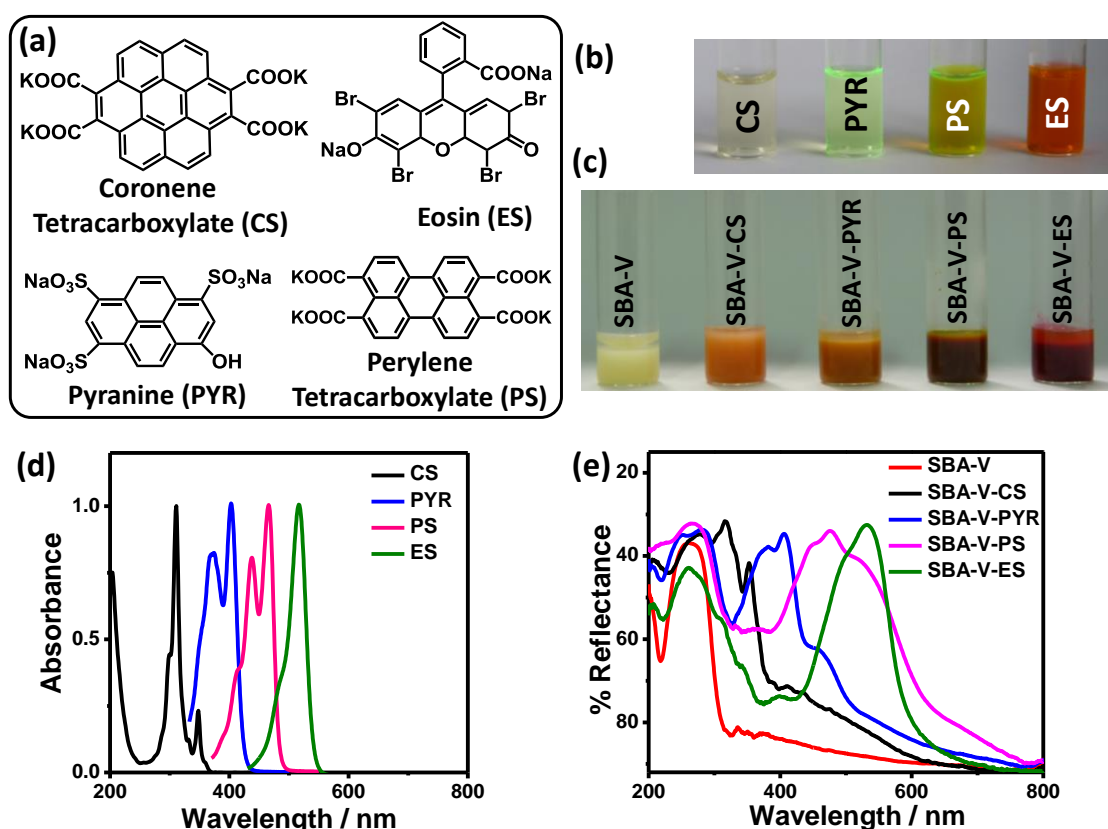


Figure 1. (a) The molecular structures of the donors used. Photographs of (b) solutions of the donors and (c) the dispersions of SBA-V bound to different donors. (d) UV-visible spectra of the

donors used for binding to SBA-V. (e) UV-visible reflectance spectra of SBA-V and SBA-V bound to various donors.

Three different donors (CS, PYR and ES) with different molecular charges were chosen so as to study the effect of molecular charge on the stoichiometry of binding. The total uptake for all these three donors was almost similar in the case of SBA-V (Figure 2) indicating that the mode of binding is one-to-one, donor-acceptor interaction. On the other hand, SBA-B exhibited different uptake behaviour for all the three donors. It can be seen that ES which has the least negative charge (two negative charges) registers the maximum uptake while CS having four negative charges shows the least uptake. In the absence of charge-transfer interactions between the donor and SBA-B, the electrostatic interactions alone control the uptake of the donor. In other words, SBA-B behaves like an ion exchange resin where the electroneutrality alone governs the uptake. The uptake of donors by SBA-B was found to be inversely related to the molecular charge on each of them (Figure 2). So, we see that in SBA-V, the strong charge-transfer interactions are responsible for the one-to-one binding of donors to the acceptor, viologen, irrespective of the different charges on the donors.

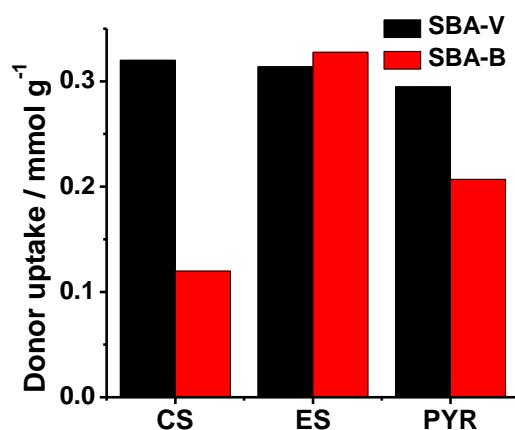


Figure 2. Uptake of different donors by SBA-V and SBA-B.

To study the selectivity of binding we chose two donors, perylene tetracarboxylate (PS) and coronene tetracarboxylate (CS), bearing similar charge but differing in their C-T binding. The absorbance maxima of both donors are well separated and do not show any interference, enabling accurate determination (Figure 3a). SBA-V soaked in an equimolar mixture of CS and PS (1.25 equivalents each), selectively bound to CS leaving the PS untouched (Figure 3b).

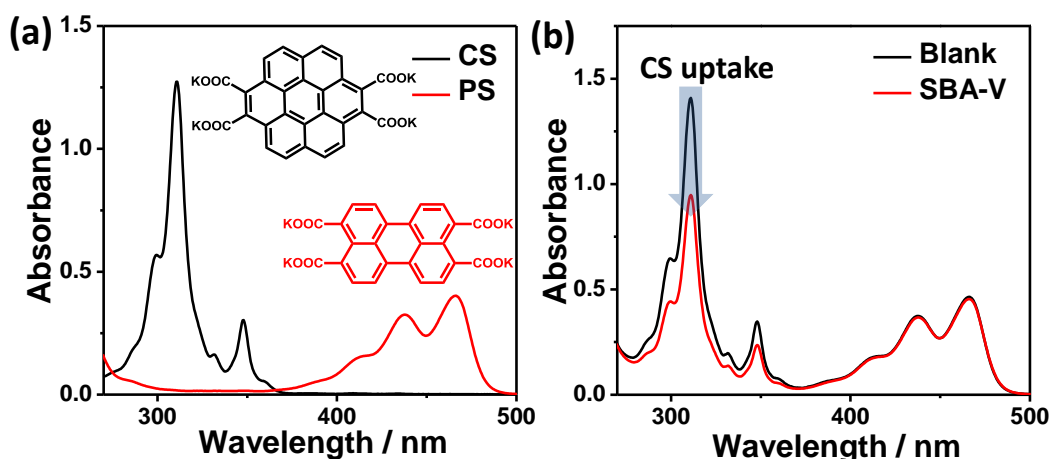


Figure 3. (a) UV-visible spectra of CS (10^{-4} M) and PS (10^{-4} M) showing widely separated absorption maxima with minimal interference. Inset showing the molecular structures of CS and PS. (b) UV-visible spectra showing exclusive uptake of CS by SBA-V from an equimolar mixture of CS and PS.

On decreasing the amount of CS and PS to 0.7 equivalents each, most of the CS in solution along with one-third of the PS was bound to SBA-V (Figure 4a). So, we see that when very less CS is left in solution then PS is capable of binding to SBA-V but when the availability of both exceeds the binding capacity of SBA-V, CS alone is exclusively bound. This is a clear case of competitive binding where CS has a stronger binding constant than PS. This was further confirmed by carrying out selective binding studies with 0.7 equivalents of each donor at higher temperature (60 °C) or at ten times dilution (Figure 4b-c). In supramolecular chemistry, both temperature and dilution work in a similar fashion.^[16] Both of them lead to breaking of the weaker viologen-PS interactions. It can be seen that even the uptake of CS is reduced to some extent on heating and dilution. Both heating and dilution reduce the total binding capacity of SBA-V, which then falls below the individual availability of both CS and PS, resulting in an increase in selective uptake (Figure 4d).

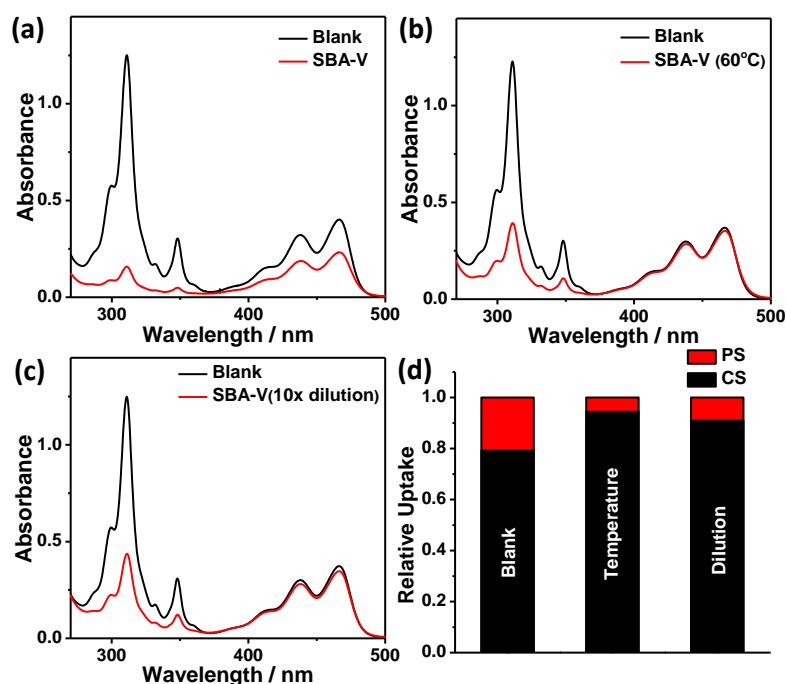


Figure 4. UV-visible spectra showing selective uptake of CS from an equimolar solution (0.7 equivalents each) of CS and PS by SBA-V (a) at room temperature, (b) at 60 °C and (c) at ten times dilution. (d) Bar graphs showing the increase in selective uptake of CS with increase in temperature to 60 °C and on dilution.

Different amounts of equimolar solution of CS and PS were added to SBA-V and based on the ratio of CS and PS bound and left unbound in supernatant, selectivity factors were calculated. The adsorption selectivity factors were calculated using the following formula:

$$\text{Adsorption selectivity factor} = \frac{[\text{CS}]_{\text{solid}} \times [\text{PS}]_{\text{solution}}}{[\text{PS}]_{\text{solid}} \times [\text{CS}]_{\text{solution}}}$$

$[\text{CS}]_{\text{solid}}$ – Amount of CS adsorbed by SBA-V; $[\text{PS}]_{\text{solid}}$ - Amount of PS adsorbed by SBA-V

The adsorption selectivity factors for SBA-V with respect to CS over PS were found to be in the range of 42-48. To understand if this high selective binding is an outcome of the native difference in binding constant/strength, solution state binding titrations between methyl viologen and the two donors were performed. The solution state selectivity is given by the ratio of their binding constants, i.e. $K_{\text{CS-MV}}/K_{\text{PS-MV}}$ which was found to be just 1.2. So we can see that viologen immobilised in SBA-V shows 38 fold enhancement of selectivity in comparison to its solution state analogue.

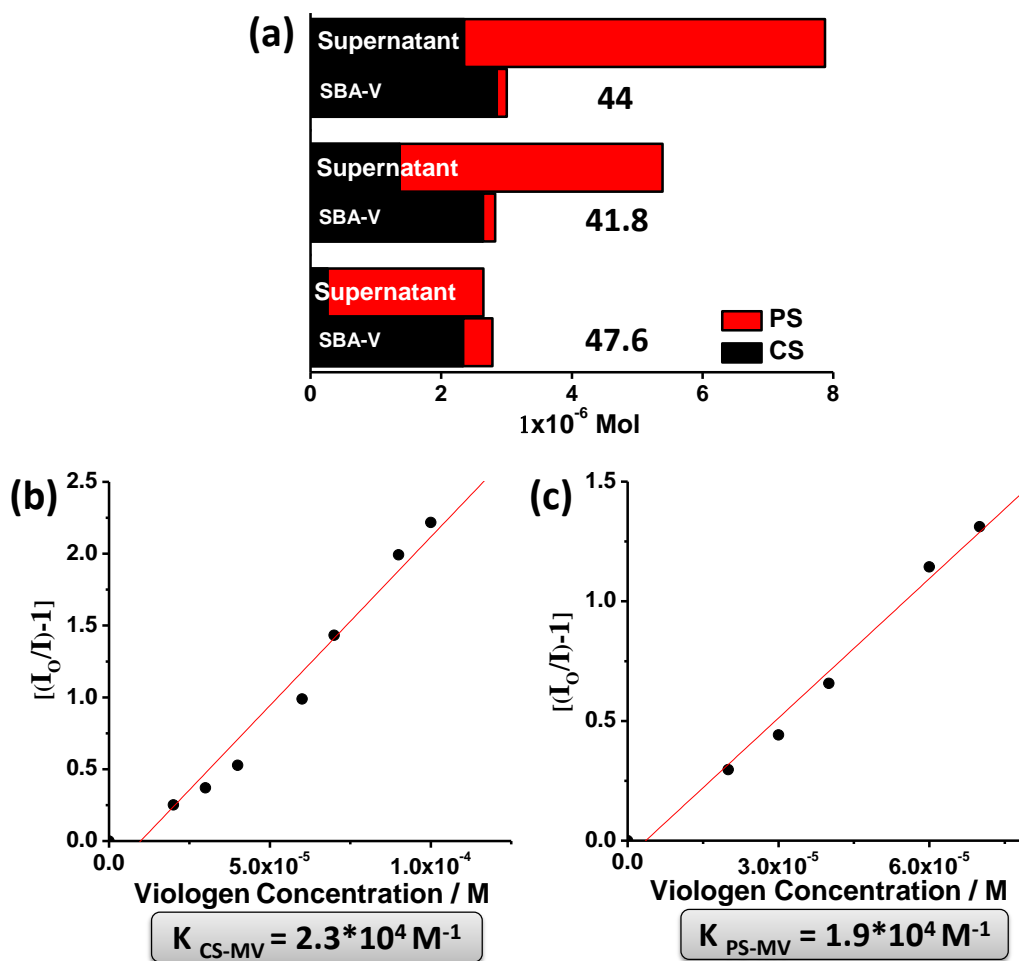


Figure 5. (a) Static selectivity binding studies of CS and PS with SBA-V using various volumes of CS/PS equimolar solutions showing adsorption selectivity factors in the range 42 - 48. Solution state binding titrations of (b) coronene tetracarboxylate (CS), and (c) perylene tetracarboxylate (PS), against methyl viologen.

The large adsorption selectivity factor would enable highly efficient dip-based single step separation of CS from mixtures of CS and PS. To check for separation in a flow-based system, breakthrough experiments were performed on a bed of SBA-V using an equimolar mixture of CS and PS. The progress of the breakthrough column was followed by collecting 100 μL fractions and analyzing them using UV-visible spectroscopy. As expected from the static binding selectivity, PS eluted faster through the column and was the first to break through in its pure form, followed by CS (Figure 5a). The separation could be followed easily since CS and PS form CT complexes with different colors (orange-brown for CS and dark brown for PS).

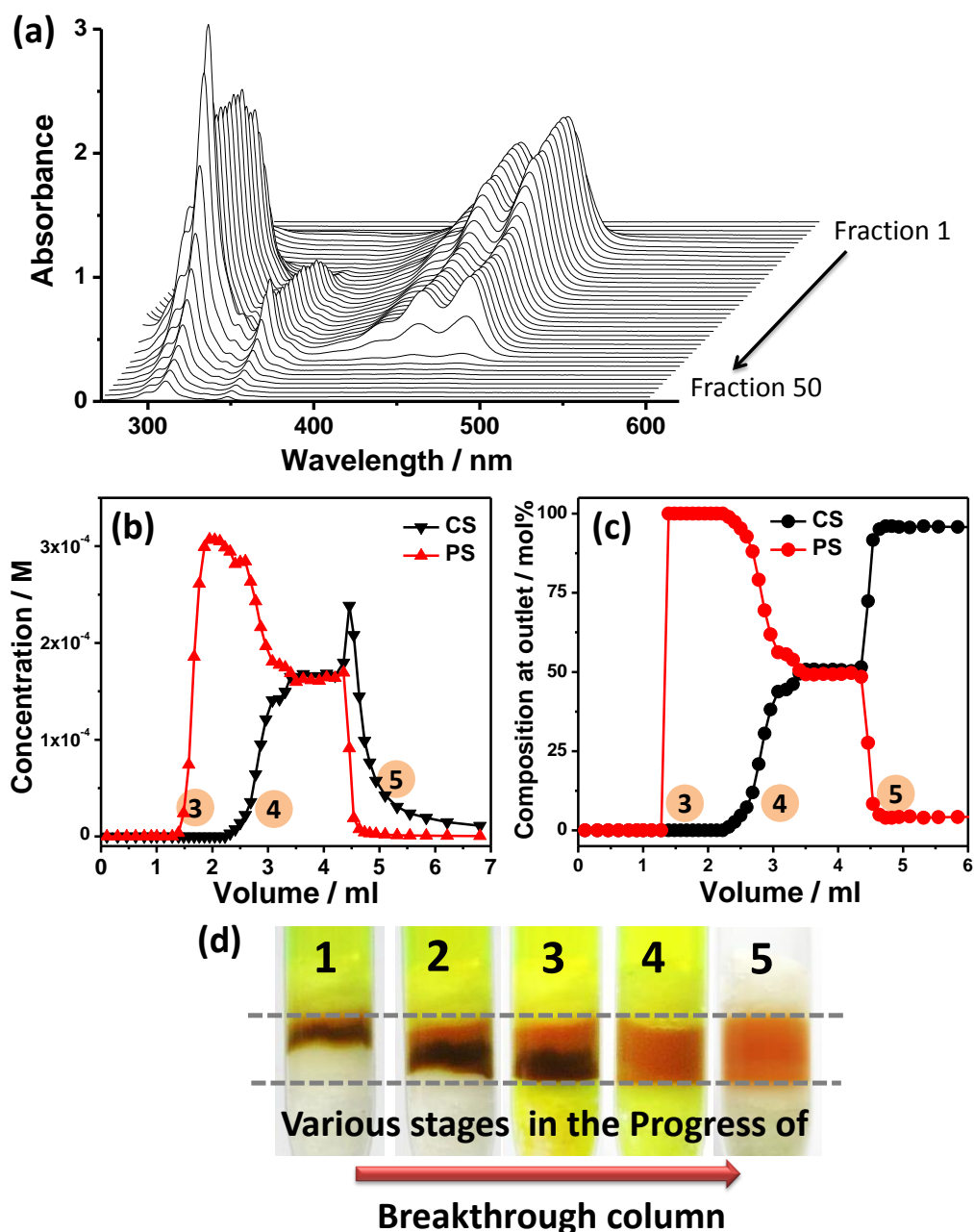


Figure 6. (a) UV-Visible spectra of the various fractions collected. (b) The concentration profile of CS and PS during the breakthrough experiment plotted against volume eluted. It shows the characteristic “roll-up” associated with displacement of weaker binding PS by stronger binding CS. (c) Experimental breakthrough curves for an equimolar mixture of CS and PS flowing through a bed of SBA-V, exhibiting clear separation and high selectivity. (d) Photographs of the bed of SBA-V (located between the dashed lines) at various stages of the breakthrough experiment. The various regions in (b) and (c) corresponding to the different stages of the breakthrough column as shown in (d) have been marked for ease of understanding.

As the feed solution passed through, it separated into a faster-traveling pure PS band and a CS-rich band [Figure 6d(2–3)]. Gradually, all of the viologen moieties became saturated with CS, at which point the outlet composition reached equimolar composition [Figure 6b(4–5)]. A water purge was then applied to elute the adsorbed contents, and the outlet molar composition quickly stabilized at CS/PS = 96:4 (Figure 6c). In order to reduce the effects of uneven packing, we used SBA as a filler material as it didn't show any selectivity to either CS or PS. Dynamic binding capacity can be calculated from the amount of donors bound during the breakthrough column during its initial stages, when all the donors passing through were getting bound to SBA-V. The dynamic binding capacity of SBA-V was found to be ~35% of its static binding capacity, which is very significant because of the high retention of efficiency even in a flow-based system.

In order to further test the capability of SBA-V in separation, we chose one more additional donor, pyrene tetrasulfonate (P4), along with CS and PS bearing the same molecular charge (Figure 7b). Even in this case, we obtained clear breakthrough curves for a three-component equimolar mixture of CS, PS, and P4 indicating the very good separation capability of SBA-V, even in flow based systems (Figure 7a). First to breakthrough the column was P4, followed by PS and then later CS. Therefore, the selectivities are in the order CS > PS > P4. The separation here is solely induced on the basis of charge transfer interactions because in terms of molecular charge they are all quadruply charged (ignoring the effects of charge density due to difference in functional group contributing the charge).

In order to understand the high selectivity exhibited by SBA-V in contrast to its solution state analogue, we modified the local environment around the viologen to see if there is an effect on the selectivity of binding. As we have seen in chapter 2, not all the iodopropyl groups react to form viologen on the pore walls of SBA-V. The reaction to form viologen moieties on the pore wall is limited by the repulsion between the viologen moieties themselves due to which some of the iodopropyl groups are left unreacted. These iodopropyl groups were reacted with azide anions to form azide groups adjacent to viologen moieties increasing the polarity of the local environment around the viologen (SBA-V_{AZ}) (Scheme 4). The infra-red spectroscopy analysis of azide modified SBA-V (SBA-V_{AZ}) showed a peak at 2100 cm⁻¹ for azide stretching vibration (Figure 8a). Nitrogen adsorption isotherms recorded on SBA-V and SBA-V_{AZ} show type IV behavior indicating a narrow pore size distribution (Figure 8b).

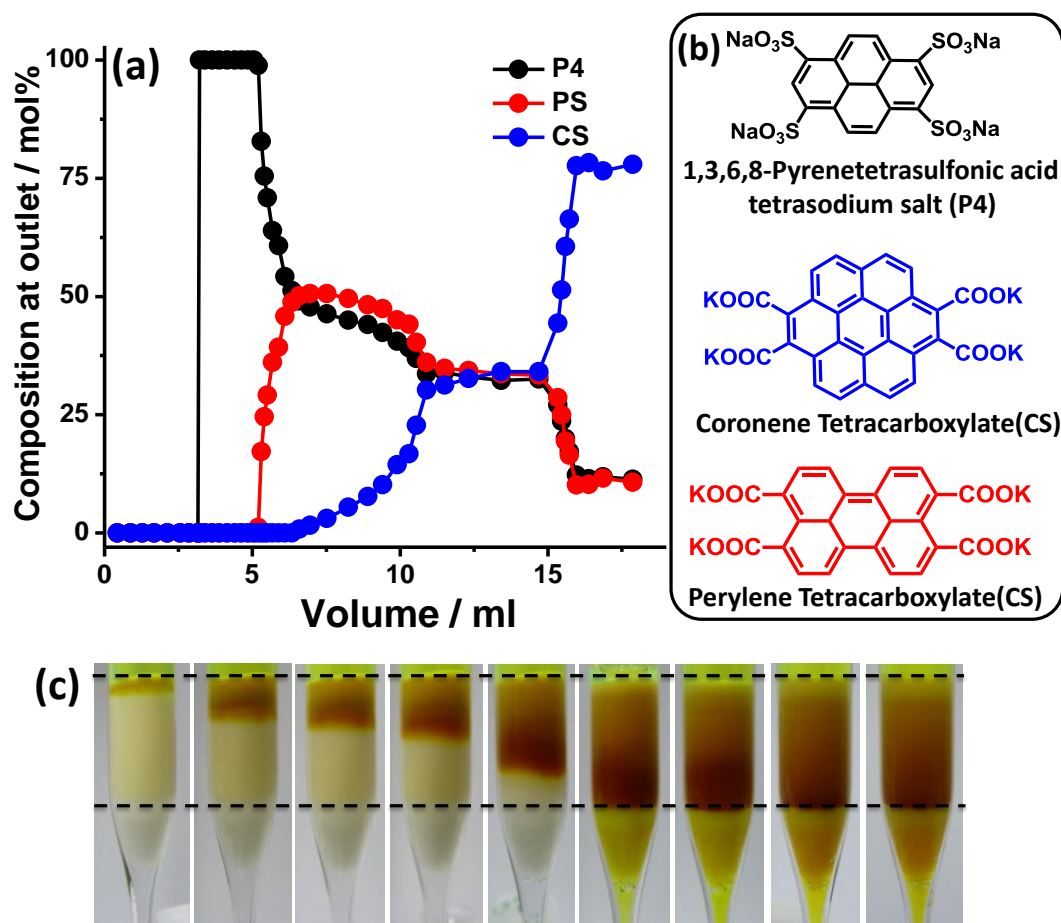
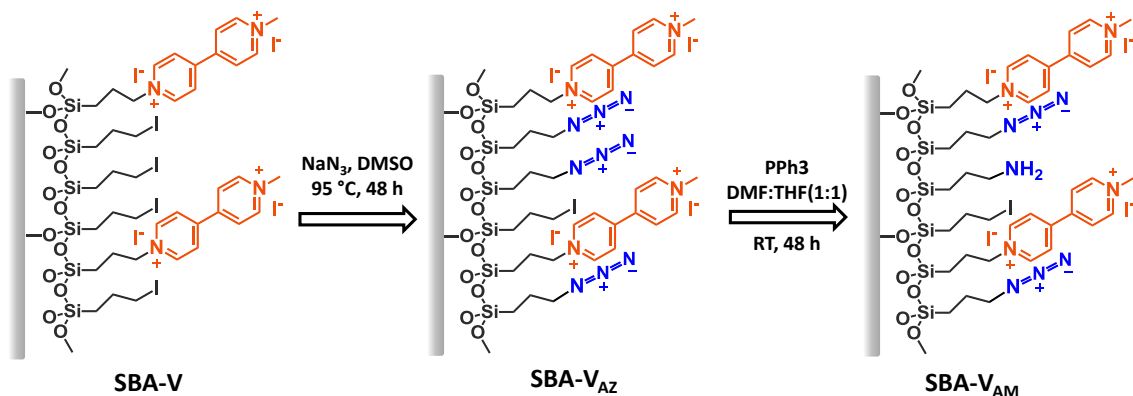


Figure 7. (a) Breakthrough curves of an equimolar mixture of CS/PS/P4 through a bed of SBA-V : SBA (1:3) showing clear separation of the three components of the mixture. (b) Molecular structures of the donors used. (c) Photographs of the bed of SBA-V, showing various stages in the progress of the breakthrough column till the attainment of equimolar composition at the outlet.



Scheme 4. Schematic showing the synthetic strategy followed for preparing SBA-V_{AZ} and SBA-V_{AM}.

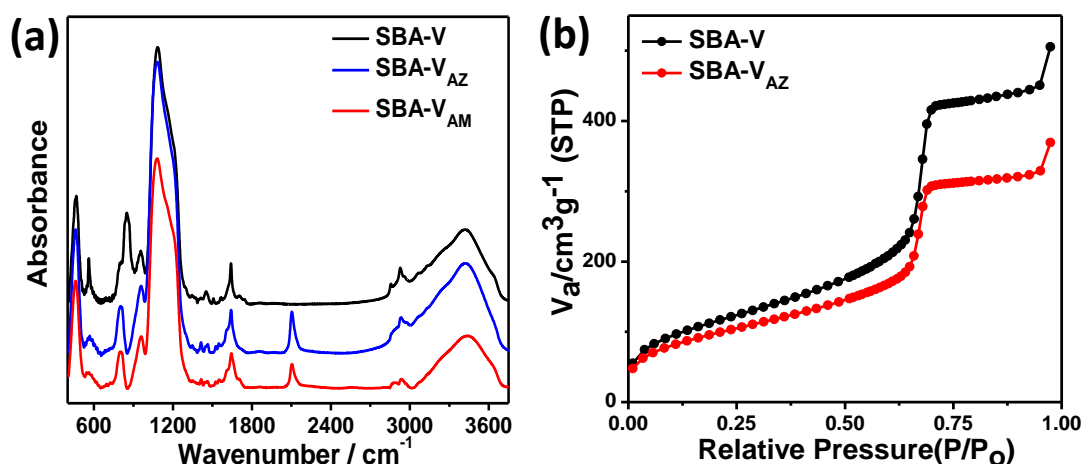


Figure 8. (a) Infra-red spectra of SBA-V, SBA-V_{AZ} and SBA-V_{AM}. (b) Nitrogen adsorption isotherms of SBA-V and SBA-V_{AZ} showing retention of pore structure on functionalization with azide moieties.

The binding capacity of SBA-V_{AZ} was found to be ten times lesser than SBA-V. This may be due to the steric hindrance caused by the azide group which could disrupt the co-facial interaction between the viologen and the donors. The dipolar nature of the azide groups could also be playing a role in hindering the approach of donors to the viologen. In order to reduce the steric hindrance, the azide group was converted partially into amine groups using the Staudinger reaction to form SBA-V_{AM} (Scheme 4). The IR spectra of SBA-V_{AM} showed a decrease in the intensity of the azide stretching peak at 2100 cm⁻¹ indicating partial conversion of azide groups into amines (Figure 8a). The IR spectra have been normalised using the Si—O—Si bending vibration at 460 cm⁻¹ for intensity calibration. The conversion of azide to amines increased the binding capacity from 0.02 mmol/g to 0.7 mmol/g. The binding studies in the presence of equimolar mixture of CS and PS were carried out to check for the effect of the local polar environment on the binding selectivity. The adsorption selectivity factors were found to be in the range of 13-17, three times smaller than the adsorption selectivity factor of SBA-V (Figure 9). So, we see that indeed on increasing the polarity of the local environment around the viologen reduces the adsorption selectivity.

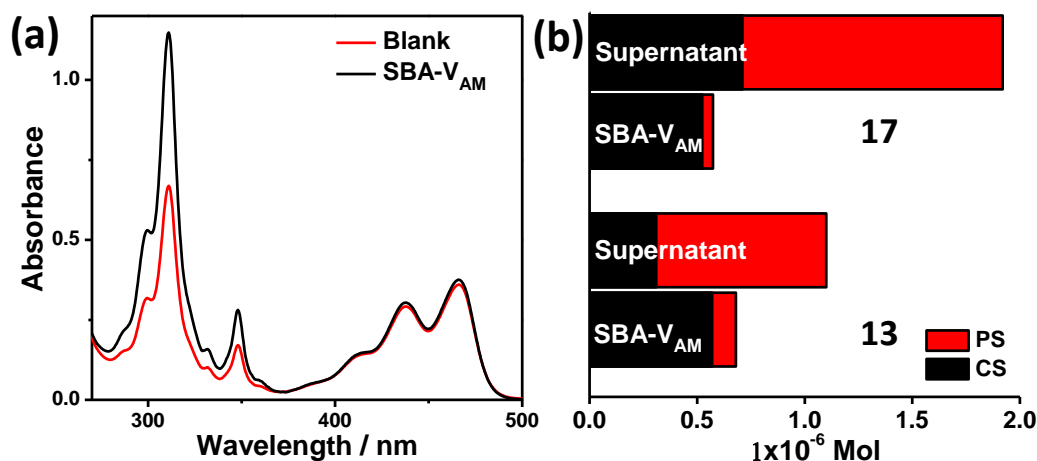
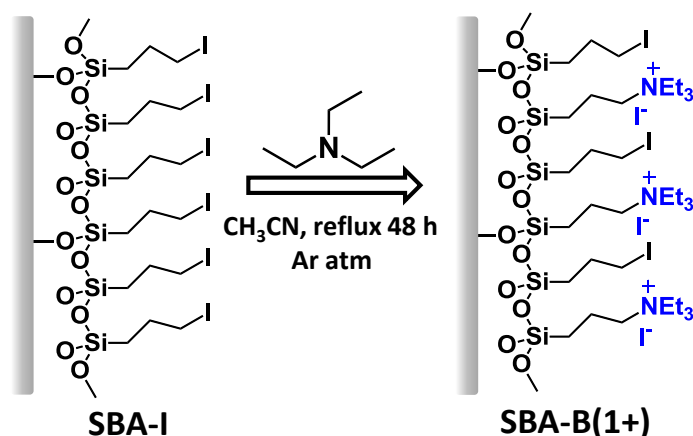


Figure 9. (a) The UV-visible spectra of the equimolar mixture of CS and PS before and after adsorption by SBA-V_{AM}. (b) Bar graphs showing the amount of CS and PS adsorbed by SBA-V_{AM} and the amount left in the supernatant for different volumes of the equimolar mixture of CS and PS used for the binding study. SBA-V_{AM} shows adsorption selectivity factors in the range of 13-17.

To further understand the importance of the non-polar environment provided by the iodopropyl groups in SBA-V, we modified SBA with monpositive ammonium moieties to serve as a control for electrostatic interactions. The SBA modified with iodopropyl groups (SBA-I) was reacted with triethylamine (Scheme 5) to functionalize monpositive ammonium salts on the pore wall [SBA-B(1+)]. In SBA-B(1+), the positively charged moieties are surrounded by the unreacted iodopropyl groups (Scheme 5) and hence will aid in understanding the effect of non-polar environment on electrostatically mediated binding of donors.



Scheme 5. Synthetic strategy for the preparation of SBA-B(1+).

SBA-B(1+) showed zeta potential distribution with a mean value of +30 mV indicating positively charged particles (Figure 10a). The nitrogen adsorption isotherms showed type IV

behavior, characteristic of mesoporous materials with a narrow pore size distribution (Figure 10b). This indicates that the functionalization of the mesopores was more or less uniform. Selective binding studies were carried out to calculate the adsorption selectivity factors. The selectivity factors for SBA-B(1+) were found to be in the range 3-4 (Figure 11a). So, we see that in the absence of strong C-T interactions, non-polar environment can only increase the selectivity factor to about 4. Nonetheless, it also means that non-polar environment has a role to play in determining the selectivity of binding.

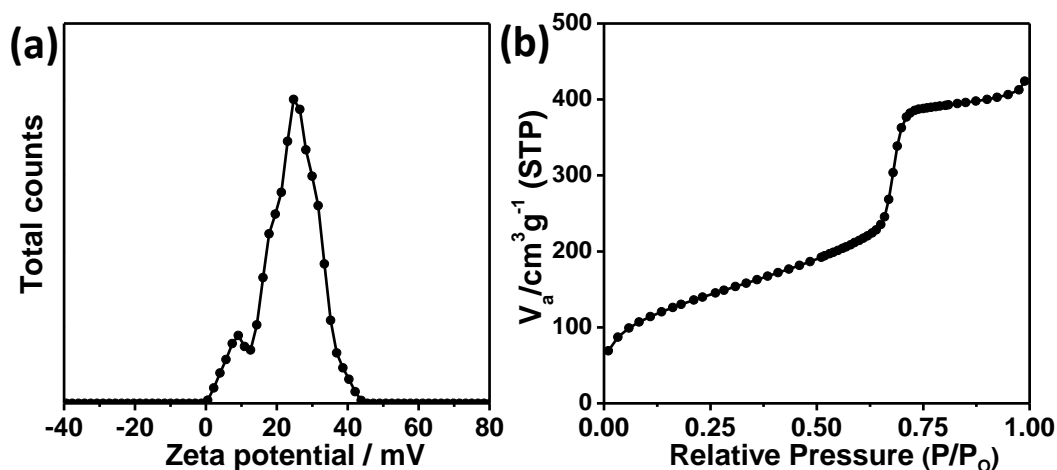


Figure 10. (a) Zeta potential distribution of SBA-B(1+) showing positively charged particles. (b) Nitrogen adsorption isotherms of SBA-B(1+) exhibiting type IV behavior.

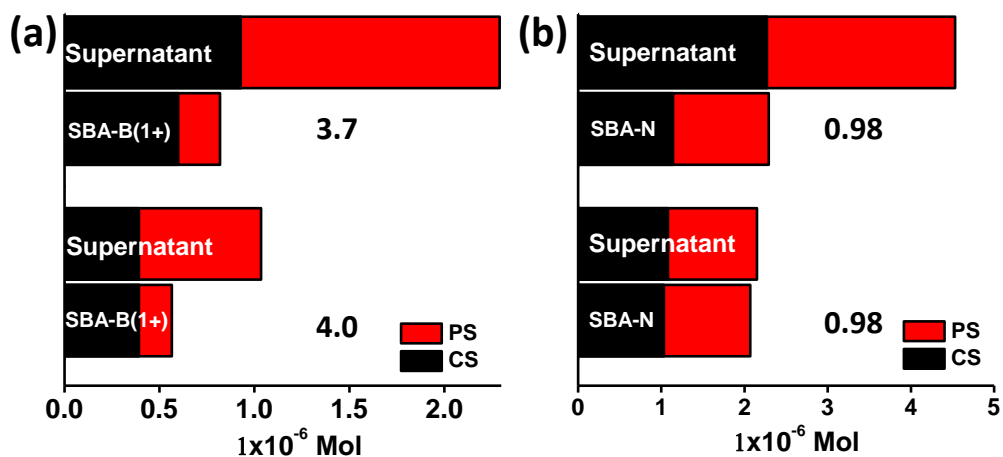


Figure 11. Bar graphs showing the uptake of donors (CS and PS) and the amount of donors left in the supernatant after adsorption by (a) SBA-B(1+) and (b) SBA-N for different volumes of the equimolar mixture of CS and PS used for the binding study.

In order to verify if the non-polar environment really has a role in determining the selectivity, we used aminopropyl modified SBA (SBA-N) which has positively charged ammonium groups along with amines which provide a polar environment. So, this would serve

would serve as a blank of just electrostatic interactions without the non-polar component. Interestingly, the binding studies showed no selectivity whatsoever for either CS or PS (Figure 12a-b). Both of them were equally adsorbed onto SBA-N. The adsorption selectivity factor was 1, implying no selectivity (Figure 11b). So, we see that non-polar environment does play a role in determining selectivity. If coupled with strong C-T interaction it results in very high selectivity (selectivity factor ~ 45) but if coupled to weak electrostatic interaction only gives a selectivity of 3-4. Though the discussion so far has focused only on the selectivity exhibited for CS over PS, it is likely to have a general implication in tuning the selective binding of donors based on the size of their π -core and molecular charge.

3.6. Conclusions

We have shown that SBA-V exhibits a very high degree of selectivity in binding to various donors and can discriminate them based on the charge as well as C-T interactions. Very high selectivity factors in the range of 42-48 were obtained which was a 38-fold enhancement when compared to its solution state analogue (methyl viologen). The enhanced selectivity of SBA-V enables facile separation of highly water-soluble donors that cannot be separated through conventional strategies. This high selectivity of binding was employed to fabricate a breakthrough column which can discriminate different donors based on C-T interactions. Clean breakthrough curves were obtained even for a three component mixture of donors having the same charge but different C-T interactions. The degree of selectivity was found to be dependent on the polarity of the environment around the viologen moieties. This was further studied using a series of control experiments to discern the role of the local environment around viologen (Figure 12).

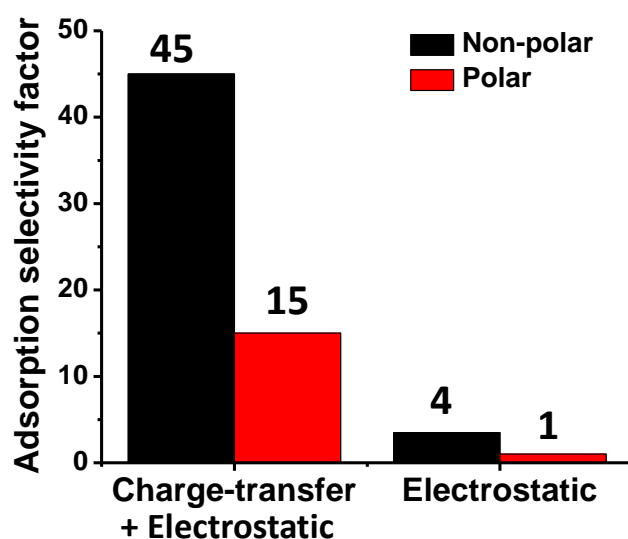


Figure 12. A brief overview of the various selectivity factors obtained by modifying the polarity of the environment and the nature of interactions (C-T or electrostatic).

3.7. References

- [1] K. K. R. Datta, D. Jagadeesan, C. Kulkarni, A. Kamath, R. Datta, M. Eswaramoorthy, *Angew. Chem. Int. Ed.* **2011**, *50*, 3929-3933.
- [2] a) B. O. Okesola, D. K. Smith, *Chem. Commun.* **2013**, *49*, 11164-11166; b) F. Rodriguez-Llansola, B. Escuder, J. F. Miravet, D. Hermida-Merino, I. W. Hamley, C. J. Cardin, W. Hayes, *Chem. Commun.* **2010**, *46*, 7960-7962.
- [3] a) X. Zhao, X. Bu, T. Wu, S.-T. Zheng, L. Wang, P. Feng, *Nat Commun* **2013**, *4*; b) C. Zou, Z. Zhang, X. Xu, Q. Gong, J. Li, C.-D. Wu, *J. Am. Chem. Soc.* **2011**, *134*, 87-90.
- [4] J. E. Lofgreen, I. L. Moudrakovski, G. A. Ozin, *ACS Nano* **2011**, *5*, 2277-2287.
- [5] a) G. Wulff, A. Sarhan, *Angew. Chem., Int. Ed. Engl.* **1972**, *11*, 341; b) T. Takagishi, I. M. Klotz, *Biopolymers* **1972**, *11*, 483-491.
- [6] A.-X. Yan, S. Yao, Y.-G. Li, Z.-M. Zhang, Y. Lu, W.-L. Chen, E.-B. Wang, *Chemistry – A European Journal* **2014**, *20*, 6927-6933.
- [7] C. Alexander, H. S. Andersson, L. I. Andersson, R. J. Ansell, N. Kirsch, I. A. Nicholls, J. O'Mahony, M. J. Whitcombe, *J. Mol. Recognit.* **2006**, *19*, 106-180.
- [8] R. Curti, U. Colombo, *J. Am. Chem. Soc.* **1952**, *74*, 3961.
- [9] M. V. Polyakov, L. P. Kuleshina, I. E. Neimark, *Zh. Fiz. Khim.* **1937**, *10*, 100-112.
- [10] A. Katz, M. E. Davis, *Nature (London)* **2000**, *403*, 286-289.
- [11] a) B. M. Jung, M. S. Kim, W. J. Kim, J. Y. Chang, *Chem. Commun.* **2010**, *46*, 3699-3701; b) S. Dai, M. C. Burleigh, Y. H. Ju, H. J. Gao, J. S. Lin, S. J. Pennycook, C. E. Barnes, Z. L. Xue, *J. Am. Chem. Soc.* **2000**, *122*, 992-993.
- [12] K. Ariga, A. Vinu, Q. Ji, O. Ohmori, J. P. Hill, S. Acharya, J. Koike, S. Shiratori, *Angew. Chem. Int. Ed.* **2008**, *47*, 7254-7257.
- [13] A. Sayari, B.-H. Han, Y. Yang, *J. Am. Chem. Soc.* **2004**, *126*, 14348-14349.
- [14] a) D. Britt, D. Tranchemontagne, O. M. Yaghi, *Proceedings of the National Academy of Sciences* **2008**, *105*, 11623-11627; b) M. S. P. Silva, M. A. Moreira, A. F. P. Ferreira, J. C. Santos, V. M. T. M. Silva, P. Sá Gomes, M. Minceva, J. P. B. Mota, A. E. Rodrigues, *Chem. Eng. Technol.* **2012**, *35*, 1777-1785; c) E. Santacesaria, M.

- Morbidelli, A. Servida, G. Storti, S. Carra, *Industrial & Engineering Chemistry Process Design and Development* **1982**, *21*, 446-451.
- [15] a) D. A. Walker, E. K. Leitsch, R. J. Nap, I. Szleifer, B. A. Grzybowski, *Nat. Nanotechnol.* **2013**, *8*, 676-681; b) D. Wang, R. J. Nap, I. Lagzi, B. Kowalczyk, S. Han, B. A. Grzybowski, I. Szleifer, *J. Am. Chem. Soc.* **2011**, *133*, 2192-2197.
- [16] P. A. Korevaar, C. Schaefer, T. F. A. de Greef, E. W. Meijer, *J. Am. Chem. Soc.* **2012**, *134*, 13482-13491.

CHAPTER 4

Surface Charge Reversal

Chapter 4.1 : *Supramolecular gating of Ion Transport in Nanochannels*

Chapter 4.2 : *A Generic Strategy to Improve the Non-covalent Gating of Ion Transport using Auxillary Hydrophobic Interactions*

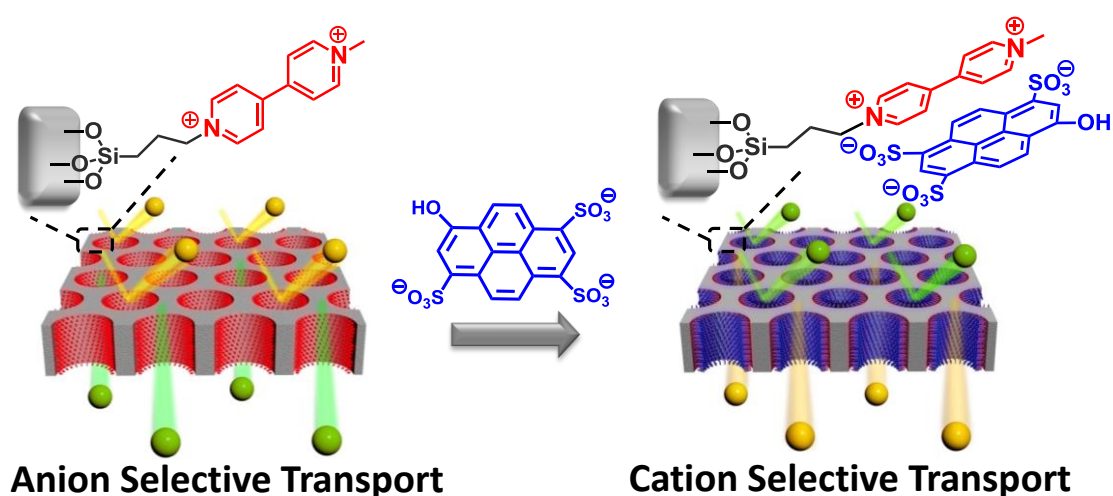
Chapter 4.3 : *Glucose- and pH-Responsive Charge-Reversal Surfaces*

Chapter-4.1

Supramolecular Gating of Ion Transport in Nanochannels

Summary

Several covalent strategies towards surface charge-reversal in nanochannels have been reported with the purpose of manipulating ion transport. However, covalent routes lack dynamism, modularity and post synthetic flexibility, and hence restrict their applicability in different environments. Here, we introduce a facile non-covalent approach towards charge-reversal in nanochannels (<10 nm) using strong charge-transfer interactions between di-positive viologen (acceptor) and tri-negative pyranine (donor). The polarity of ion transport was switched from anion selective to cation selective through ambipolar stage by controlling the extent of pyranine bound to the viologen. Further, we could also regulate the ion transport with respect to pH by selecting a donor (coronene tetracarboxylate) with pH responsive functional groups. The modularity of this approach further allows facile integration of various functional groups capable of responding to stimuli such as light and temperature to modulate the transport of ions as well as molecules.



Publication based on this work has appeared in *Angew. Chem. Int. Ed.*, **2014**, DOI: 10.1002/anie.201406448.

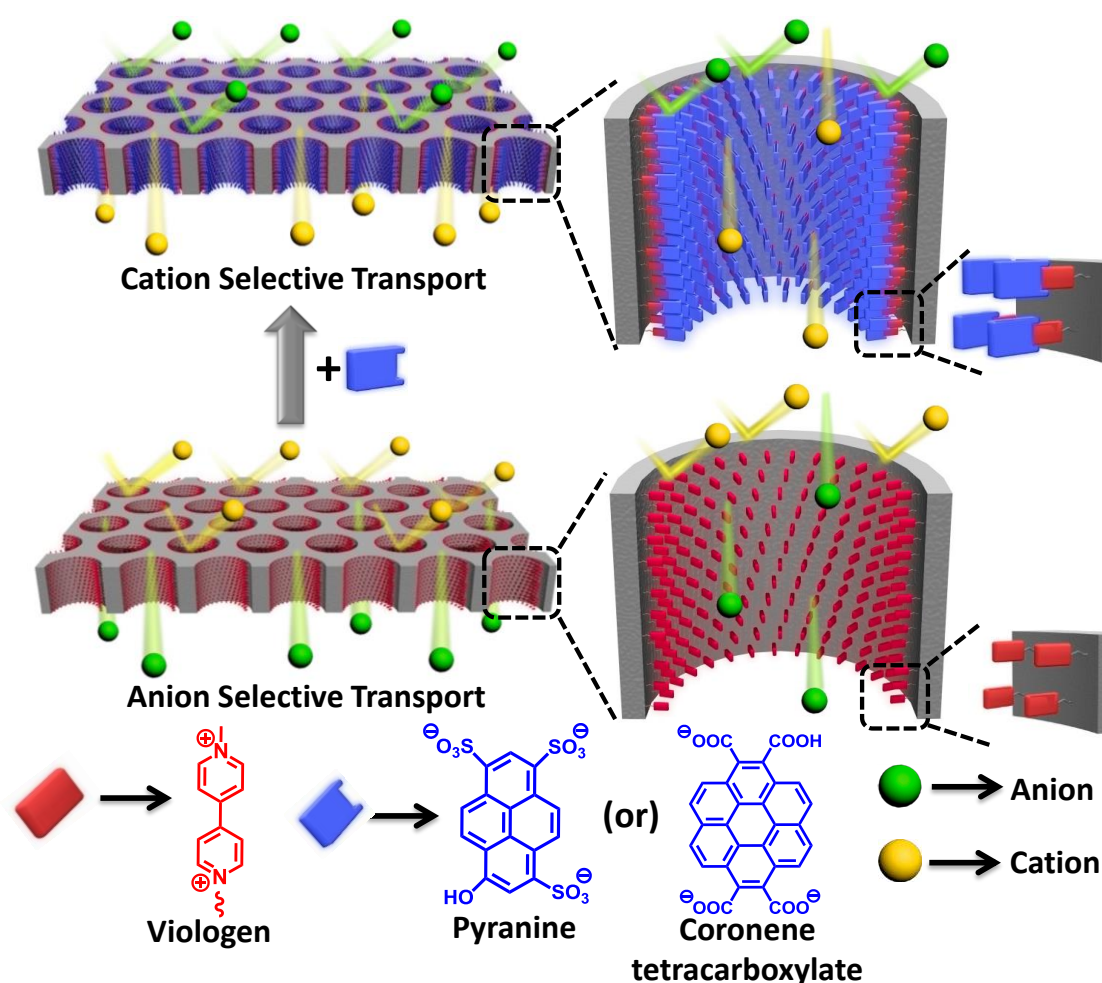
4.1.1. Introduction

Biological systems employ protein nanochannels to regulate ion transport which is vital for maintaining their integrity and communication with extracellular environment.^[1] Design of abiotic analogues to manipulate ion transport through nanochannels has gained tremendous attention in recent years, considering their role in the development of ionic circuits for sensing, switching and amplifying the chemical identities from aqueous environment.^[2] Nanochannels with charged surfaces having pore dimensions within the Debye length range, are known to display selective transport properties associated with the surface charge dependent enhancement^[3] and depletion phenomenon.^[4] Thus, control of surface charge within the nanochannel is critical for effective gating and rectification of ion transport^[5]. Manipulation of surface charge in nanochannels of size less than 10 nm is of biological relevance since at physiological salt concentrations the Debye length is in the range of few nanometers. Nanochannels having charge-reversal surfaces would be able to switch the polarity of ion transport from cation selective to anion selective and are ideal candidates for gating and rectification. To achieve charge-reversal, surfaces were often covalently functionalized with pH-^[6] or light-^[7] responsive functional groups such as aminoacids^[8] and spiropyrans.^[9] However, the covalent functionalization to a larger extent lacks dynamism, modularity and post synthetic flexibility and hence, restricts its wider applicability in different environments. On the other hand, non-covalent functionalization, notwithstanding its ability to overcome some of these limitations, has not been successful so far in confined environments (<10 nm). Since, non-covalent approach largely relied on electrostatic interactions, it is unlikely to attain charge-reversal in confined spaces where the penalty for charge accumulation is high.^[10] In order to realize charge-reversal and hence, the control of ion permeation in nanopores/nanochannels through non-covalent approach, one has to overcome the electrostatic repulsion of “like” charges through strong orthogonal interactions. The modular nature of non-covalent functionalization would enable use of a variety of non-covalent motifs to modulate surface charge in response to multiple stimuli.

4.1.2. Scope of the present investigation

Mixed charge transfer modules, in which donor and acceptor aromatic molecules are co-facially arranged, have recently emerged as strong supramolecular motifs for the formation of supramolecular polymers^[11] and charge-transfer nanostructures.^[12] In chapter 2, we have seen that the non-covalent C-T interactions between covalently immobilized viologen and free pyranine analogues can be exploited to tune the pore size and philicity of mesoporous silica SBA-15.^[13] The unusually strong C-T interactions (binding constant $\sim 10^5$ - 10^6 M⁻¹) between the positively charged acceptor and negatively charged donor, led us to believe that the surface

charge could be controlled non-covalently by using donors of different molecular charges. To understand the ability of these strong supramolecular motifs in attaining charge-reversal within the confined nanopores (< 10 nm) and their concomitant role in gating of ion transport, cyclic voltammetric studies were carried out over viologen modified mesoporous silica film prepared on a conducting ITO substrate. In this chapter, non-covalent, charge-transfer (C-T) based supramolecular motifs have been used to obtain charge-reversal surfaces inside the nanopores and demonstrated their ion gating ability (Scheme 1). By employing pyranine as the donor and viologen as the acceptor we manipulated the surface charge inside the nanopores from positive to neutral or negative. pH-responsive switching of ion transport was also achieved through the use of coronene tetracarboxylate donor.



Scheme 1. Non-covalent functionalization of viologen modified nanopores with negatively charged donor, pyranine (or coronene tetracarboxylate), to switch the gating properties of the nanopores from anion selective to cation selective.

4.1.3. Experimental section

Viologen functionalized mesoporous silica film (MF-V)

Mesoporous silica film (MF). Mesoporous silica films (MF) were synthesized using a sol gel method based on tetraethoxysilane (TEOS) as the oxide precursor in the presence of non-ionic block copolymer, Pluronic F127 as the template. The precursor solution was prepared with the following composition: 1 TEOS: 0.0075 F127: 24 EtOH: 5.2 H₂O: 0.28 HCl. ITO slides were then dip coated with precursor solution at a withdrawing speed of 1.5 mm s⁻¹ and at a relative humidity of 40-50 %.^[14] The freshly deposited films were placed in a chamber maintained at 50% relative humidity for 1 h. The relative humidity in the chamber was maintained using a saturated solution of potassium carbonate which is known to give a relative humidity of 43 %. The dip coated slides were subjected to thermal treatment at 60 °C (for 1 h) and 130 °C (for 1 h) before calcining them at 350 °C for 2 h.

Iodopropyl functionalized mesoporous silica films (MF-I). The calcined mesoporous silica films were degassed and then hydrated in a humidity chamber at 50 % relative humidity for 1 h and added into 20 mL of degassed toluene along with 1.0 mL of (3-iodopropyl)trimethoxysilane (5 mmol) and left overnight. The temperature was increased to 110 °C and held for 6 h to complete the reaction. The iodopropyl functionalized films were washed thoroughly with ethanol and finally subjected to soxhlet extraction in ethanol to completely wash away uncondensed silane from the pores.

Viologen functionalized mesoporous silica films (MF-V). The MF-I films were degassed at 80 °C for 3 h. To this 0.6 g (2 mmol) of N-methyl-4,4'-bipyridinium iodide dissolved in 30 mL of degassed acetonitrile (CH₃CN) was added and refluxed for 3-4 days. The MF-V obtained were washed with ethanol and subjected to soxhlet extraction with ethanol.

Viologen Functionalized SBA (SBA-V). The experimental procedure followed was same as given in chapter 2.

MF-B (Ionic blank).

The MF-I films degassed at 80 °C were added to 25 mL of degassed acetonitrile containing 0.22 g (2 mmol) of 1,4-diazabicyclo[2.2.2]octane (DABCO) and refluxed for 3-4 days (2 mmol of tetrabutylammonium bromide was also added). It was subjected to soxhlet extraction in ethanol and then reacted with excess methyl iodide (40 mmol) in 25 mL acetonitrile for 6 h at 60 °C to obtain ionic hybrid, MF-B. Protocol for workup was similar to MF-V.

SBA-B. The experimental procedure followed was same as given in chapter 2.

Digestion of MF-V. The MF-V films were digested in a 4 M solution of NH_4F at 60 °C for 10 minutes and analyzed using UV-visible spectroscopy in a 1 mm quartz cuvette.

TEM Sample Preparation. The mesoporous silica films coated on ITO were soaked in 6 M HCl solution overnight to lift off the films from the ITO. The films were centrifuged and washed with ethanol to remove any excess acid.

pH titration of coronene tetracarboxylate

10 ml of 0.8 mM solution of coronene tetracarboxylate salt was taken in a vial and degassed for 15 minutes. 20 μL aliquots of 0.1 M HCl were added to the donor solution and the pH was monitored after every addition. A nitrogen blanket was maintained over the solution in order to prevent interference from dissolution of carbon dioxide in water.

Voltammetry measurements.

Cyclic voltammetry measurements were performed with ITO slides coated with mesoporous silica films as working electrodes, platinum wire as counter electrode and aqueous Ag/AgCl as reference electrode. MF-V films were soaked for 16 h in 1 mM solutions of the respective donors to allow for the completion of charge-transfer complex formation prior to the voltammetry measurements. The transport of positively charged $[\text{Ru}(\text{NH}_3)_6]^{3+}$ and negatively charged $[\text{Fe}(\text{CN})_6]^{3-}$ redox probes through the films was monitored using cyclic voltammetry to follow the change in transport properties of the mesoporous silica films. All voltammetric measurements were performed using 1 mM solutions of the redox probe with 0.1 M KCl as the supporting electrolyte at a scan rate of 200 mV/s. In the case of the studies on MF-V and MF-B films with pyranine, the voltammetric measurements were performed in presence of 5×10^{-4} M pyranine. This was to ensure stable electrochemical measurements since the binding of donors to viologen is non-covalent in nature and hence in the absence of donor in solution some amount of donor would unbind from viologen. The pH was adjusted using acetic acid (0.1 M) and NaOH (0.1 M) for studying the pH responsive properties of coronene tetracarboxylate (CS) bound MF-V films. In the case of CS bound MF-V films, the electrochemical currents were stable without the presence of donor in solution for short periods of time. However, in the experiment where we showed switching of ion transport with pH for three cycles, the film was soaked in a 1mM solution of CS for 15 minutes after every cycle to ensure good performance.

Zeta potential measurements

1.5 mg of SBA-V or SBA-B was weighed into separate vials and increasing amounts of pyranine were added into the vials and the volume was made up to 0.5 mL. They were stirred for 4 h and then diluted to 5 ml for recording zeta potential measurements.

4.1.4. Characterization

Please refer to the appendix for the instrumental details of UV-visible spectroscopy, diffuse reflectance infra-red fourier transform spectroscopy (DRIFTS), voltammetry, profilometry, TEM and zeta potential measurements.

4.1.5. Results and discussion

In chapter 2, we have demonstrated that the strong non-covalent C-T interactions between covalently immobilized viologen and free pyranine can be exploited to tune the pore size and philicity of mesoporous silica SBA-15^[13]. The unusually strong C-T interactions (binding constant $\sim 10^5 \text{ M}^{-1}$) between the di-positively charged acceptor (viologen) and tri-negatively charged donor (pyranine), led us to believe that we would be able to reverse the surface charge since the donor has more negative charge than the positive charge on the acceptor in a one-to-one binding. The zeta potential measurements on SBA-V particles indeed show a reversal of charge on addition of pyranine indicating that the binding is strong enough to induce charge reversal (Figure 1a-b). SBA-V shows a gradual decrease in zeta potential with increasing amount of pyranine added. The zeta potential decreases from +30 mV for SBA-V to -25 mV for SBA-V bound on addition of 0.6 mmol of pyranine. The change in zeta potential becomes negligible at around 0.3 mmol of pyranine added per gram of SBA-V which is the total binding capacity for SBA-V. At around 0.2 mmol/g of pyranine addition (two-thirds of the total binding capacity), the zeta potential nearly goes to zero, possibly due to the fact that trinegative pyranine required to neutralize the dipositive viologen is only two-third of the amount of viologen (Figure 1a). It can be understood that to neutralise a surface charge due to dipositive viologen moieties at least two-thirds of them should be bound to pyranine which bears three negative charges. SBA-B (functionalised with dipositive ammonium salt of DABCO), on the other hand doesn't show any signs of charge-reversal on addition of pyranine. It shows a decrease in zeta potential from +25 mV to +5 mV on addition of 0.6 mmol/g of pyranine (Figure 1a and 1c). This observation clearly signifies the indispensable role of C-T interaction in the charge-reversal phenomenon. Furthermore, to show the general nature of this approach to attain charge reversal on any surface, we modified stöber silica spheres with viologen silane (SS-V) which on addition of pyranine induces charge reversal (Figure 1d).

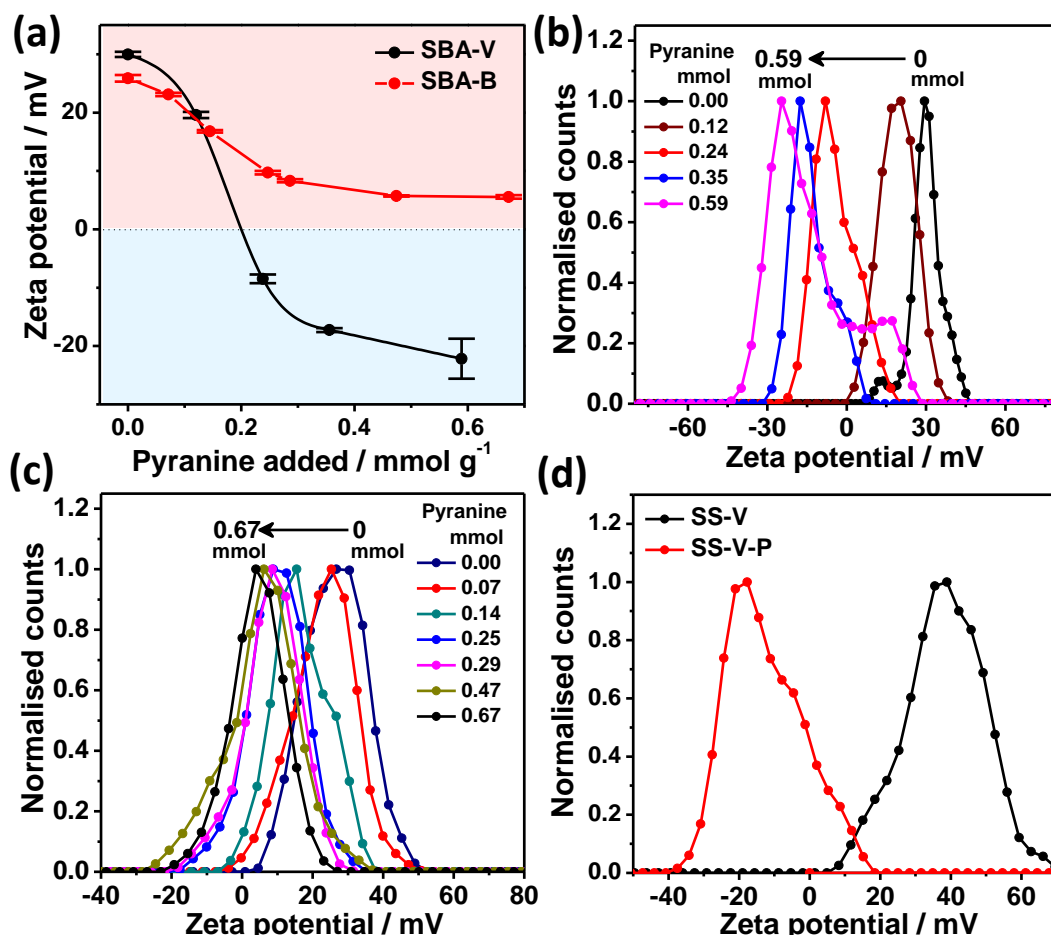
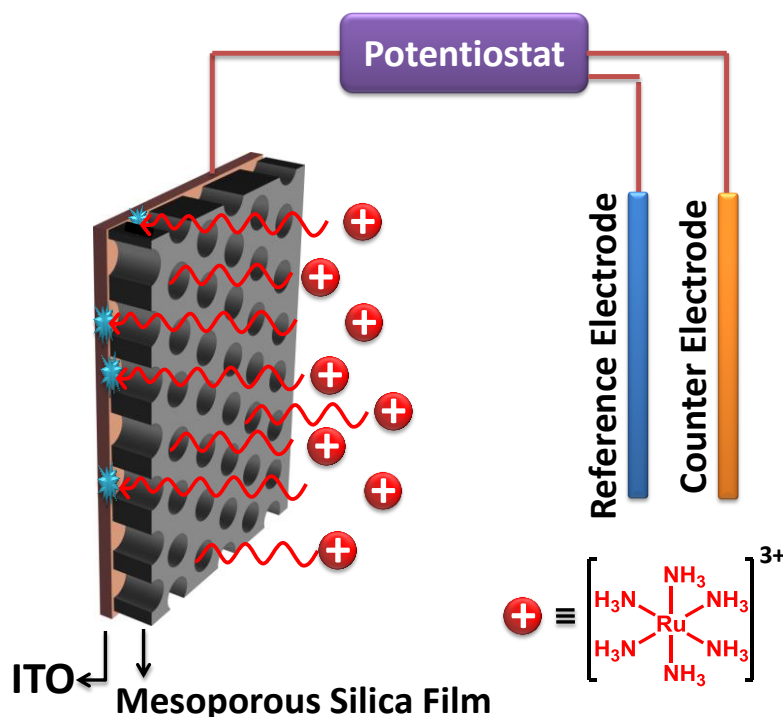


Figure 1. (a) Change in zeta potential for SBA-V and SBA-B with incremental addition of pyranine. (b) Shift in zeta potential distribution of SBA-V on addition of pyranine from positive to negative side indicates surface charge reversal. (c) Zeta potential distributions of SBA-B on addition of pyranine show neutralization of the positively charged surface of SBA-B by electrostatic adsorption of pyranine. (d) Stöber spheres modified with viologen silane (SS-V) show reversal of charge from +40 mV to -20 mV on binding to pyranine (SS-V-P).

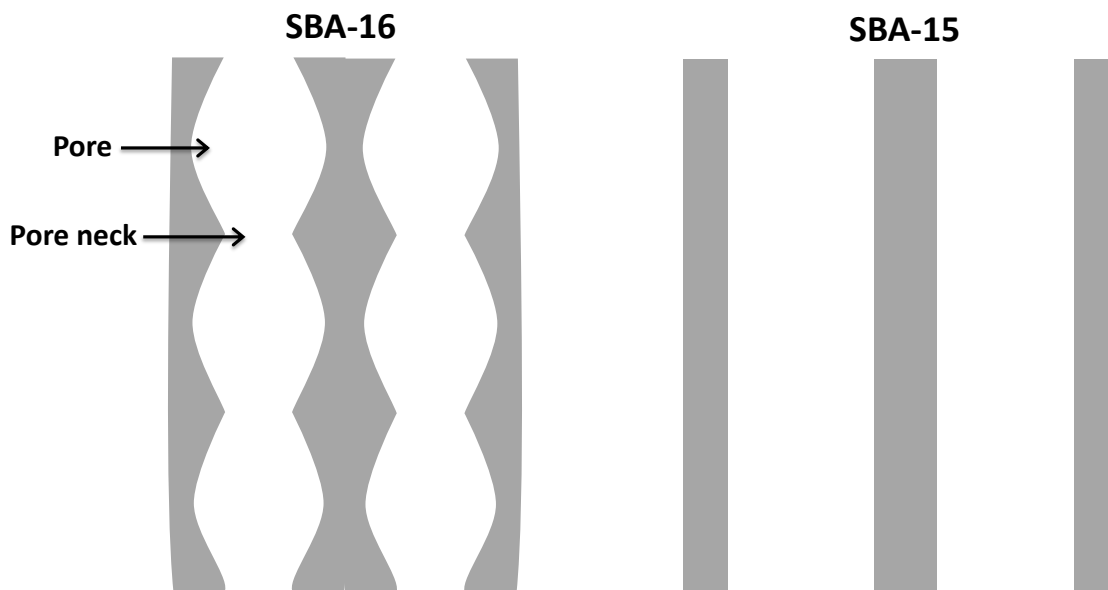
Though zeta potential measurements indicate reversal of surface charge in SBA-V particles on binding to pyranine, this doesn't necessarily mean that the surface charge inside the pores has been reversed as well. The ion transport properties of nanopores are dictated by the nature of charges on the pore walls. Hence, to understand the ability of these strong supramolecular motifs in attaining charge-reversal within the confined nanopores (< 10 nm) and their concomitant role in gating of ion transport, viologen modified mesoporous silica films were prepared on a conducting ITO substrate for probing the change in their transport properties on binding to pyranine. The transport properties of the films were studied by following the diffusion of positively $[\text{Ru}(\text{NH}_3)_6]^{3+}$ or negatively $[\text{Fe}(\text{CN})_6]^{3-}$ charged redox probes through them using cyclic voltammetry. The typical setup used for recording these cyclic voltammograms is shown in Scheme 2. The redox probes have to diffuse through the

mesoporous silica film to undergo redox processes at the ITO (working electrode) in order to give a signal in the cyclic voltammogram.



Scheme 2. Illustration showing the experimental setup used for recording cyclic voltammograms on the films to probe the transport properties of pores. Here, positive redox probes (hexammineruthenium) are shown to diffuse through the mesoporous silica film to undergo reduction at the ITO.

The mesoporous silica films, SBA-16, were prepared on ITO substrates^[15] by dip coating a sol of tetraethylorthosilicate in presence of non-ionic block-copolymer template Pluronic F127.^[14] It should be noted that pore geometry in SBA-16 is different from SBA-15 used in chapter 2. In SBA-16, the pores form a three dimensional network with the interconnection between the pores forming a neck (6 nm) with a smaller diameter than the pore (10-11 nm). SBA-15 on the other hand, has straight walled tubular pores (Scheme 3). The TEM images of the calcined film show existence of mesopores in the size range of 8-10 nm (Figure 2a-b).



Scheme 3. Illustration showing the difference in pore geometry of SBA-16 and SBA-15. SBA-16 shows pores connected through pore necks and SBA-15 has straight walled pores without any interconnectivity.

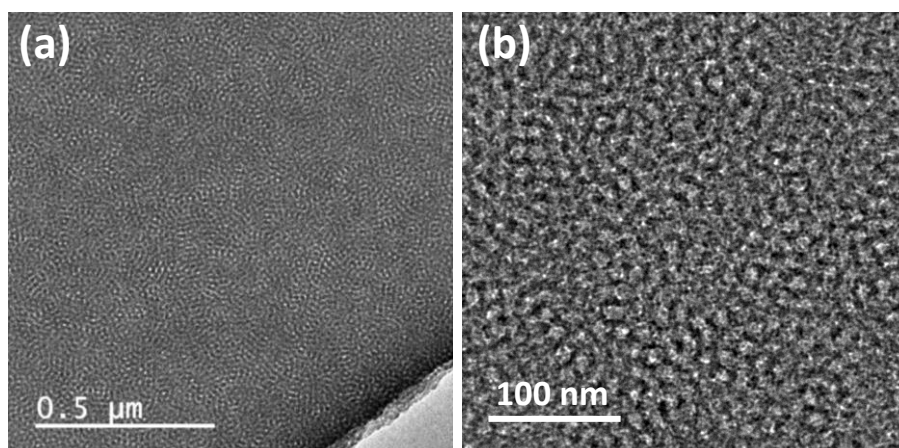


Figure 2. TEM images of the mesoporous silica films lifted off the ITO substrates (a) at low magnification and (b) at high magnification.

The as-synthesized mesoporous silica films did not show any voltammetric response for the electroactive probe, $[\text{Ru}(\text{NH}_3)_6]^{3+}$, indicating their crack-free nature (Figure 3a). The thickness of the calcined films was found to be 130 nm using optical profilometry (Figure 3b). The walls of the nanopores were covalently functionalized with viologen moieties through an iodopropylsilane method (Figure 4) standardized for the functionalization of SBA-15 nanopores.^[13] The TEM images of the viologen modified mesoporous silica films (MF-V) show retention of mesoporous structure (Figure 5a-b). IR spectroscopy and digestive analysis of the films confirmed the presence of viologen (Figures 6a-b). Diffuse reflectance infra-red fourier

transform (DRIFT) spectrum of MF-V film showing a peak at 1638 cm^{-1} characteristic of pyridinium ring $\text{—C=N}^+\text{—}$ stretching vibration and also sp^3 (2860 cm^{-1} , 2925 cm^{-1}) and sp^2 C-H (3050 cm^{-1} , 3130 cm^{-1}) stretching vibration (Figure 6a). The UV-visible spectrum of the fluoride digested MF-V film showed a peak for aromatic $\pi\text{—}\pi^*$ transition in the pyridinium rings associated with viologen^[16] at 265 nm whereas the unfunctionalized mesoporous silica film (MF) doesn't show any signature in the UV-visible spectrum (Figure 6b).

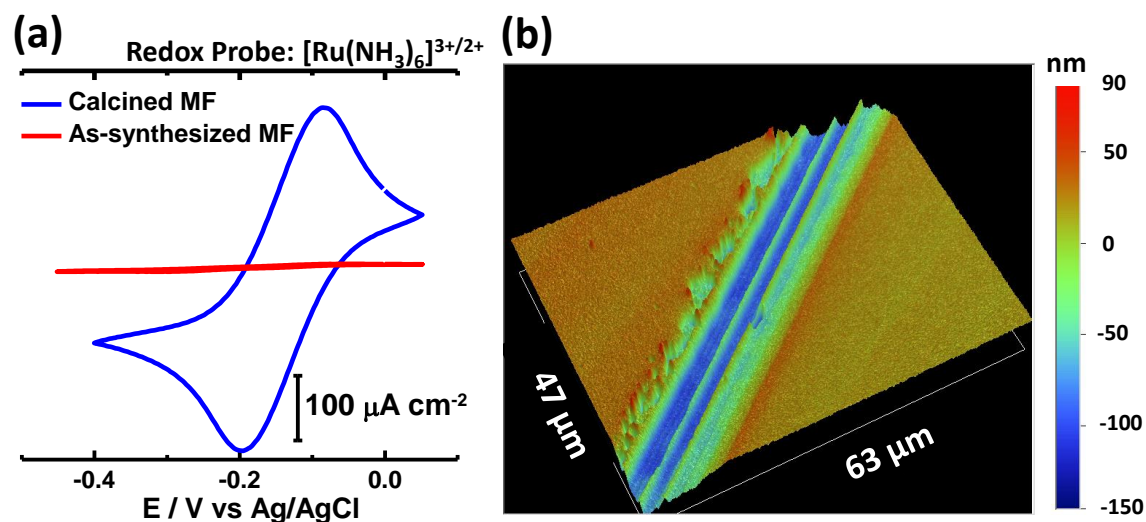


Figure 3. (a) Cyclic voltammograms of the mesoporous silica film before and after calcination in the presence of $1\text{ mM } [\text{Ru}(\text{NH}_3)_6]^{3+}$ showing no ion transport for the uncalcined film implying crack free films. (b) Optical profilometry image of mesoporous silica film with an incision made using a needle to show the film thickness which is around 130 nm . The rest of the film is very uniform in thickness with a roughness of a few nanometers.

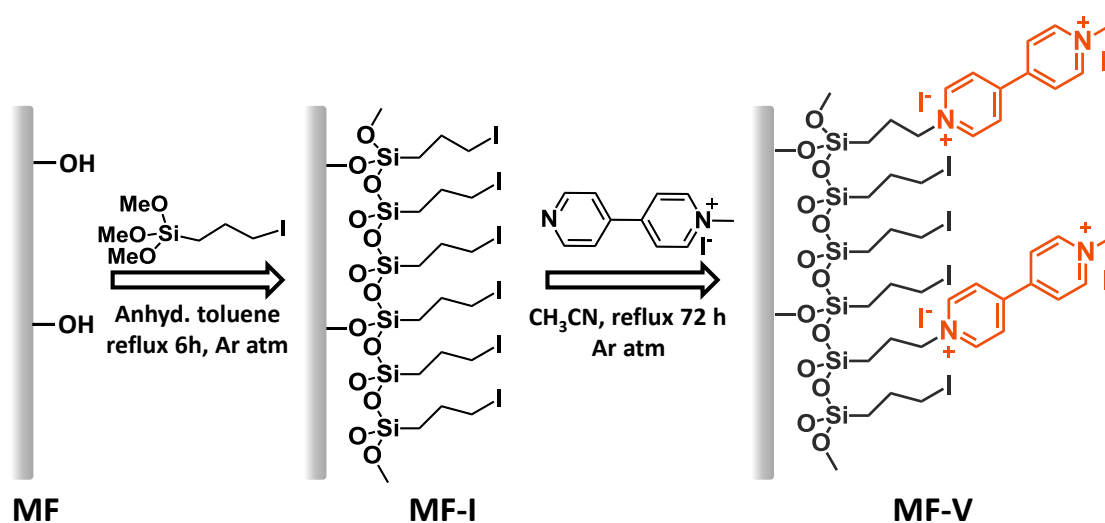


Figure 4. Schematic showing the synthetic strategy followed for preparing MF-V.

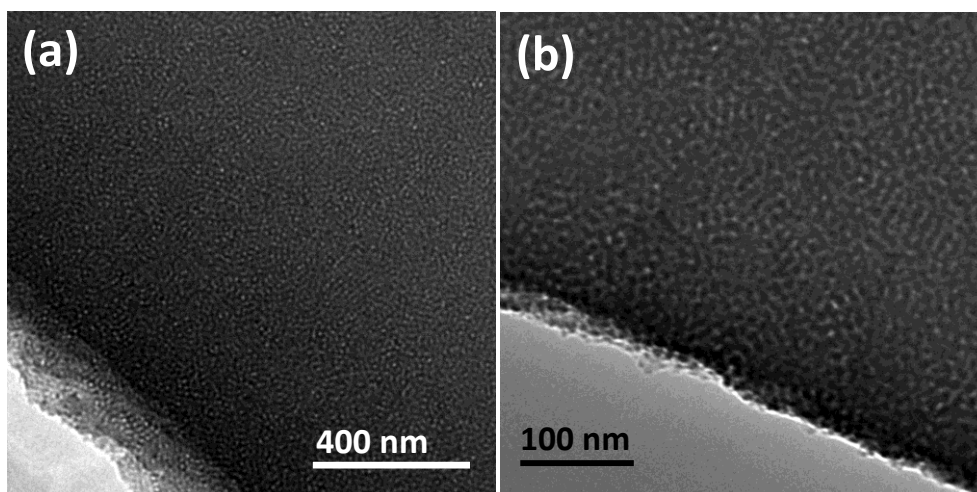


Figure 5. TEM images of the MF-V films lifted off the ITO substrates (a) at low magnification and (b) at high magnification showing retention of its mesoporous structure on functionalization.

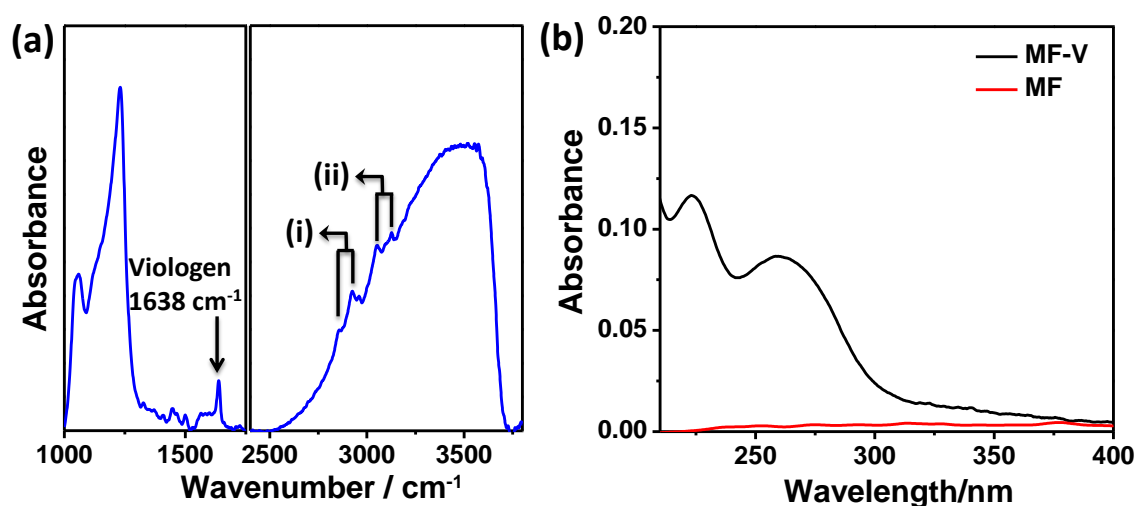


Figure 6. (a) Diffuse reflectance infra-red fourier transform (DRIFT) spectrum of MF-V film showing a peak at 1638 cm^{-1} characteristic of viologen and also (i) sp^3 (2860 cm^{-1} , 2925 cm^{-1}) and (ii) sp^2 C-H (3050 cm^{-1} , 3130 cm^{-1}) stretches. (b) UV-visible spectrum of the flouride digested MF-V film showing peak for aromatic π - π^* transition in the pyridinium rings associated with viologen^[16] at 265 nm whereas the unfunctionalized mesoporous silica film (MF) doesn't show any signature in the UV-visible spectrum.

The transport across the nanopores of MF-V supported on ITO substrate was investigated separately with 1 mM solutions of $[\text{Fe}(\text{CN})_6]^{3-}$ and $[\text{Ru}(\text{NH}_3)_6]^{3+}$ as anionic and cationic electroactive probes respectively, using cyclic voltammetry. Electrochemical measurements were carried out in the potential window of -0.40 V to $+0.45\text{ V}$, where there are no interferences from the electroactive acceptor, viologen and the donor, pyranine (Figure 7).

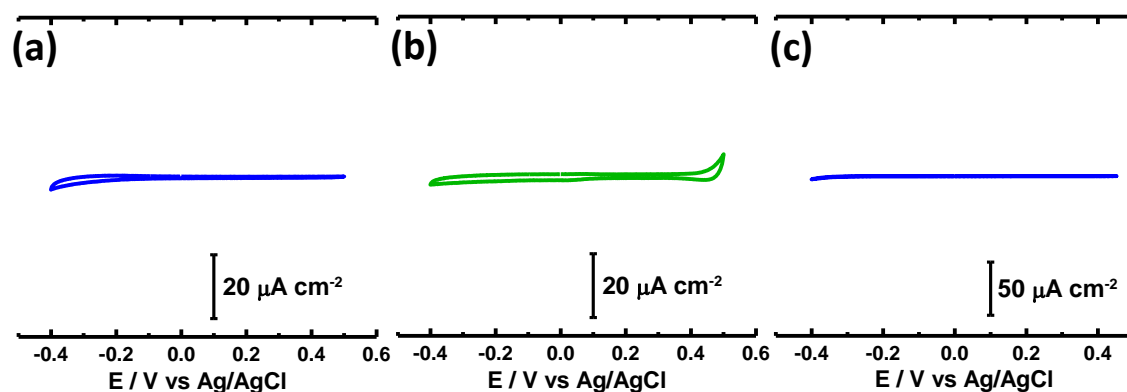


Figure 7. Cyclic voltammograms of (a) 5×10^{-4} M coronene tetracarboxylate (CS) and (b) 5×10^{-4} M pyranine (P) showing no interference in the scan range used for transport measurements. (c) Cyclic voltammogram of viologen modified film in the absence of redox probes showing no interference in the measurement window of -0.40 V to +0.45 V. Scan rate: 200 mV/s. Supporting electrolyte: 0.1 M KCl.

Figure 8a shows the cyclic voltammograms for the transport of $[\text{Fe}(\text{CN})_6]^{3-}$ and $[\text{Ru}(\text{NH}_3)_6]^{3+}$ through MF-V at pH 6 with 0.1 M KCl as supporting electrolyte. The positively charged pores of the MF-V elicits a strong and highly selective electrochemical response (cathodic current density $185 \mu\text{A}/\text{cm}^2$) for the transport of anionic, $[\text{Fe}(\text{CN})_6]^{3-}$ probe (blue trace), and no response to the cationic, $[\text{Ru}(\text{NH}_3)_6]^{3+}$ (red trace), owing to the unipolar environment inside the nanopores (Figure 8b) of radius in the order of Debye length range. To reverse the surface charge within the pores, non-covalent interactions between the positively charged viologen (each unit carries two positive charges) and negatively charged pyranine (each unit has three negative charges at pH 6) was used by soaking the MF-V film in 1 mM solution of pyranine. MF-V soaked in pyranine solution for 16 h, shows a strong electrochemical response to cationic probe, $[\text{Ru}(\text{NH}_3)_6]^{3+}$ and no response for anionic $[\text{Fe}(\text{CN})_6]^{3-}$ in the cyclic voltammogram, a complete reversal of ionic transport from anion selective to cation selective indicating charge-reversal inside the nanopores (Figure 8c,d).

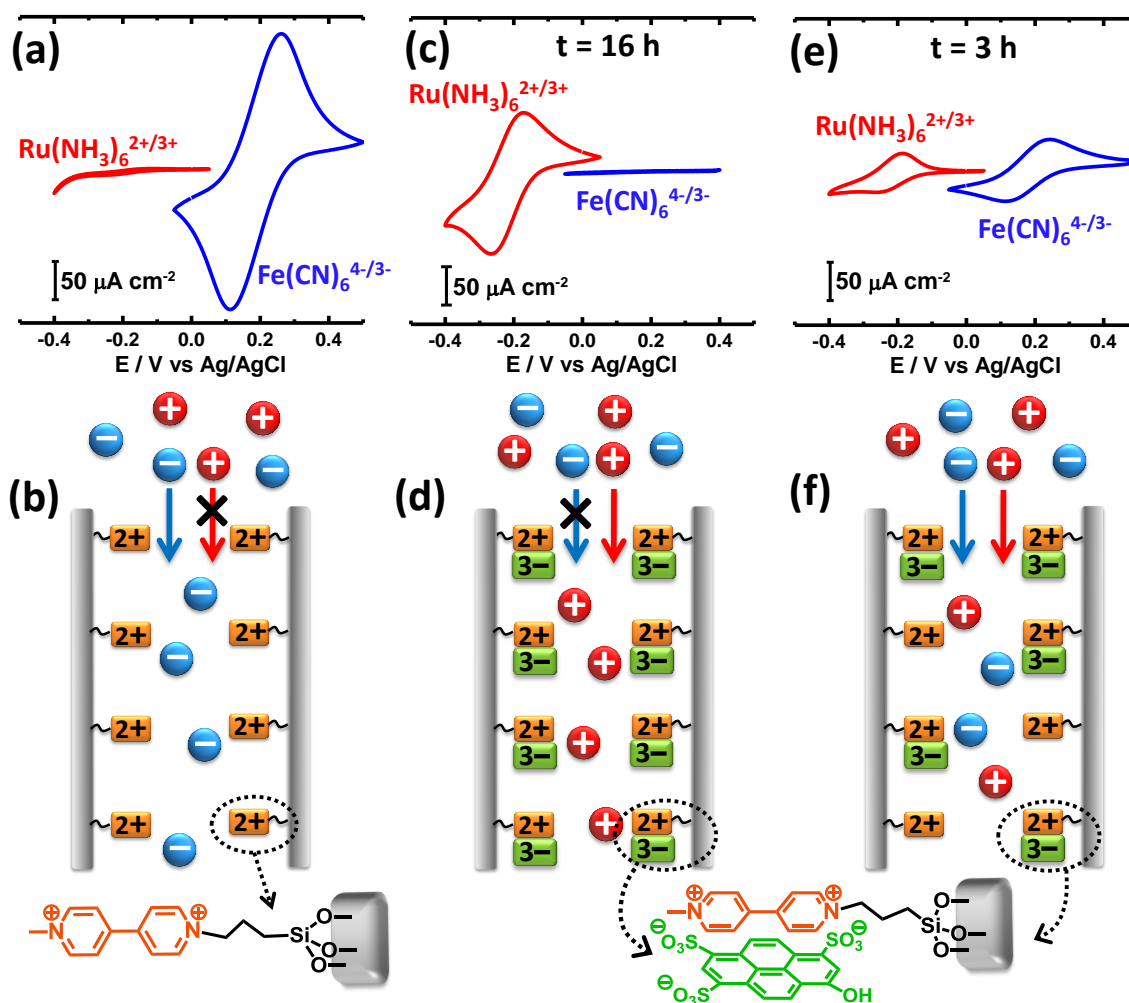


Figure 8. Cyclic voltammograms corresponding to viologen modified mesoporous silica film (MF-V) deposited on ITO electrode in the presence of 1 mM $[\text{Ru}(\text{NH}_3)_6]^{3+}$ (red trace) and 1 mM $[\text{Fe}(\text{CN})_6]^{3-}$ (blue trace) before soaking in 1 mM pyranine solution (a), after soaking in 1 mM solution of pyranine for 16h (c) and 3 h (e). Scan Rate: 200 mV/s. Supporting electrolyte: 0.1 M KCl (pH 6). The corresponding schematics depicting the surface charge of the pores and the nature of transport are given as (b), (d) and (f) respectively.

Furthermore, the peak current density for $[\text{Ru}(\text{NH}_3)_6]^{3+}$ transport (cathodic current density $96 \mu\text{A/cm}^2$) is half that of the peak current density observed for $[\text{Fe}(\text{CN})_6]^{3-}$ transport (cathodic current density $185 \mu\text{A/cm}^2$) in MF-V. This can possibly be understood by considering the fact that the transport in nanochannels is governed by the surface charge.³ On soaking MF-V in pyranine (16 h), the surface charge inside the nanopores is halved as the di-positive viologen moieties become mono-negative C-T pairs and hence lead to a decrease in ion transport. It is to be noted that charge-reversal in 1:1 binding would be possible only when, the donor has more number of negative charges than the number of positive charges available with the acceptor. If the charges on both donor and acceptor are equal, 1:1 binding will only lead to

charge neutralization. In our case, the di-positive acceptor, viologen and tri-negative donor, pyranine would lead to neutralization when two-thirds of the viologen are bound to pyranine. The observation of charge reversal on soaking MF-V in pyranine for 16 h suggests that most of the viologen are bound to pyranine. Moreover, the extent of viologen moieties binding to pyranine inside the nanopores can be controlled by the time of soaking since the binding of pyranine to viologen is diffusion controlled. SBA-16 films used here have a three dimensional pore network containing pores of diameter 10-11 nm and pore necks of size around 6 nm.^[10a] Functionalization with viologen moieties (MF-V) further reduces the pore neck size and hence restricts the diffusion of pyranine. This is in contrast to the fast diffusion observed over viologen functionalized SBA-15 with relatively large pore size (8 nm).^[13] The slow diffusion over MF-V was in turn used to control the surface charge within the pores from positive to neutral (or negative) depending upon the degree of binding of pyranine with time. When the soaking time of MF-V in pyranine solution was reduced to 3 h, the resulting film shows ambipolar transport by allowing both anionic and cationic probes to comparable extent^[17] (Figure 8e,f). This suggests that the surface charge of the nanopores is close to neutrality, implying that roughly two-thirds of the viologen are bound to pyranine. So, it can be understood that the diffusion of pyranine molecules into the pores initially neutralises the pore surface charge and then further binding increases the negative charge on the pore wall which decreases the entry of pyranine molecules due to electrostatic repulsion. This slows down the reversal of charge inside the nanopores and hence the neutralisation step takes only 3 h to complete.

To discern the role of C-T interactions in achieving charge reversal, an ionic blank was made by functionalizing the pores of mesoporous silica films with dicationic ammonium salt of 1,4-diazabicyclo[2.2.2]octane (MF-B, Figure 9). The dicationic moieties of MF-B cannot form C-T complexes with pyranine and hence will serve as a blank for electrostatic interactions. The electrochemical response of the ionic blank, MF-B, mimics that of MF-V by selectively transporting anions, $[\text{Fe}(\text{CN})_6]^{3-}$ (Figure 10a-b). Unlike MF-V film, soaking of MF-B film in pyranine solution for 16 h did not reverse the transport behaviour (Figure 10c-d). The weak electrostatic binding of pyranine to the positively charged walls of MF-B reduces the overall positive charge allowing small amount of $[\text{Ru}(\text{NH}_3)_6]^{3+}$ ions to pass through, giving a very weak signal. This clearly supports the role of strong supramolecular C-T motifs in reversing the surface charge and polarity of ion transport in a confined environment.

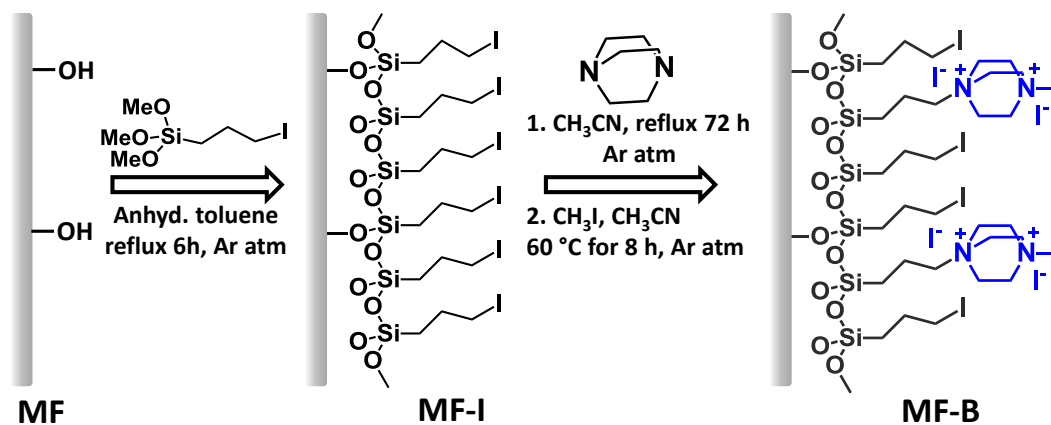


Figure 9. Schematic showing the synthetic strategy followed for preparing MF-B. Note: The dipositive ammonium salt of DABCO could also be attached to the pore wall through both nitrogens and not necessarily as shown.

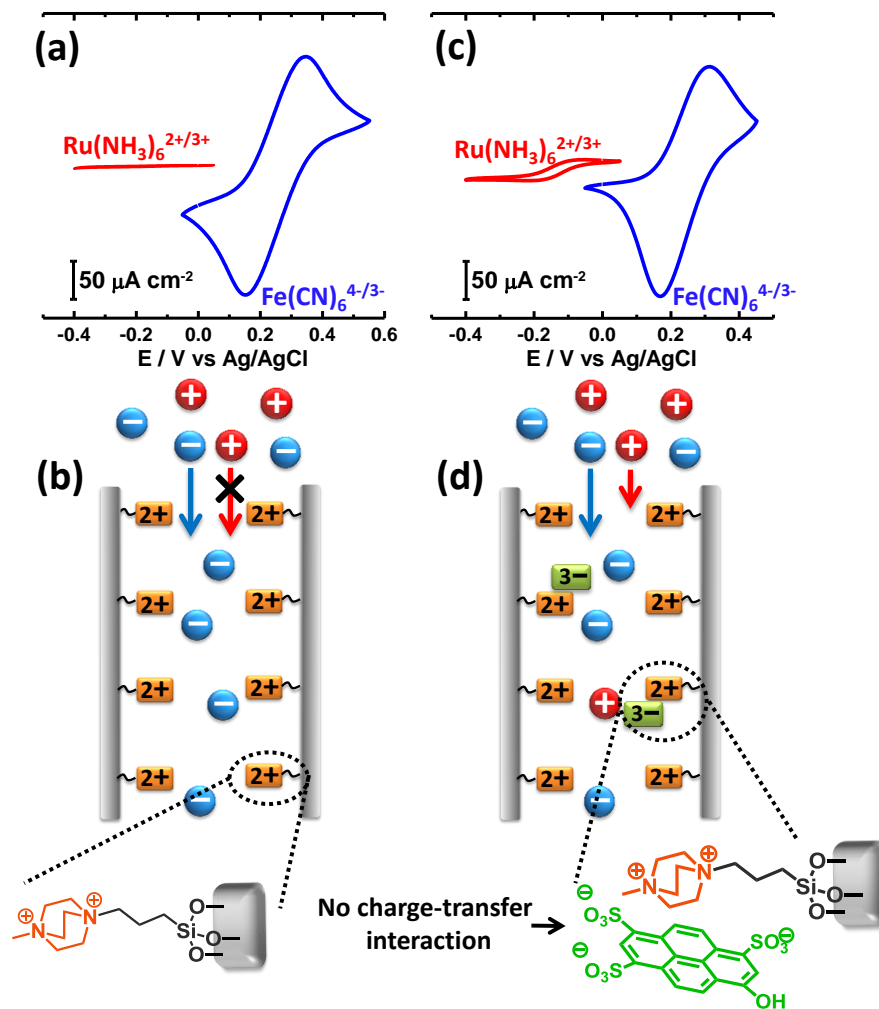


Figure 10. Cyclic voltammograms corresponding to mesoporous silica film modified with dipositive ammonium salt of 1,4-diazabicyclo[2.2.2]octane (MF-B) supported on ITO electrode in the presence of 1 mM $[Ru(NH_3)_6]^{3+}$ (red trace) and 1 mM $[Fe(CN)_6]^{3-}$ (blue trace), before (a)

and after 16 h (c) exposure to 1 mM pyranine solution. Scan Rate: 200 mV/s. Supporting Electrolyte: 0.1 M KCl (pH 6). Schematic illustration of ion transport through the MF-B film before (b) and after soaking it for 16 h (d) in 1 mM pyranine solution.

Viologen being a very strong acceptor is capable of binding to a variety of charged donors (for example coronene tetracarboxylate, eosin, perylene tetracarboxylate, etc.) which allows flexibility to use a variety of donors to modify the surface charge on the pore wall. This modular nature of these C-T based supramolecular motifs gives ample flexibility to manipulate the surface charge as they can be functionalized with various moieties which could respond to external stimuli like pH, light, and temperature. For example, donor components having several carboxylic acid groups (with different pK_a values) in the same molecule would offer pH responsive surface charge regulation within the confined nanopores. To modulate ion transport in response to pH, we have selected coronene tetracarboxylate (CS) as the donor. It has four carboxylate groups whose protonation/deprotonation can be modulated with pH. A pH titration of CS was carried out in order to determine the pK_a 's of the four carboxyl groups (Figure 11). The pH titration shows three distinct regions of slope change (marked as A, B and C) indicating three different pK_a 's. Each of the regions, A and B, extend for around 0.08 mL of 0.1 M HCl indicating protonation of one equivalent of $-\text{COOH}$ groups. The region C spans twice the volume of region A or B, indicating protonation of two equivalents of carboxylate groups. This implies that these two carboxyl groups have very similar pK_a of around 4.5. So the pK_a 's of the four $-\text{COOH}$ groups are: $pK_{a4} \sim 9.5$ (region A); $pK_{a3} \sim 5.5 - 6.0$ (region B); pK_{a2} and $pK_{a1} \sim 4.5$ (region C)

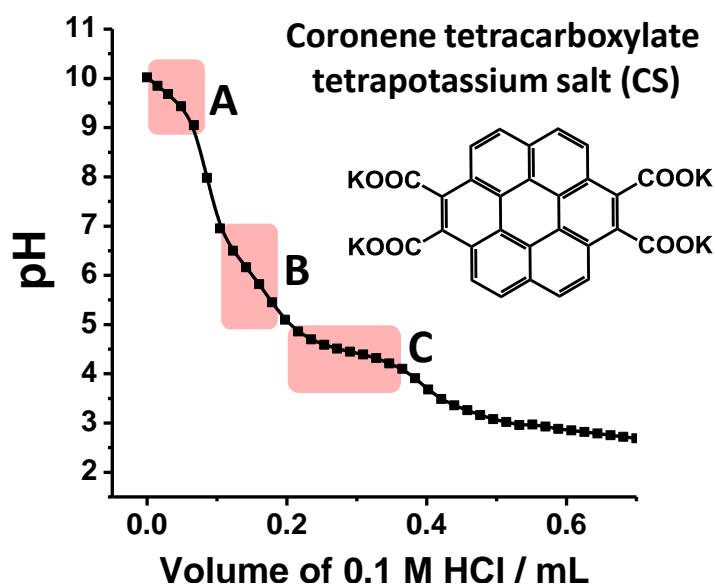


Figure 11. pH titration of coronene tetracarboxylate tetrapotassium salt showing three different pK_a 's.

It should be noted that this is a solution state titration and hence does not directly reflect their pK_a when bound to viologen on MF-V film. It is also known that the pK_a of surface adsorbed and confined molecules can differ by 2-3 units from their solution state analogues.^[18] The MF-V films were soaked in coronene tetracarboxylate solution (1 mM, pH 6) to non-covalently functionalize the pore walls with CS through C-T binding to the viologen. The ion transport through the nanopores of CS bound MF-V film was investigated at different pH (9, 6 and 3) to understand its pH-responsive transport.

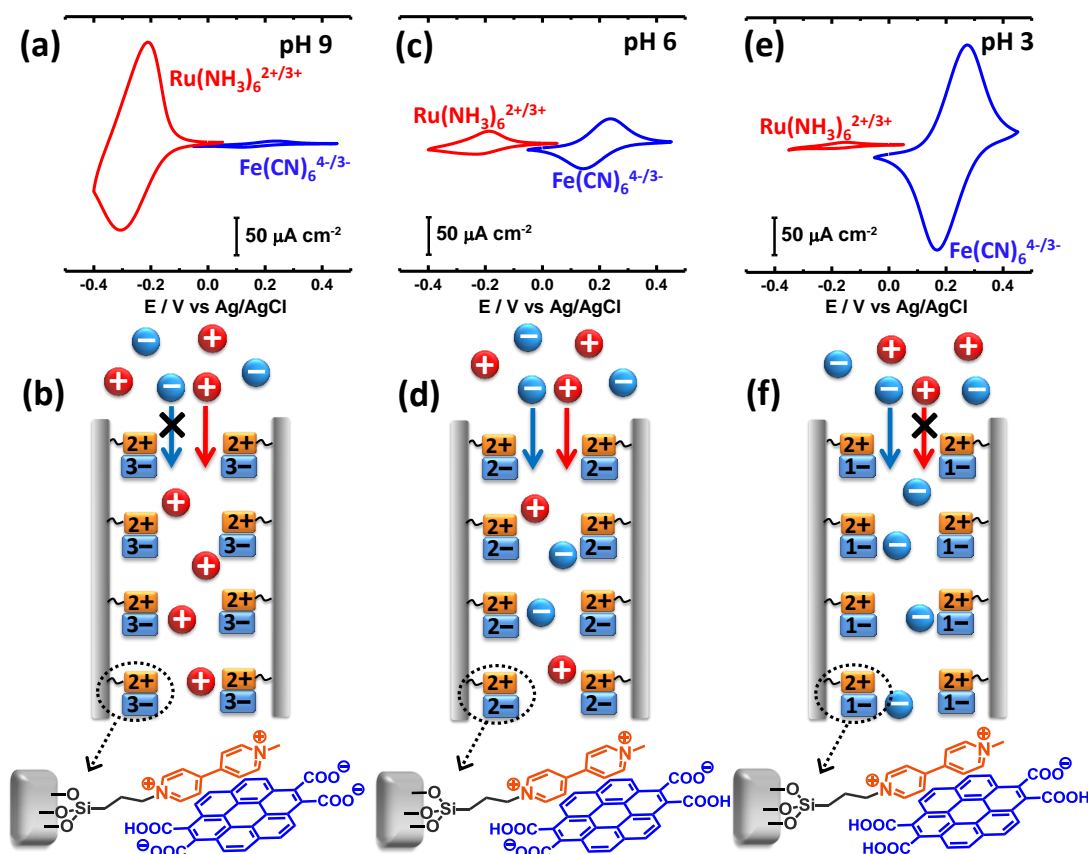


Figure 12. Cyclic voltammograms corresponding to coronene tetracarboxylate bound MF-V deposited on ITO electrode in the presence of 1 mM $[Ru(NH_3)_6]^{3+}$ (red trace) and 1 mM $[Fe(CN)_6]^{3-}$ (blue trace) at different pH conditions: (a) 9, (c) 6 and (e) 3. Scan Rate: 200 mV/s. Supporting Electrolyte: 0.1 M KCl. The corresponding schematics are given as (b), (d) and (f).

The voltammogram recorded at pH 9 shows a very high transport for positively charged $[Ru(NH_3)_6]^{3+}$ probe and a suppression for $[Fe(CN)_6]^{3-}$ transport, implying negatively charged pore walls (Figure 12a). This is understandable as most of the carboxylate groups of CS are not protonated at pH 9 (Figure 12b), thereby flipping the charge on the pore walls from positive (MF-V) to negative. At pH 6, both positive and negative probes give similar voltammetric response indicating ambipolar transport (Figure 12c) This suggests that at pH 6, probably two of the four carboxylate groups in the donor molecules are protonated, thereby

effectively neutralizing the dipositive viologen moieties inside the pores (Figure 12d). In contrast to the behaviour at pH 9, the transport at pH 3 shows a strong preference to negatively charged $[\text{Fe}(\text{CN})_6]^{3-}$, similar to that of MF-V, suggesting that most of the carboxylate groups in the donor are in the protonated form (Figures 12e-f). On changing the pH from 9 to 3, the electrochemical current density for $[\text{Ru}(\text{NH}_3)_6]^{3+}$ decreases from $101 \mu\text{A}/\text{cm}^2$ to $3 \mu\text{A}/\text{cm}^2$ while, for $[\text{Fe}(\text{CN})_6]^{3-}$ it increases from $3 \mu\text{A}/\text{cm}^2$ to $126 \mu\text{A}/\text{cm}^2$ (Figure 13a). The ratio of electrochemical currents for negative and positive redox probes, $I_{\text{Fe}}/I_{\text{Ru}}$, which is 0.03 at pH 9 increases to 60 at pH 3, a change more than three orders in magnitude (Figure 13b).

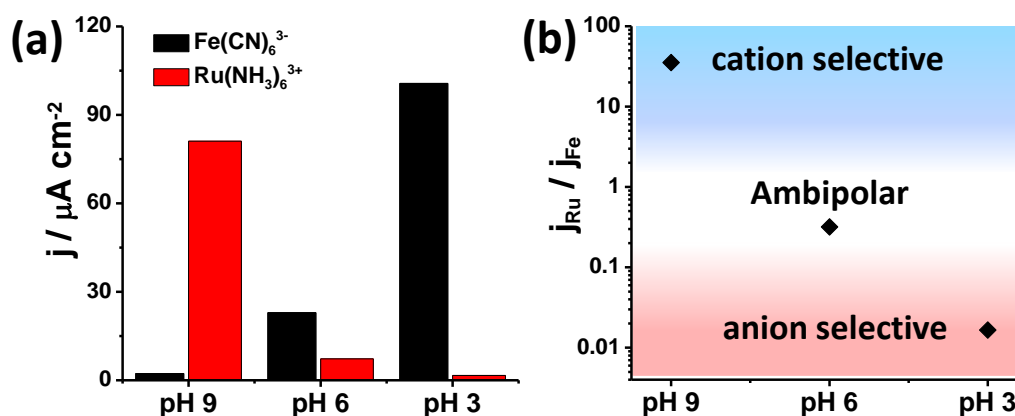


Figure 13. (a) The variation of peak current densities of $[\text{Fe}(\text{CN})_6]^{3-}$ and $[\text{Ru}(\text{NH}_3)_6]^{3+}$ for CS bound MF-V showing switching of ion transport properties with change in pH from 9 to 3. (b) The ratio of anion to cation current density showing three orders of change with pH. The regimes of different types of ion transport, viz. anion selective, cation selective and ambipolar, are shown in different colors.

The variation of surface charge with respect to pH by silanol groups^[19] is ruled out in our case as the pore surfaces were modified through a surface polymerization approach,^[20] which completely coats the surface with a monolayer of silane leaving no free silanol groups. Moreover, separate ion-transport experiments on MF-V with respect to pH did not show any variation in the asymmetry of transport (Figures 14a and 15) clearly supporting that the origin of pH- responsive ion transport is from the carboxyl functional groups associated with the donor. Thus, by selecting a donor with pH responsive functional groups we were able to switch the transport between cation selective, anion selective and ambipolar by changing the pH (Figure 14b). To demonstrate the switching ability of the system with pH we monitored the voltammograms through three cycles of pH which showed good reversibility (Figure 14b).

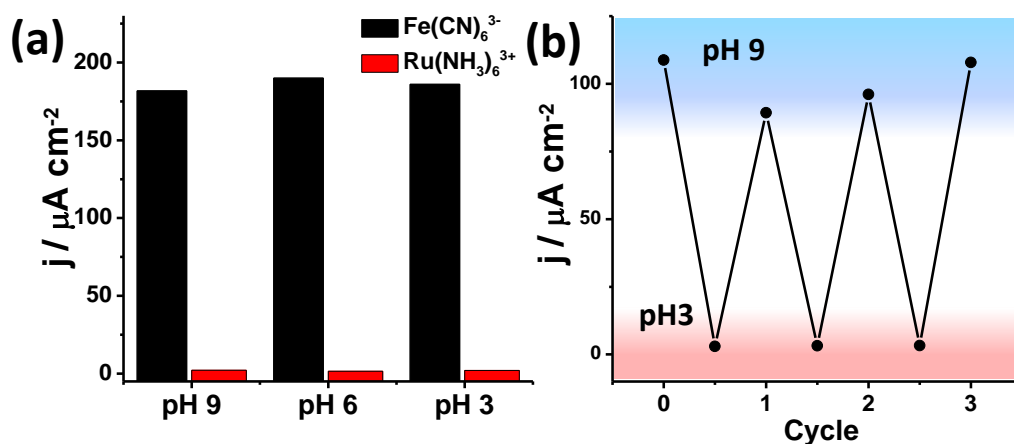


Figure 14. (a) The peak current densities of $[Fe(CN)_6]^{3-}$ and $[Ru(NH_3)_6]^{3+}$ for MF-V show no significant change with variation in pH indicating absence of free silanol groups. (b) The switching of peak current density of $[Ru(NH_3)_6]^{3+}$ on exposure to three cycles of pH change showing good reversibility.

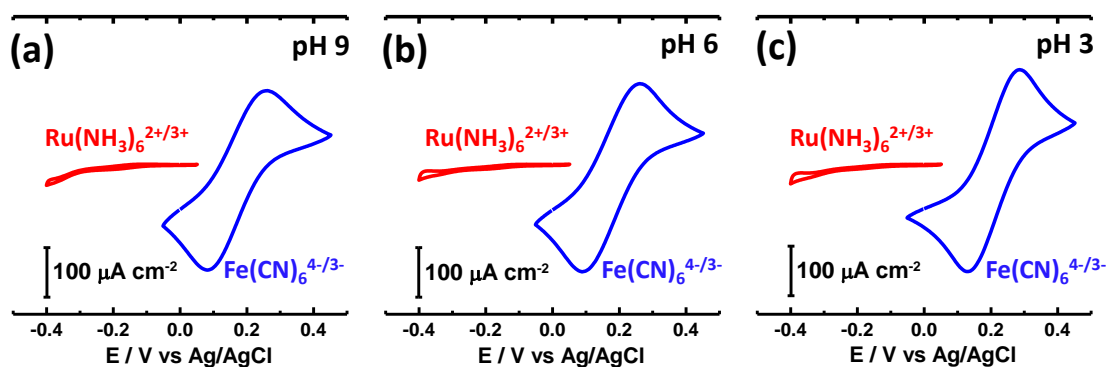


Figure 15. Cyclic voltammograms of viologen modified mesoporous silica film in the presence of 1 mM $[Ru(NH_3)_6]^{3+}$ (red trace) and 1 mM $[Fe(CN)_6]^{3-}$ (blue trace) respectively, at different pH environments: (a) 9, (b) 6 and (c) 3.

4.1.6. Conclusions

In conclusion, we have demonstrated a facile non-covalent approach to attain charge-reversal within the nanopores (< 10 nm) using supramolecular C-T motifs. This non-covalent approach gives a lot of manoeuvrability to control the surface charge within the confined pores which in turn was exploited to achieve various forms of ion transport, like cation selective, anion selective and ambipolar with respect to extent of donor binding. Furthermore, the functional utility of donors for pH responsive ion transport has also been demonstrated. This in principle opens up the possibility of selecting large variety of donor modules attached with various functional groups which could respond to multiple stimuli such as light, pH, and

temperature and redox system and hence modulate transport of ions as well as the molecules across the nanochannel.

4.1.7. References

- [1] B. Hille, *Ion Channels of Excitable Membranes, 3rd Edition*, Sinauer, **2001**.
- [2] a) W. Sparreboom, A. van den Berg, J. C. T. Eijkel, *Nat. Nanotechnol.* **2009**, *4*, 713-720; b) C. Dekker, *Nat. Nanotechnol.* **2007**, *2*, 209-215; c) X. Hou, L. Jiang, *ACS Nano* **2009**, *3*, 3339-3342; d) S. Howorka, Z. Siwy, *Chem. Soc. Rev.* **2009**, *38*, 2360-2384; e) Z. S. Siwy, *Adv. Funct. Mater.* **2006**, *16*, 735-746; f) H. Daiguji, *Chem. Soc. Rev.* **2010**, *39*, 901-911.
- [3] D. Stein, M. Kruithof, C. Dekker, *Phys. Rev. Lett.* **2004**, *93*, 035901.
- [4] Q. Pu, J. Yun, H. Temkin, S. Liu, *Nano Lett.* **2004**, *4*, 1099-1103.
- [5] R. Karnik, C. Duan, K. Castelino, H. Daiguji, A. Majumdar, *Nano Lett.* **2007**, *7*, 547-551.
- [6] B. Yameen, M. Ali, R. Neumann, W. Ensinger, W. Knoll, O. Azzaroni, *Nano Lett.* **2009**, *9*, 2788-2793.
- [7] L. Wen, Q. Liu, J. Ma, Y. Tian, C. Li, Z. Bo, L. Jiang, *Adv. Mater.* **2012**, *24*, 6193-6198.
- [8] a) M. Ali, P. Ramirez, S. Mafé, R. Neumann, W. Ensinger, *ACS Nano* **2009**, *3*, 603-608; b) B. Yameen, M. Ali, R. Neumann, W. Ensinger, W. Knoll, O. Azzaroni, *J. Am. Chem. Soc.* **2009**, *131*, 2070-2071.
- [9] a) G. Wang, A. K. Bohaty, I. Zharov, H. S. White, *J. Am. Chem. Soc.* **2006**, *128*, 13553-13558; b) M. Zhang, X. Hou, J. Wang, Y. Tian, X. Fan, J. Zhai, L. Jiang, *Adv. Mater.* **2012**, *24*, 2424-2428.
- [10] a) A. Brunsen, A. Calvo, F. J. Williams, G. J. A. A. Soler-Illia, O. Azzaroni, *Langmuir* **2011**, *27*, 4328-4333; b) E. N. Savariar, M. M. Sochat, A. Klaikherd, S. Thayumanavan, *Angew. Chem. Int. Ed.* **2009**, *48*, 110-114; c) O. Azzaroni, B. Trappmann, P. van Rijn, F. Zhou, B. Kong, W. T. S. Huck, *Angew. Chem. Int. Ed.* **2006**, *45*, 7440-7443.
- [11] a) R. Scott Lokey, B. L. Iverson, *Nature* **1995**, *375*, 303-305; b) Z. Huang, L. Yang, Y. Liu, Z. Wang, O. A. Scherman, X. Zhang, *Angew. Chem. Int. Ed.* **2014**, doi: 10.1002/anie.201402817; c) T. Aida, E. W. Meijer, S. I. Stupp, *Science* **2012**, *335*, 813-817; d) A. Brunsen, C. Díaz, L. I. Pietrasanta, B. Yameen, M. Ceolín, G. J. A. A. Soler-Illia, O. Azzaroni, *Langmuir* **2012**, *28*, 3583-3592.
- [12] a) K. Liu, C. Wang, Z. Li, X. Zhang, *Angew. Chem. Int. Ed.* **2011**, *50*, 4952-4956; b) C. Wang, S. Yin, S. Chen, H. Xu, Z. Wang, X. Zhang, *Angew. Chem. Int. Ed.* **2008**, *47*, 9049-9052; c) K. V. Rao, K. Jayaramulu, T. K. Maji, S. J. George, *Angew. Chem. Int.*

- Ed.* **2010**, *49*, 4218-4222; d) F. Tian, D. Jiao, F. Biedermann, O. A. Scherman, *Nat. Commun.* **2012**, *3*, 1207; e) N. Yanai, K. Kitayama, Y. Hijikata, H. Sato, R. Matsuda, Y. Kubota, M. Takata, M. Mizuno, T. Uemura, S. Kitagawa, *Nat. Mater.* **2011**, *10*, 787-793; f) S. Shimomura, R. Matsuda, T. Tsujino, T. Kawamura, S. Kitagawa, *J. Am. Chem. Soc.* **2006**, *128*, 16416-16417; g) A. Okabe, T. Fukushima, K. Ariga, T. Aida, *Angew. Chem. Int. Ed.* **2002**, *41*, 3414-3417.
- [13] B. V. V. S. P. Kumar, K. V. Rao, T. Soumya, S. J. George, M. Eswaramoorthy, *J. Am. Chem. Soc.* **2013**, *135*, 10902-10905.
- [14] D. Zhao, P. Yang, N. Melosh, J. Feng, B. F. Chmelka, G. D. Stucky, *Adv. Mater.* **1998**, *10*, 1380-1385.
- [15] A. Walcarius, *Chem. Soc. Rev.* **2013**, *42*, 4098-4140.
- [16] R. Martín, P. C. Heydorn, M. Alvaro, H. Garcia, *Chem. Mater.* **2009**, *21*, 4505-4514.
- [17] S. B. Lee, C. R. Martin, *Anal. Chem.* **2001**, *73*, 768-775.
- [18] a) D. A. Walker, E. K. Leitsch, R. J. Nap, I. Szleifer, B. A. Grzybowski, *Nat. Nanotechnol.* **2013**, *8*, 676-681; b) D. Wang, R. J. Nap, I. Lagzi, B. Kowalczyk, S. Han, B. A. Grzybowski, I. Szleifer, *J. Am. Chem. Soc.* **2011**, *133*, 2192-2197.
- [19] A. Calvo, B. Yameen, F. J. Williams, G. J. A. A. Soler-Illia, O. Azzaroni, *J. Am. Chem. Soc.* **2009**, *131*, 10866-10868.
- [20] X. Feng, G. E. Fryxell, L.-Q. Wang, A. Y. Kim, J. Liu, K. M. Kemner, *Science* **1997**, *276*, 923-926.

Chapter-4.2

A Generic Strategy to Improve the Non-covalent Gating of Ion Transport using Auxillary Hydrophobic Interactions

Summary

Realization of charge-reversal in nanochannels through non-covalent motifs requires a generic strategy to improve their strength of association in water based systems. Surfaces modified with weak pyranine-viologen, charge-transfer (C-T) modules were only capable of showing only charge neutralization and not charge reversal. We illustrate a strategy based on hydrophobic forces to improve the performance of weak C-T modules to show complete charge reversal within nanopores. The strong association aided by hydrophobic forces enable the performance of supramolecular assemblies in achieving charge reversal and reduce the dependence on excess donors in solution. The kinetics of assembly was found to be fast with completion of non-covalent functionalization within 30 minutes.

Manuscript based on this work is under preparation.

4.2.1. Introduction

Protein nanochannels in biological systems^[1] are known to modulate the flux as well as the nature of ion transport in and out of the cell. They are also capable of showing selective transport of specific ions based on size. Their elegance in regulating the ion transport inspired many to develop abiotic mimics in recent years to modulate the flux, nature and direction of ion transport. Apart from geometry, the surface charge^[2] plays a pivotal role in controlling the nature of ion transport and is an important parameter to be considered in designing these abiotic analogues. Furthermore, the control of surface charge in nanochannels of size less than 10 nm has biological relevance since the Debye length at physiological salt concentrations is of the order of a few nanometres. Typically, the modulation of surface charge was achieved through covalent linking of organic moieties capable of switching their charge in response to pH^[3] or light.^[4] However, the strong and static nature of covalent functionalization, though a virtue in itself, hampers its post synthetic flexibility and re-configurability to respond to multiple stimuli. On the other hand, non-covalent strategies towards charge reversal in confined environments (<10 nm) largely depend upon the strength of their association. Most often non-covalent motifs have weak association and hence lack the ability to show charge-reversal on binding. Even systems with strong C-T modules^[5] require addition of a small amount of non-covalent motif in solution in order to keep the equilibrium towards the bound state. For example, in our study with strong C-T modules, pyranine and viologen attached to mesoporous silica film (Chapter 4.1), we have used 0.5 mM of the donor in solution while recording cyclic voltammograms to maintain a stable assembly. Any generic strategy to improve the binding constant would reduce this dependence on excess donor in solution and also allow us to utilize the plethora of non-covalent motifs to tune the surface charge.

A simple strategy to enhance the association of non-covalent motifs in water is to make use of hydrophobic forces.^[6] The strength of hydrophobic forces stems from the minimisation of the unfavourable water/hydrophobic interface which disrupts the three dimensional network of hydrogen bonds in water. Self-assembly driven by strong hydrophobic interactions is known in literature for numerous systems. Aida and co-workers reported self-assembled nanostructures held together by hydrophobic and π - π interactions.^[6a, 7] Hydrophobic forces are one of the vital components responsible for the stability of many amphiphilic assemblies. They also form the basis of some of the most robust, non-covalent assemblies used for fabricating filtration membranes^[8] which combine the qualities of sturdiness with adaptivity. In these amphiphilic systems, the association constants in water are of the order 10^8 M^{-1} , and cannot be determined directly. So, in order to address the issues of weak binding and requirement of excess motifs in solution, we use hydrophobic interactions to create very strong supramolecular assemblies capable of showing charge reversal in the absence of excess unbound motifs in solution.

4.2.2. Scope of the present investigation

The present study is aimed at developing a generic strategy to improve the performance of supramolecular assemblies in achieving charge reversal and increase their robustness. We observed that the association of donors with viologen (immobilised on the mesoporous silica) was weaker in presence of negatively charged silanols present on the mesoporous silica wall. The binding of pyranine could not induce complete charge reversal even in the presence of excess pyranine in solution. In absence of excess pyranine, only neutralization of pore wall was observed. To improve the strength of association through hydrophobic forces, a dodecyl chain was appended to the pyranine moiety through an ether linkage. This enabled strong binding between the donor and acceptor to create robust supramolecular assemblies to achieve charge reversal even in the absence of excess donor in solution.

4.2.3. Experimental section

Viologen functionalized mesoporous silica film (MF_{OH}-V)

a) Mesoporous silica film (MF_{OH}). Mesoporous silica films (MF_{OH}) were synthesized using a sol-gel method based on tetraethoxysilane (TEOS) as the oxide precursor in the presence of non-ionic block copolymer, Pluronic F127 as the template. The precursor solution was prepared with the following composition: 1 TEOS: 0.0075 F127: 24 EtOH: 5.2 H₂O: 0.28 HCl. ITO slides were dip coated with precursor solution at a withdrawing speed of 1.5 mm s⁻¹ and at a relative humidity of 40-50%.^[9] The freshly deposited films were placed in a chamber maintained at 50% relative humidity for 1 h. The relative humidity in the chamber for placing the freshly deposited films was maintained using a saturated solution of potassium carbonate which is known to give a relative humidity of 43%. The dip coated slides were subjected to thermal treatment at 60 °C (for 1 h) and then at 130 °C (for 1 h) before calcining them for 2 h at 350 °C.

b) Synthesis of N-Methyl-4,4'-bipyridinium Iodide (MV+).^[10] 4 g of 4,4'-bipyridine was dissolved in 60 mL of dichloromethane (DCM) and a solution of 2.0 mL methyl iodide in 20 mL of DCM was added dropwise to the stirred solution. The mixture was left stirring at room temperature for 12 h. The yellow product was filtered off under suction and purified by recrystallization from methanol.

c) Synthesis of viologen silane/1-(3-Trimethoxysilylpropyl)-1'-methyl-(4,4')-bipyridinium.^[11] To the solution containing 1.2 g of MV+, 2.0 mL of (3-iodopropyl)trimethoxysilane was added and refluxed for 48 h. The solvent was then removed to obtain a red solid which was purified by washing extensively with acetonitrile.

(iv) **Viologen functionalized mesoporous silica films (MF_{OH}-V).** The MF_{OH} films were degassed at 80 °C for 3 h and added to 25 mL of dimethylformamide (DMF) along with 0.3 g (0.5 mmol) of viologen silane and left at 85 °C for 24 h. The MF_{OH}-V films obtained were washed with ethanol and subjected to soxhlet extraction with ethanol for a minimum of 24 h.

MF_{OH}-B (Ionic hybrid control)

MF_{OH} films degassed at 80 °C were added to 25 mL of acetonitrile along with 0.22 g (0.5 mmol) of quaternary ammonium silane and heated at 85 °C for 24 h. Protocol for workup was similar to MF_{OH}-V.

Digestion of MF_{OH}-V

The MF_{OH}-V films were digested in a 4 M solution of NH₄F at 60 °C for 10 minutes and analyzed using UV-visible spectroscopy in a 1 mm quartz cuvette.

TEM Sample Preparation

The mesoporous silica films coated on ITO were soaked in 6 M HCl solution overnight to lift off the films from the ITO. The films were centrifuged and washed with ethanol to remove any excess acid.

Voltammetry measurements.

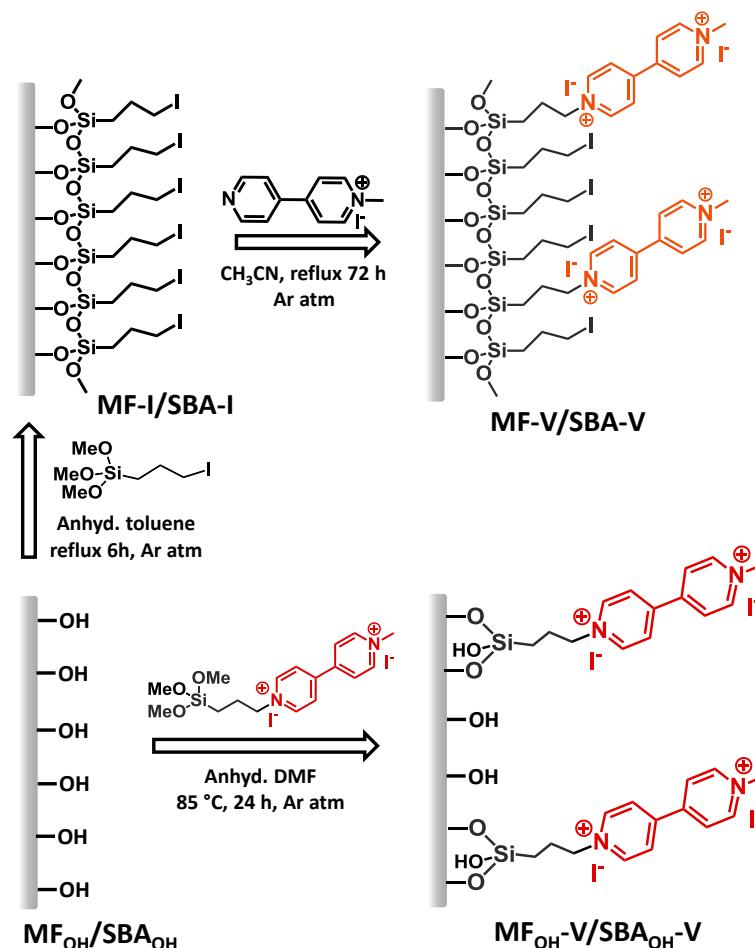
Cyclic voltammetry measurements were performed with ITO slides coated with mesoporous silica films as working electrodes, platinum wire as counter electrode and aqueous Ag/AgCl as reference electrode. MF_{OH}-V films were soaked in 1 mM solution of the donors for 3 h (unless otherwise specified) to allow completion of charge-transfer complex formation prior to the voltammetry measurements. The transport of positively charged [Ru(NH₃)₆]³⁺ and negatively charged [Fe(CN)₆]³⁻ redox probes through the films was monitored using cyclic voltammetry to follow the change in transport properties of the mesoporous silica films. All voltammetric measurements were performed using 1 mM solutions of the redox probe with 0.1 M KCl as the supporting electrolyte at a scan rate of 200 mV/s. The pH was adjusted using acetic acid (0.1 M) and NaOH (0.1 M) for studying the pH responsive properties of the films.

4.2.4. Characterization

Please refer to the appendix for the instrumental details of UV-visible spectroscopy, TEM, FESEM, DRIFTS and voltammetry.

4.2.5. Results and discussion

The nature of functional groups around the viologen on the pore wall determines the binding properties of various donors to viologen. For example, in the presence of polar functional groups the selectivity of binding to coronene tetracarboxylate over perylene tetracarboxylate diminishes. To further understand the influence of iodopropyl groups (hydrophobic environment) on the binding strength, a viologen appended silane was used to directly functionalize mesoporous silica with viologen moieties (SBA_{OH}-V, Scheme 1). The binding studies on SBA_{OH}-V with pyranine revealed a binding constant (Figure 1) seven to eight times smaller than SBA-V (Chapter 2). In order to check if the weakened binding would be sufficient to enable charge-reversal and affect the ion transport properties, mesoporous silica films (SBA-16) functionalized with viologen silane were fabricated.



Scheme 1. Schematic showing the strategy followed for synthesizing SBA-V/MF-V and SBA_{OH}-V/MF_{OH}-V. When the mesoporous silica used was SBA-15, the functionalized silica are

represented as SBA_{OH} , $SBA-I$, $SBA-V$ and SBA_{OH-V} . It is important to note that a significant number of silanols are not passivated on functionalization in the case of SBA_{OH-V}/MF_{OH-V} .

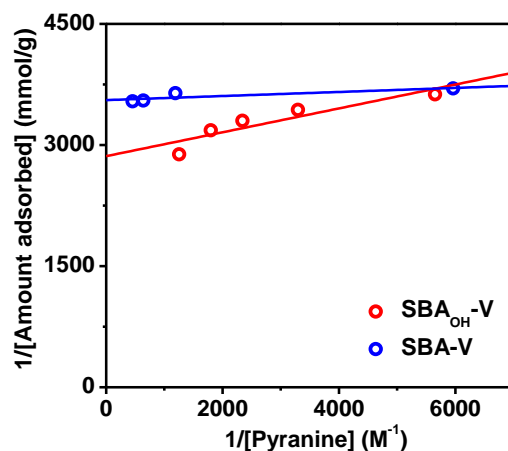


Figure 1. Linear Langmuir plots for the adsorption of pyranine onto $SBA-V$ and SBA_{OH-V} in water at pH 6. The binding constants of $SBA-V$ and SBA_{OH-V} were calculated to be $1.4 \times 10^5 M^{-1}$ and $1.9 \times 10^4 M^{-1}$, respectively. It should be noted that $SBA-V$ does not contain surface silanol and that SBA_{OH-V} has some unpassivated silanols on the pore surface.

Mesoporous silica films supported on ITO substrates were synthesized by dip coating a sol obtained from tetraethylorthosilicate in presence of non-ionic block copolymer template, Pluronic F127. The FESEM images of the calcined films show very uniform crack free films of thickness 180 nm (Figure 2). TEM images show arrays of pores of size range 8-10 nm (Figure 3a-b). The pores were then covalently functionalised with viologen silane (Scheme 1). The incorporation of viologen was confirmed through IR spectroscopy and digestive analysis of the viologen functionalised mesoporous silica films (MF_{OH-V}) (Figure 4). The TEM images of the MF_{OH-V} show retention of the mesoporous structure on functionalization (Figure 3c-d).

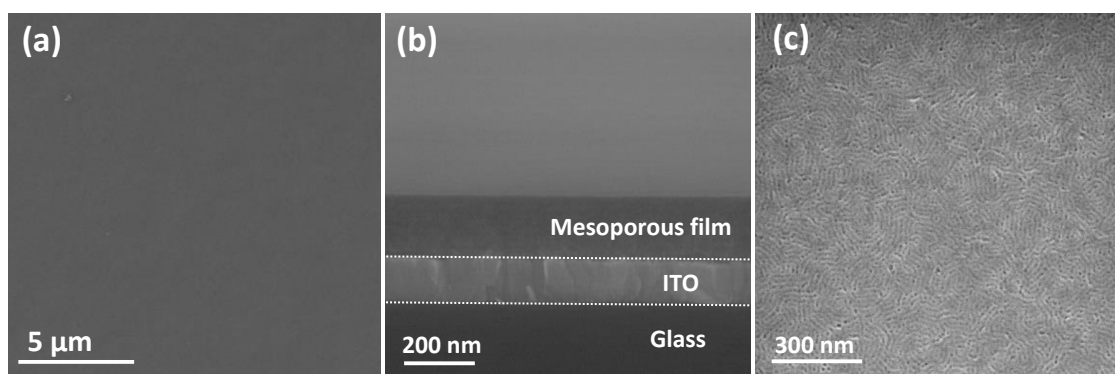


Figure 2. FESEM images (a) at low magnification showing very uniform and crack free mesoporous silica films, (b) showing the thickness of the mesoporous silica film deposited on ITO, and (c) at high magnification showing the porous nature of the film.

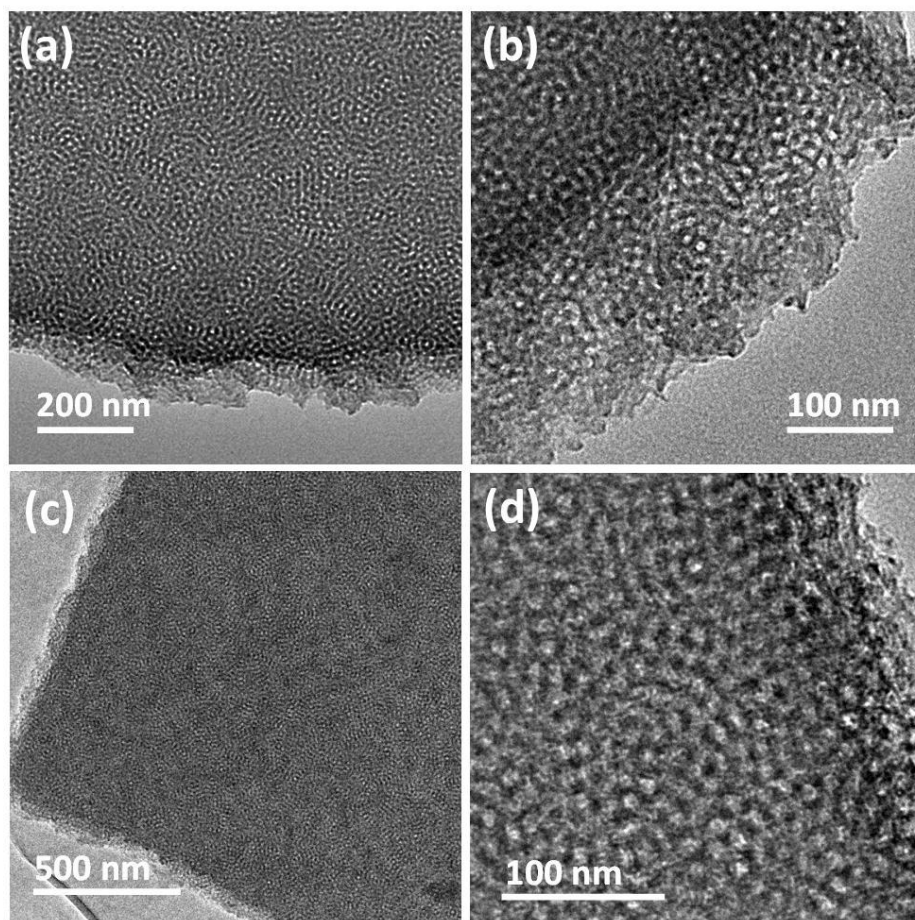


Figure 3. TEM images of mesoporous silica film (a,b) before and (c,d) after viologen functionalization showing retention of pore structure.

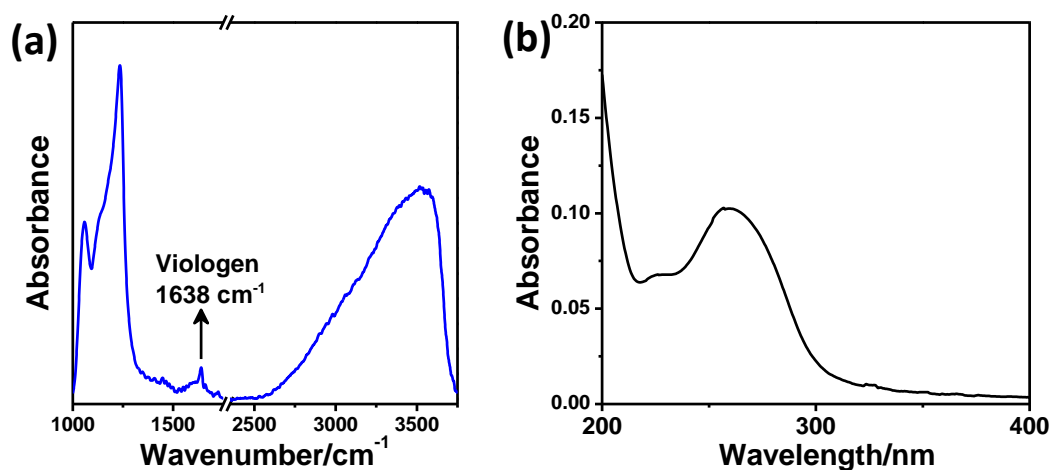


Figure 4. (a) Diffuse reflectance infra-red fourier transform spectrum of MF-V_{OH} showing the characteristic peak for viologen at 1638 cm⁻¹. (b) UV-visible spectrum of the fluoride digested MF-V_{OH} film showing a peak for viologen at 260 nm corresponding to the aromatic π - π^* transition in pyridinium rings.

The permselectivity of the films prepared on ITO was investigated by monitoring the diffusion of positively and negatively charged redox probes, $[\text{Ru}(\text{NH}_3)_6]^{3+}$ and $[\text{Fe}(\text{CN})_6]^{3-}$ respectively, using cyclic voltammetry. To avoid potential interference from the electroactive acceptor (viologen) and donor (pyranine), all measurements were carried out within a potential window of -0.4 V to 0.45 V. Figure 5a and 5c show the cyclic voltammograms recorded on $\text{MF}_{\text{OH-V}}$ film in the presence of 1 mM $[\text{Fe}(\text{CN})_6]^{3-}$ (blue trace) and 1 mM $[\text{Ru}(\text{NH}_3)_6]^{3+}$ (red trace) at pH 3 and pH 6 respectively with 0.1 M KCl as the supporting electrolyte. At both pH 3 and pH 6, the positively charged pores of $\text{MF}_{\text{OH-V}}$ show an anion selective transport. The decrease in the electrochemical response for $[\text{Fe}(\text{CN})_6]^{3-}$ from 230 $\mu\text{A}/\text{cm}^2$ (anodic current density) at pH 3 to 140 $\mu\text{A}/\text{cm}^2$ (anodic current density) at pH 6, indicates decrease in the overall positive charge on the pore walls of $\text{MF}_{\text{OH-V}}$. Since viologen doesn't undergo any change at this pH, it is evident that the ionisation of silanol groups^[12] ($\text{pK}_a \sim 2\text{-}3$) on the pore wall at pH 6 decreases the cumulative positive charge (Scheme 1). The anion selective transport at pH 6 further indicates that the number density of the silanol groups undergoing ionization at pH 6 is much less than the viologen functionalization density as shown in the schematic (Figure 5b and 5d).

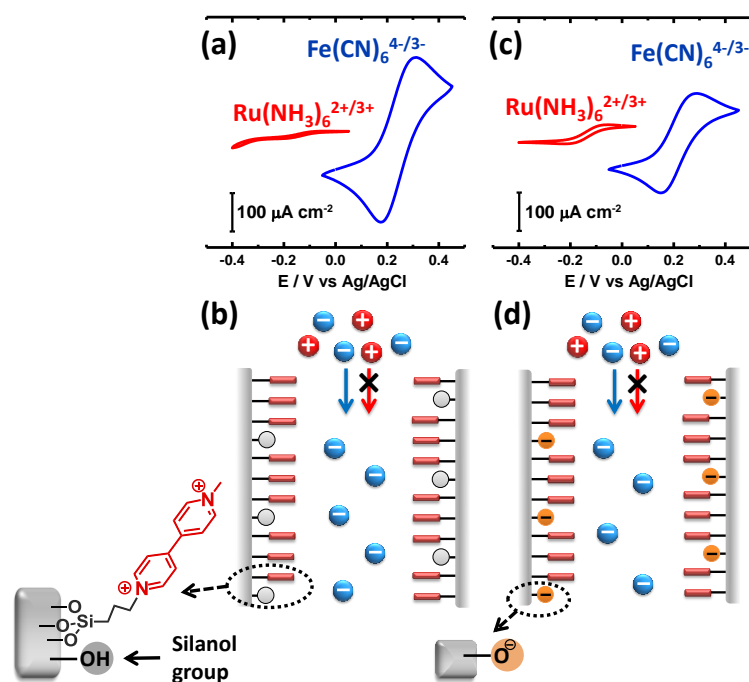


Figure 5. Cyclic voltammograms were recorded in the presence of 1 mM $[\text{Ru}(\text{NH}_3)_6]^{3+}$ (red trace) and 1 mM $[\text{Fe}(\text{CN})_6]^{3-}$ (blue trace) on $\text{MF}_{\text{OH-V}}$ films at (a) pH 3 and (c) pH 6. Scan Rate: 200 mV/s. Supporting electrolyte: 0.1 M KCl. Schematics qualitatively depicting the charge on the pore walls as indicated by the nature of transport through the $\text{MF}_{\text{OH-V}}$ at (b) pH 3 and (d) pH 6. Please note that it is possible that there are silanols which are ionised at pH 3 also but they have not been indicated since they would be ionised at pH 6 as well.

Functionalization of MF_{OH}-V with pyranine was carried out by soaking it in 1 mM solution of pyranine at pH 3 for 3 h. The UV-visible spectrum of MF_{OH}-V functionalized with pyranine (MF_{OH}-V-P) shows the signature absorption bands of pyranine indicating its presence (Figure 6a). The cyclic voltammograms for MF_{OH}-V-P at pH 6 show cation selective transport (Figure 6b) only in the presence of 0.5 mM pyranine. When there was no pyranine in the solution, it shows ambipolar transport (Figure 6c). This implies that in the absence of pyranine in solution some of the bound pyranine comes out to the solution leaving the pore wall in a “nearly charge-balanced state” which is evident from the ambipolar nature^[13] of ion transport. The term “nearly charge-balanced” has been used to accommodate the fact that the ion transport is partially biased towards cation selective. The ionization of silanols at pH 6 also contributes to the neutralization of the positive charge of the viologen along with the pyranine molecules bound to viologen (Figure 6d). The weak binding of pyranine to viologen could in part be due to the electrostatic repulsion between the negatively charged silanol groups and the triply negatively charged pyranine. In the presence of excess pyranine in solution, the equilibrium is shifted towards charge-transfer complex formation which leads to negatively charged pore walls encouraging positive ion transport. It should be noted that there is still a discernible electrochemical response for negatively charged [Fe(CN)₆]³⁻ indicating that the reversal of charge is not complete and that some viologen moieties are still left unbound (Figure 6e).

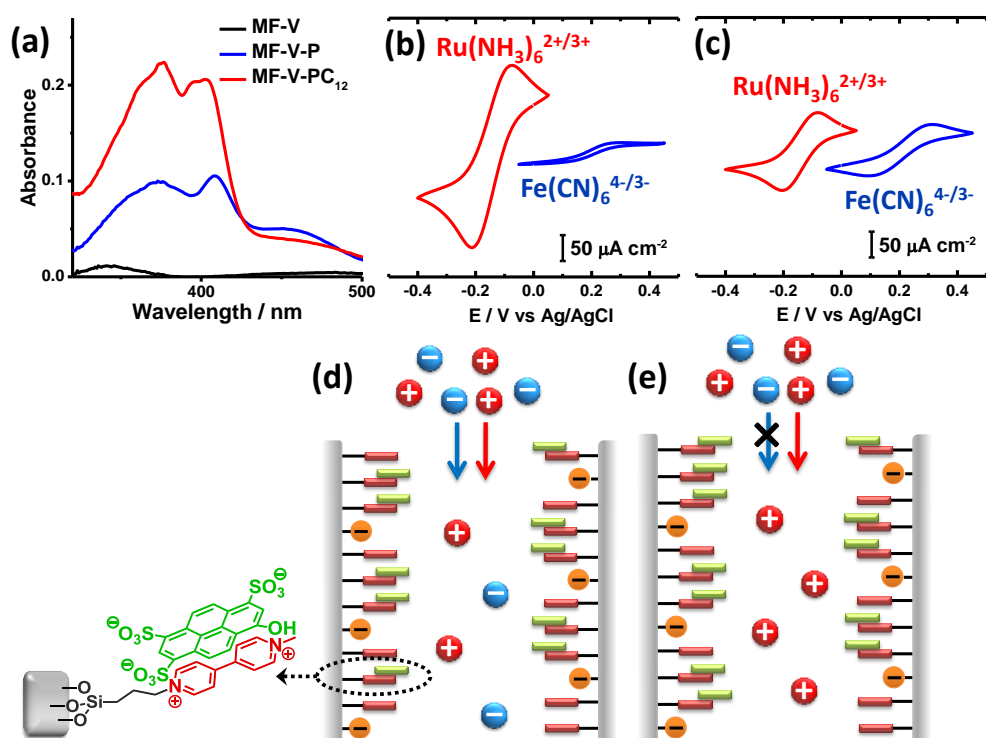


Figure 6. (a) UV-visible spectra of the MF_{OH}-V, MF_{OH}-V-P and MF_{OH}-V-PC₁₂ films showing the characteristic absorption for pyranine at 405 nm and 380 nm indicating presence of

pyranine and PC₁₂ in the films. Cyclic voltammograms were recorded in presence of 1 mM [Ru(NH₃)₆]³⁺ (red trace) and 1 mM [Fe(CN)₆]³⁻ (blue trace) on MF-V_{OH}-P films at pH 6 (b) in presence of pyranine (0.5 mM) and (c) in absence of pyranine in solution. Scan Rate: 200 mV/s. Supporting electrolyte: 0.1 M KCl. Schematics qualitatively depicting the charge on the pore walls as indicated by the nature of transport through MF_{OH}-V-P films in (d) absence and (e) presence of pyranine in solution.

Hydrophobic interactions have been known to improve the strength of non-covalent interactions and have been the driving force behind many amphiphilic assemblies^[6a] which are known to have very strong association. In order to utilise these hydrophobic interactions, pyranine appended with a dodecyl alkyl group, PC₁₂, was used as a donor (Figure 7). MF_{OH}-V films were soaked in 1 mM PC₁₂ solution at pH 3 for 3 h to form MF_{OH}-V-PC₁₂@pH3. The UV-visible spectra of MF_{OH}-V soaked in PC₁₂ at pH 3 show the signature absorption bands of pyranine indicating the inclusion of PC₁₂ into the film (Figure 6a). The cyclic voltammograms recorded at pH 6 on these films, show a very strong electrochemical response for positively charged [Ru(NH₃)₆]³⁺ and no response for negatively charged [Fe(CN)₆]³⁻ indicating complete reversal of charge (Figure 8a). This implies that unlike pyranine, PC₁₂ exhibits stronger binding to viologen and does not come into the solution. The cyclic voltammograms carried out over pyranine bound MF_{OH}-V (referred as MF_{OH}-V-P) soaked in PC₁₂ for 1 h clearly shows the shift from ambipolar transport (observed for MF_{OH}-V-P) to cation selective transport (Figure 8c and 8f). This change in the nature of ion transport from ambipolar to cation selective in presence of PC₁₂ clearly suggests the strong binding affinity associated with PC₁₂ in comparison to pyranine. Absence of any discernible electrochemical response for negatively charged [Fe(CN)₆]³⁻ in 2 h time indicates complete charge reversal (Figure 8f). The strong binding PC₁₂ not only displaced the pyranine bound to viologen but also complexed with viologens left unoccupied in MF_{OH}-V-P, to induce a complete reversal of charge (Figure 8d). This suggests that the hydrophobic interaction between the alkyl groups has increased the binding strength and stabilised the supramolecular assembly. The diffuse reflectance infra-red fourier transform spectrum (DRIFTS) of MF_{OH}-V film soaked in PC₁₂ at pH 3, show evidence of alkyl chain packing^[14] confirming the involvement of hydrophobic interactions (Figure 8g).

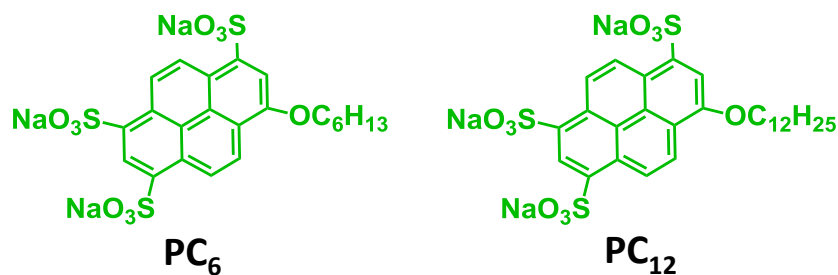


Figure 7. Molecular structures of the pyranine derivatives used in this study. PC_6 : Trisodium-8-hexyloxyppyrene-1,3,6-trisulfonate; PC_{12} : Trisodium-8-dodecyloxyppyrene-1,3,6-trisulfonate.

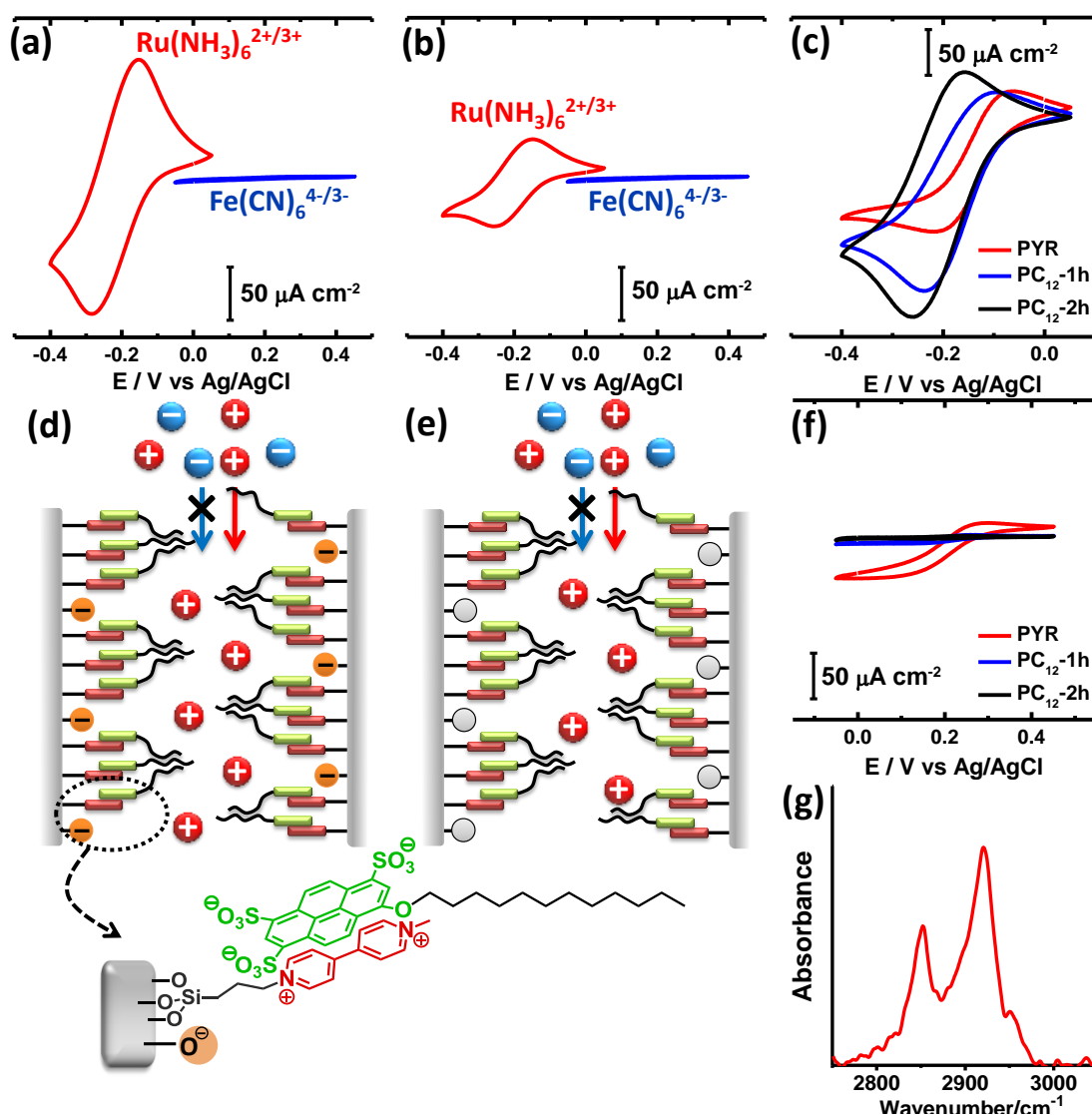


Figure 8. Cyclic voltammograms were recorded at different pH values in the presence of 1 mM $[Ru(NH_3)_6]^{3+}$ (red trace) and 1 mM $[Fe(CN)_6]^{3-}$ (blue trace) on MF_{OH^-} -V films soaked in PC_{12} at pH 3 - (a) pH 6 and (b) pH 3. Scan Rate: 200 mV/s. Supporting electrolyte: 0.1 M KCl. Schematics qualitatively depicting the charge on the pore walls as indicated by the asymmetry of transport through the MF_{OH^-} -V films soaked in PC_{12} (pH 3) at (d) pH 6 and (e) pH 3. Cyclic

voltammograms recorded with (c) 1 mM of $[Ru(NH_3)_6]^{3+}$ and (f) 1 mM of $[Fe(CN)_6]^{3-}$ on MF_{OH} films soaked in pyranine for 3 h at pH 3 (PYR) and after subsequent soaking in 1 mM PC_{12} at the same pH for 1 h (PC_{12} -1h) and 2 h (PC_{12} -2h). All of the cyclic voltammograms were recorded in the absence of excess donor in solution. (g) Diffuse reflectance infra-red fourier transform spectra of the MF_{OH} -V- PC_{12} @pH3 film showing asymmetric (CH_2) and symmetric (CH_2) stretches at lower wavenumbers ($\nu_{as} - 2920\text{ cm}^{-1}$, $\nu_s - 2852\text{ cm}^{-1}$) indicating packing of alkyl chains.

As was noted previously, the silanol groups on the pore wall contribute to the negative charge to some extent at pH 6. To discern the contribution of PC_{12} towards the overall negative charge on the pore wall, the transport properties of the MF_{OH} -V- PC_{12} @pH3 film were studied at pH 3 where there is a minimal participation of silanols. The cyclic voltammograms recorded at pH 3, show that the transport is still cation selective. It is important to note that even at pH 3, where the ionization of the silanols is minimal, the electrochemical response for negatively charged $[Fe(CN)_6]^{3-}$ is completely suppressed (Figure 8b). This indicates that most of the viologen moieties are bound to PC_{12} (Figure 8e). So, the silanol groups only served to increase the overall negative charge on the pore walls (Figure 8d). Earlier, we saw that the ionization of silanols reduced the negative ion transport through MF_{OH} -V films but here they lead to an increase in positive ion transport through the MF_{OH} -V- PC_{12} @pH3 films. This can be rationalised by considering the fact that in the case of MF_{OH} -V the negative charge on silanols was working against the predominant positive charge on the pore walls due to the viologen moieties but here they are adding to the negative charge already built up on the pore wall due to the binding of PC_{12} to viologen moieties.

To understand the effect of the negatively charged silanol moieties on the supramolecular assembly of PC_{12} in MF_{OH} -V- PC_{12} @pH6 (obtained by soaking MF_{OH} -V in PC_{12} at pH 6 for 3 h), the transport studies were carried out at pH 6 and at pH 3. At pH 6, the MF_{OH} -V- PC_{12} @pH6 showed highly selective cation transport with a very stifled response for negatively charged $[Fe(CN)_6]^{3-}$ (Figure 9a). Whereas, at pH 3, it showed ambipolar transport allowing both positively and negatively charged redox probes (Figure 9c). This suggests that PC_{12} is only balancing the positive charge of the viologen moieties and the negative charge from the silanol moieties induces cation selective transport at pH 6 (Figure 9b and 9d). It is understandable that to neutralise the charge due to viologen moieties, two-thirds of them should be bound to PC_{12} as indicated in the schematic (Figure 9b and 9d). So, silanol groups do affect the supramolecular assembly of PC_{12} depending on the pH and the assemblies formed modulate the transport differently with respect to pH. Even though both donor and acceptor in both cases are the same, the pH at which the assembly was carried out greatly influences the outcome.

Figure 10 summarises the various modes of ion transport possible by simply changing the pH at which the assembly of PC₁₂ was carried out. The fact that when transport across MF_{OH}-V-PC₁₂@pH3 is studied at pH 6, it shows greater cation selectivity than MF_{OH}-V-PC₁₂@pH6 which implies that it doesn't reorganise to the state of MF_{OH}-V-PC₁₂@pH6. This implies that PC₁₂ is more strongly bound to MF_{OH}-V when the assembly was performed at pH 3. It can be rationalised by considering the fact that the increase in binding strength of PC₁₂ in comparison to pyranine was due to the cohesive hydrophobic interactions between pendant alkyl chains. The diffuse reflectance infra-red fourier transform spectra (DRIFTS) of MF_{OH}-V-PC₁₂@pH3 and MF_{OH}-V-PC₁₂@pH6, both show evidence of alkyl chain packing (Figure 9g). It is expected that with increase in the number and packing density of alkyl chains, the hydrophobic interactions become stronger and hence in the case of MF_{OH}-V-PC₁₂@pH3 where the number of PC₁₂ bound to viologen is maximum, the hydrophobic interactions are much stronger and hold the assembly together even when the pH is raised to 6 where the silanol groups become negatively charged and could destabilise the C-T pair. It is clear from these observations, that a weak C-T pair can be made strong by bringing cohesive hydrophobic interactions between donors through the attachment of long alkyl chain pendants. Moreover, the kinetics of assembly was also found to be fast. The kinetics of binding of PC₁₂ to MF_{OH}-V was monitored at 10 minute intervals through cyclic voltammetry. Within 20 minutes of soaking, the cation transport reached saturation (Figure 9e) and the anion transport was totally suppressed (Figure 9f). The assemblies in MF_{OH}-V-PC₁₂@pH3 were found to be quite stable even on soaking in water for extended periods of time which avoids the use of excess donors in the solution during transport measurement of non-covalent systems to maintain stability. The transport properties of the film remained cation selective even on soaking in water for around 10 h (Figure 11b). There was a 30% decrease in the electrochemical current for positively charged [Ru(NH₃)₆]³⁺ but no significant change in the anion current density (Figure 12a-b). The decrease in cation flux is due to the unbinding of PC₁₂ from MF_{OH}-V on extended soaking in water which was immediately regenerated by soaking in PC₁₂ solution at pH 3 for just 10 minutes (Figure 11a-b).

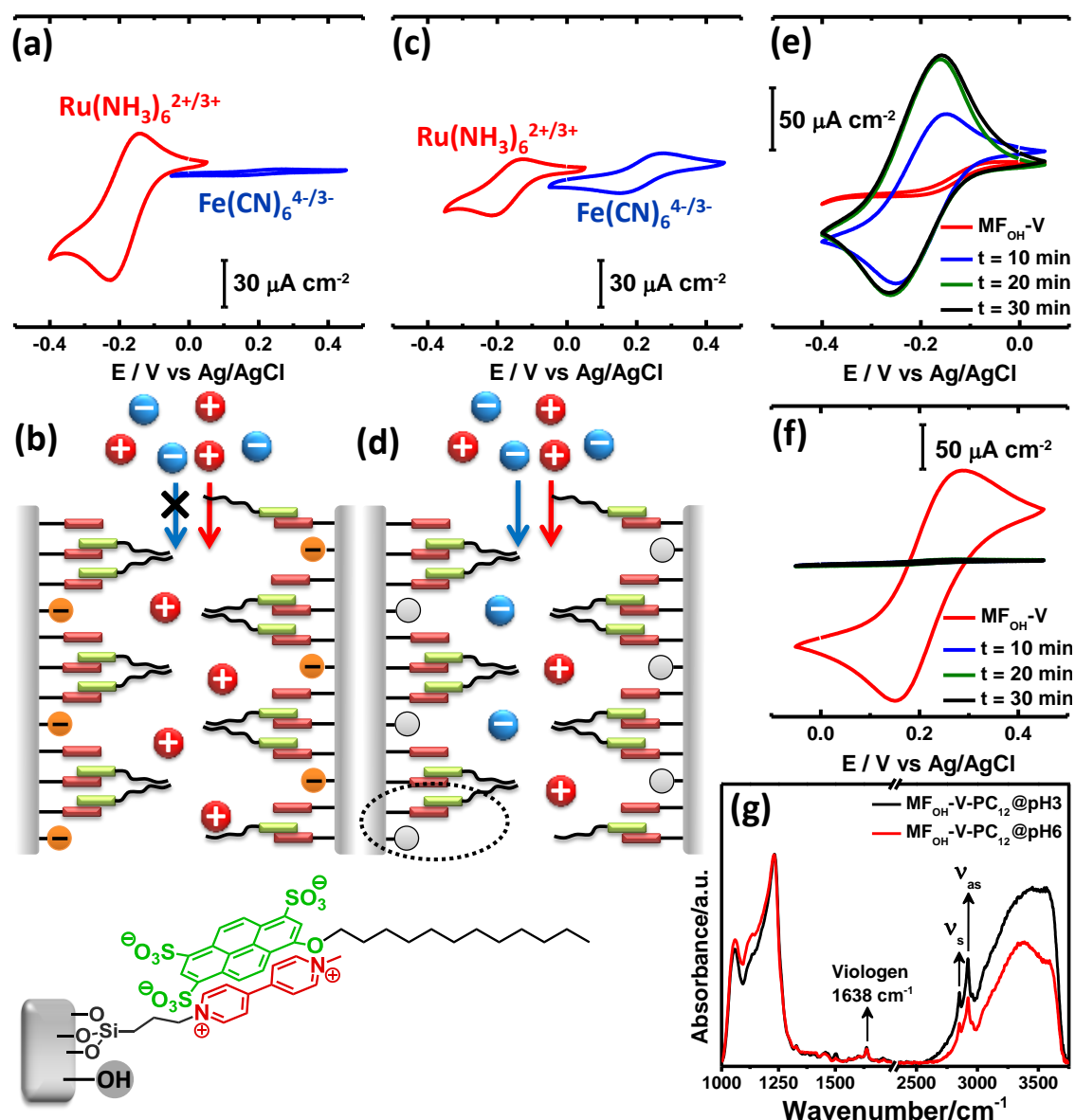


Figure 9. Cyclic voltammograms were recorded in the presence of 1 mM $[\text{Ru}(\text{NH}_3)_6]^{3+}$ (red trace) and 1 mM $[\text{Fe}(\text{CN})_6]^{3-}$ (blue trace) on $\text{MF}_{\text{OH}}\text{-V-PC}_{12}$ @pH6 films at (a) pH 6 and (c) pH 3 in the absence of donor in solution. Scan Rate: 200 mV/s. Supporting electrolyte: 0.1 M KCl. Schematics qualitatively depicting the charge on the pore walls as indicated by the nature of transport through the $\text{MF}_{\text{OH}}\text{-V-PC}_{12}$ @pH6 films at (b) pH 6 and (d) pH 3. (e) Cyclic voltammograms recorded on $\text{MF}_{\text{OH}}\text{-V}$ at pH 6 in the presence of 1 mM $[\text{Ru}(\text{NH}_3)_6]^{3+}$ for different durations of soaking in 1 mM PC_{12} (at pH 3), showing completion of functionalization within 20 minutes. (f) Cyclic voltammograms recorded in the presence of 1 mM $[\text{Fe}(\text{CN})_6]^{3-}$ at pH 6 on $\text{MF}_{\text{OH}}\text{-V}$ film with increase in time of soaking in 1 mM PC_{12} (at pH 3), showing immediate blocking of anion transport. (g) DRIFT spectra of $\text{MF}_{\text{OH}}\text{-V}$ films soaked in 1 mM PC_{12} (at pH 3 and pH 6), showing asymmetric and symmetric stretches at lower wavenumbers ($\nu_{\text{as}} - 2920 \text{ cm}^{-1}$, $\nu_{\text{s}} - 2852 \text{ cm}^{-1}$) indicating packing of alkyl chains.

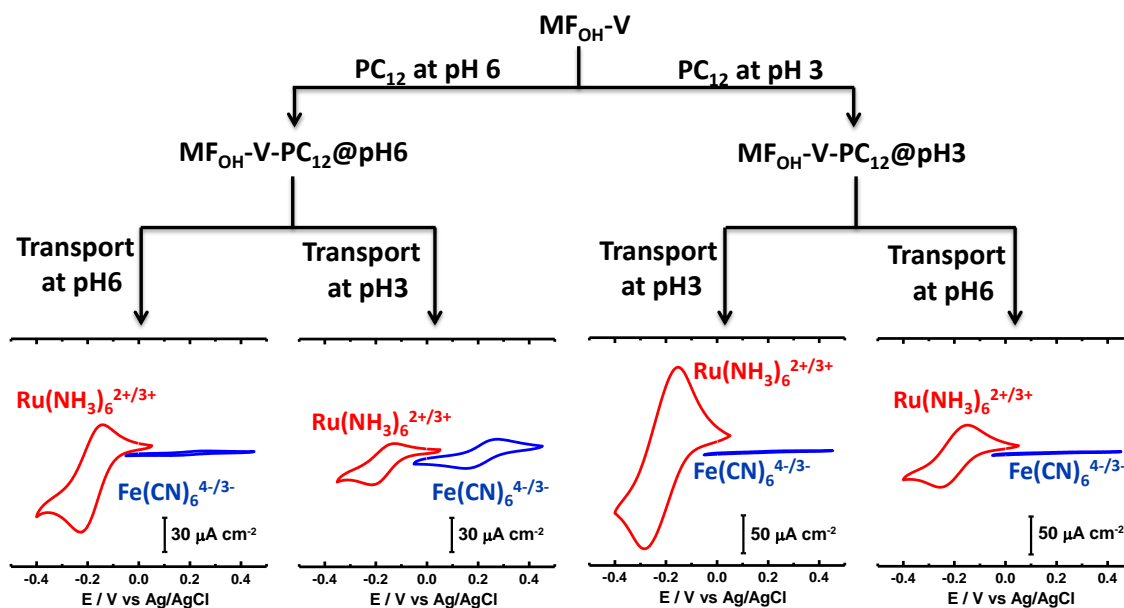


Figure 10. A brief overview of the various modes of transport shown by the assemblies of PC₁₂ at different pH values.

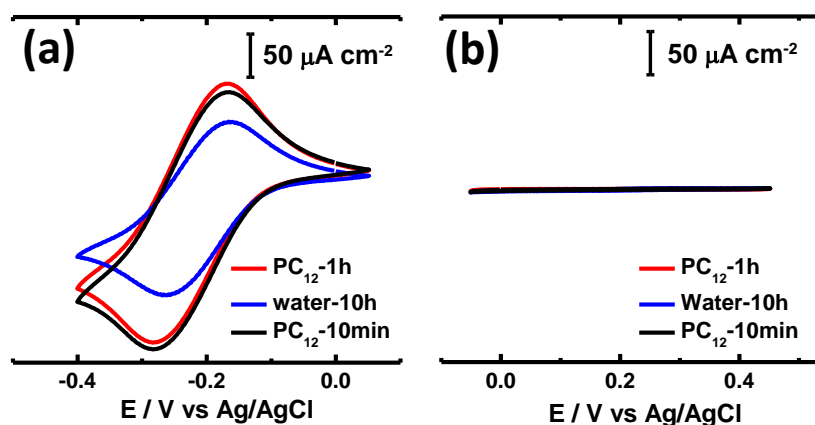


Figure 11. Cyclic voltammograms were recorded on MF_{OH}-V in the presence of (a) 1 mM [Ru(NH₃)₆]³⁺ and (b) 1 mM [Fe(CN)₆]³⁻ after soaking in PC₁₂ (pH 3) for 1 h, water for 10 h and PC₁₂ (pH 3) again for 10 minutes to check the stability and reversibility of functionalization. Rate: 200 mV/s. Supporting electrolyte: 0.1 M KCl

It is known that the strength of hydrophobic effect increases steeply with the length of alkyl chain. The use of a hexyl chain appended pyranine, PC₆, could only neutralise the pore walls of MF_{OH}-V at pH 6 to allow ambipolar transport (Figure 12a,b). On subsequent soaking in PC₁₂ solution at pH 3 for 2 h, the transport properties switched to cation selective as in the case of MF_{OH}-V-PC₁₂ indicating displacement of weakly binding PC₆ from viologen by PC₁₂ (Figure 12c). The DRIFT spectrum of MF_{OH}-V-PC₆ doesn't show any distinct signature of alkyl chain packing unlike MF_{OH}-V-PC₁₂ (Figure 9g). It is worth noting that the non-covalent nature of

these assemblies is responsible for their dynamic nature and ability to reorganise and reconfigure in the presence of a stronger stimulus to attain the most stable state under the given conditions.

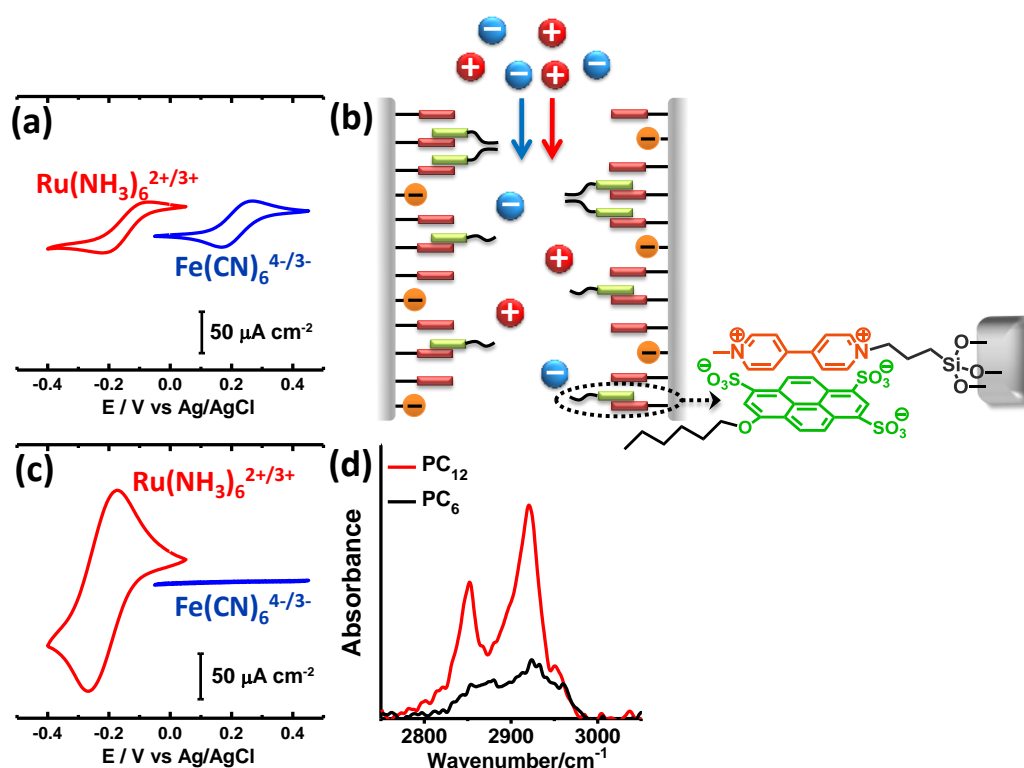


Figure 12. Cyclic voltammograms recorded at pH 6 in the presence of 1 mM $[Ru(NH_3)_6]^{3+}$ (red trace) and 1 mM $[Fe(CN)_6]^{3-}$ (blue trace) over (a) $MF_{OH-V-PC_6}$ showing ambipolar transport which changes to (c) cation selective transport on soaking for 2 h in 1 mM solution of PC_{12} at pH 3. Rate: 200 mV/s. Supporting electrolyte: 0.1 M KCl. (b) Schematic qualitatively depicting the charge on the pore walls as indicated by the nature of transport through the $MF_{OH-V-PC_6}$ films at pH 6. (d) DRIFT spectra of $MF_{OH-V-PC_6}$ film showing no signs of alkyl chain packing like in the case of $MF_{OH-V-PC_{12}}$ film.

To examine the importance of charge-transfer interactions, an electrostatic blank (MF_{OH-B}) was prepared by functionalising the pore walls with a quaternary ammonium silane (Figure 13). The transport properties of MF_{OH-B} were similar to that of MF_{OH-V} showing anion selective transport (Figure 14a). MF_{OH-B} soaked in PC_{12} at pH 3 for 3 h, showed ambipolar transport at pH 6 indicating only neutralization of charges on the pore wall, unlike $MF_{OH-V-PC_{12}}$ which shows cation selective transport. On subsequent soaking in water for 30 minutes the transport switched back to anion selective (Figure 14b) but the anion selectivity is still lower than native MF_{OH-B} (not soaked in PC_{12}). This indicates that PC_{12} is still bound to MF_{OH-B} causing a larger electrochemical response for positively charged $Ru(NH_3)_6^{3+}$ than in MF_{OH-B}

(not soaked in PC₁₂). The DRIFTS spectra of PC₁₂ soaked MF_{OH}-B showed signs of alkyl chain packing (Figure 14c).

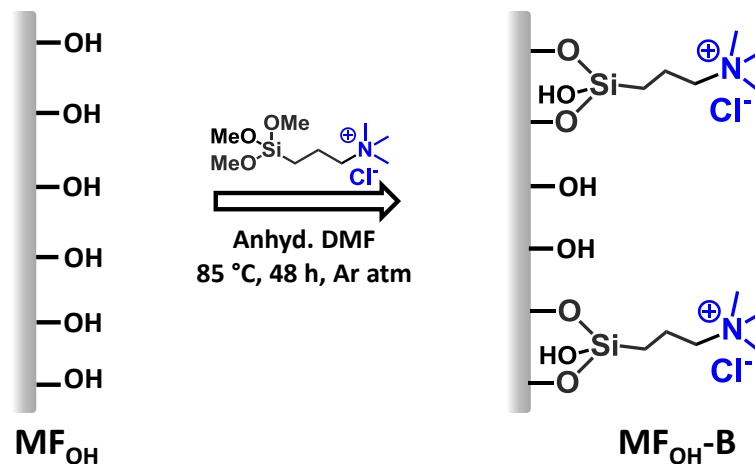


Figure 13. Schematic showing the synthetic approach followed for preparing MF_{OH}-B. It is important to note that there are a significant number of silanols which are not passivated on functionalization.

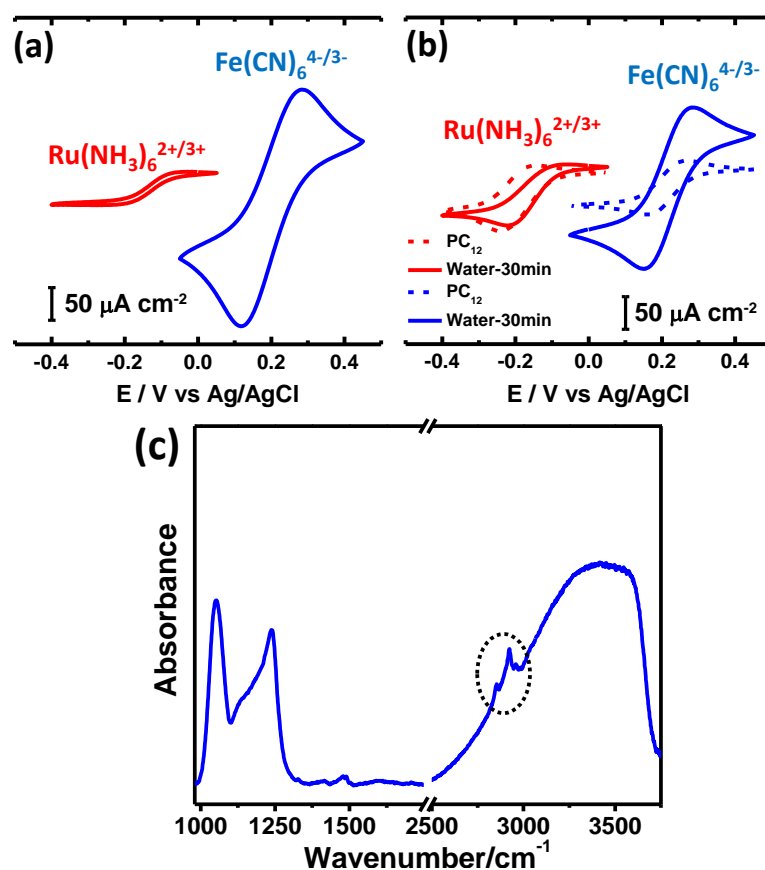


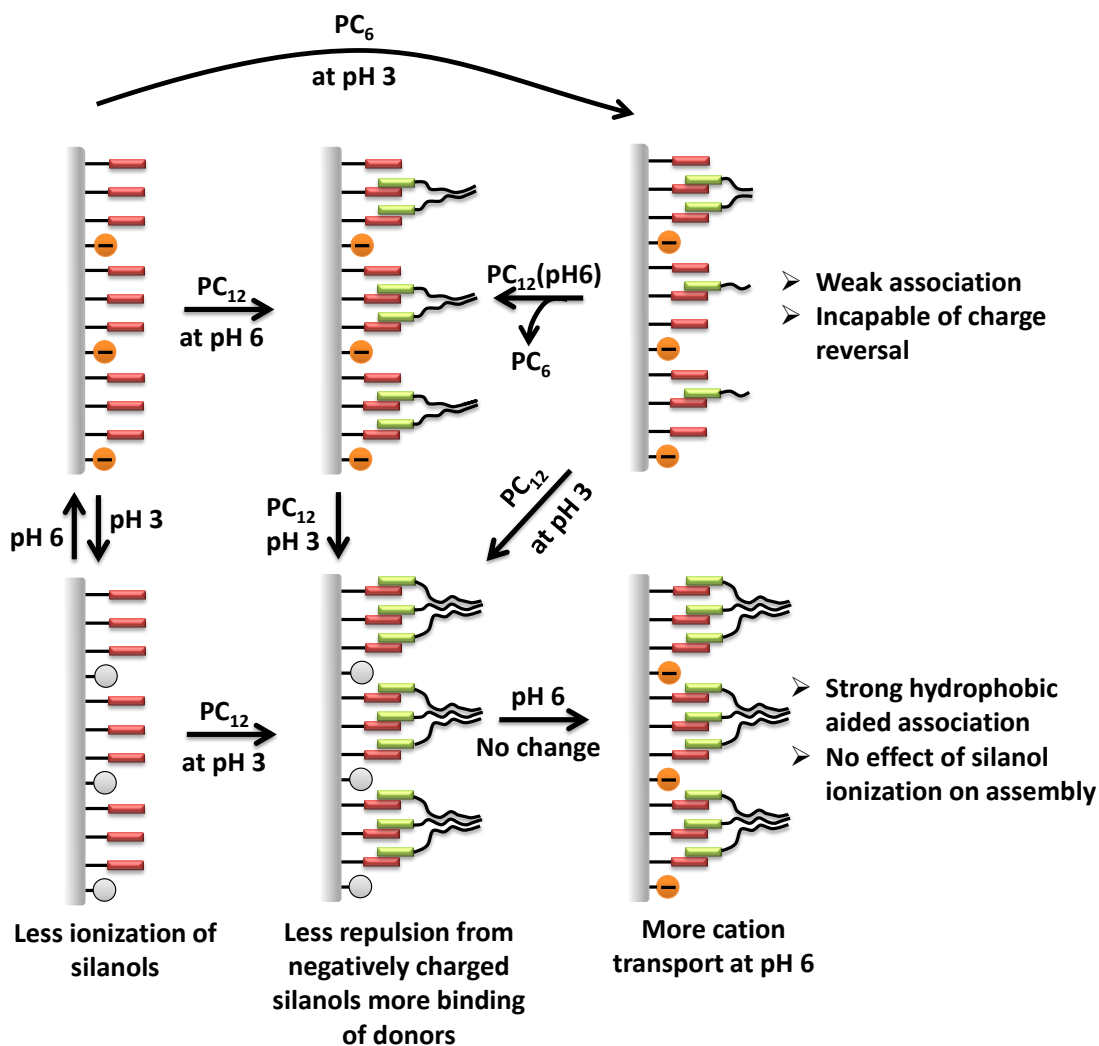
Figure 14. Cyclic voltammograms recorded in the presence of 1 mM [Ru(NH₃)₆]³⁺ (red trace) and 1 mM [Fe(CN)₆]³⁻ (blue trace) at pH 6 for (a) MF-B and (b) MF-B soaked in 1 mM solution of PC₁₂ at pH 3 for 3 h (dotted traces) and subsequent soaking in water for 30 minutes

(solid traces). Rate: 200 mV/s. Supporting electrolyte: 0.1 M KCl. (c) DRIFT spectrum MF_{OH-B} films soaked in 1 mM PC₁₂ at pH 3 showing some amount of alkyl chain packing.

It is to be noted that MF-B (Chapter 4.1) on soaking with pyranine does not change the nature of transport. On the other hand, soaking of MF_{OH-B} in PC₁₂ switched the transport from anion selective to ambipolar even though it was not stable. This can be understood by considering the fact that the binding of PC₁₂ has a hydrophobic component which is independent of C-T and still shows some amount of binding for PC₁₂. So, we see that C-T interactions which contribute only a part of the binding energy are nevertheless very important in achieving charge reversal and in maintaining the stability of these assemblies in confined environment.

4.2.5. Conclusions

In conclusion, we have demonstrated a simple generic strategy to improve the association of non-covalent motifs to achieve charge reversal within confined pores of less than 10 nm. The use of dodecyl appended pyranine not only enabled the switching of transport properties from anion selective to cation selective but also allowed the films to operate for extended periods of time in the absence of excess donor in solution. The length of the alkyl chain appended was found to be very crucial and the use of a shorter hexyl chain appended pyranine, PC₆, could not achieve charge reversal, rather only neutralised the charge on the pore walls to achieve ambipolar transport (Scheme 2). In the presence of a strong donor the assembly reorganised to incorporate the stronger binding component (dynamic in nature) and the permselectivity of the films could be switched accordingly (Scheme 2). The application of this hydrophobic interaction aided strategy for the weak non-covalent motifs will enable their use in creating a wide range of dynamic assemblies capable of responding to a variety of stimuli.



Scheme 2. A brief overview of the various supramolecular assemblies of PC₁₂ and PC₆ formed on the pore walls and their reorganization based on strength of association.

4.1.6. References

- [1] B. Hille, *Ion Channels of Excitable Membranes, 3rd Edition*, Sinauer, **2001**.
- [2] R. Karnik, C. Duan, K. Castelino, H. Daiguji, A. Majumdar, *Nano Lett.* **2007**, 7, 547-551.
- [3] B. Yameen, M. Ali, R. Neumann, W. Ensinger, W. Knoll, O. Azzaroni, *Nano Lett.* **2009**, 9, 2788-2793.
- [4] L. Wen, Q. Liu, J. Ma, Y. Tian, C. Li, Z. Bo, L. Jiang, *Adv. Mater.* **2012**, 24, 6193-6198.
- [5] B. V. V. S. P. Kumar, K. V. Rao, T. Soumya, S. J. George, M. Eswaramoorthy, *J. Am. Chem. Soc.* **2013**, 135, 10902-10905.
- [6] a) J. D. Hartgerink, E. Beniash, S. I. Stupp, *Proceedings of the National Academy of Sciences* **2002**, 99, 5133-5138; b) E. Obert, M. Bellot, L. Bouteiller, F. Andrioletti, C.

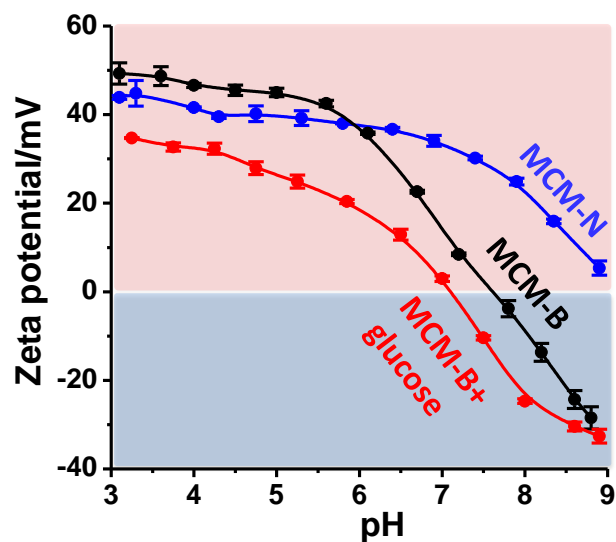
- Lehen-Ferrenbach, F. Boué, *J. Am. Chem. Soc.* **2007**, *129*, 15601-15605; c) G. V. Oshovsky, D. N. Reinhoudt, W. Verboom, *Angew. Chem. Int. Ed.* **2007**, *46*, 2366-2393.
- [7] a) J. P. Hill, W. Jin, A. Kosaka, T. Fukushima, H. Ichihara, T. Shimomura, K. Ito, T. Hashizume, N. Ishii, T. Aida, *Science* **2004**, *304*, 1481-1483; b) G. Zhang, W. Jin, T. Fukushima, A. Kosaka, N. Ishii, T. Aida, *J. Am. Chem. Soc.* **2006**, *129*, 719-722.
- [8] E. Krieg, H. Weissman, E. Shirman, E. Shimoni, B. Rybtchinski, *Nat Nano* **2011**, *6*, 141-146.
- [9] D. Zhao, P. Yang, N. Melosh, J. Feng, B. F. Chmelka, G. D. Stucky, *Adv. Mater.* **1998**, *10*, 1380-1385.
- [10] F. Tian, N. Cheng, N. Nouvel, J. Geng, O. A. Scherman, *Langmuir* **2010**, *26*, 5323-5328.
- [11] R. Martín, P. C. Heydorn, M. Alvaro, H. Garcia, *Chem. Mater.* **2009**, *21*, 4505-4514.
- [12] A. Calvo, B. Yameen, F. J. Williams, G. J. A. A. Soler-Illia, O. Azzaroni, *J. Am. Chem. Soc.* **2009**, *131*, 10866-10868.
- [13] S. B. Lee, C. R. Martin, *Anal. Chem.* **2001**, *73*, 768-775.
- [14] a) R. R. San Juan, T. B. Carmichael, *Langmuir* **2012**, *28*, 17701-17708; b) M. D. Porter, T. B. Bright, D. L. Allara, C. E. D. Chidsey, *J. Am. Chem. Soc.* **1987**, *109*, 3559-3568.

Chapter-4.3

Glucose- and pH-Responsive Charge-Reversal Surfaces

Summary

We have shown a pH and glucose responsive charge-reversal on silica surface through heterogeneous functionalization utilising amines and boronic acid moieties. The dual responsiveness of the charge reversal has been unambiguously demonstrated through desorption of charged chromophores. Interestingly, we observed a concentration dependent desorption response to glucose at physiologically relevant levels.



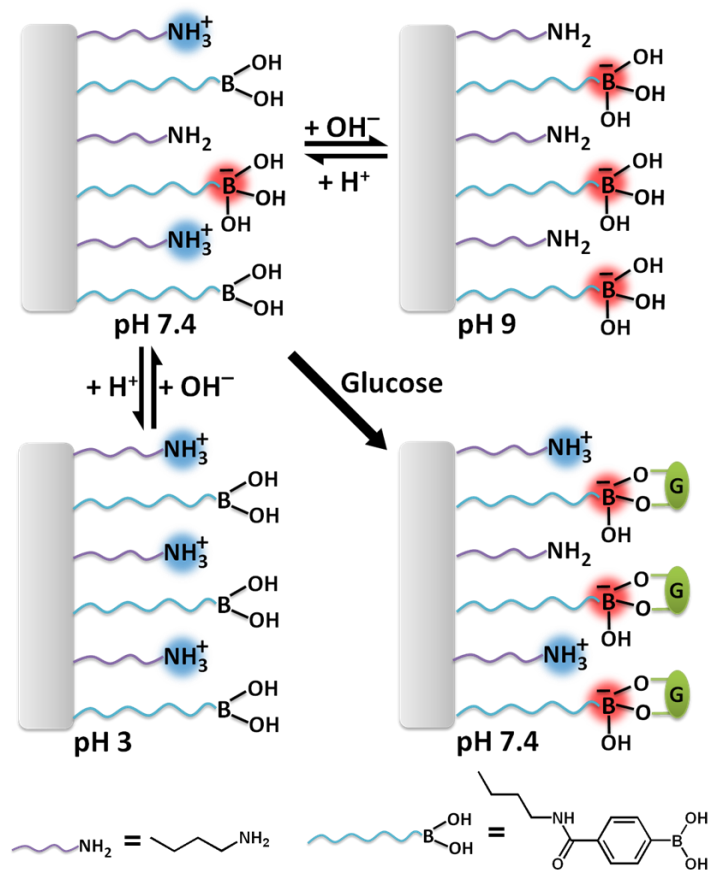
Publication based on this work has appeared in *Langmuir*, 2014, 30, 4540-4544.

4.3.1. Introduction

Systems capable of having charge reversal have attracted a lot of attention in recent years by virtue of their applications in switchable assemblies,^[1] permselective transport,^[2] controlled cell adhesion,^[3] drug/gene delivery,^[4] switchable electrode interfaces^[5] and bacterial targeting.^[6] Many covalent approaches have been designed to achieve charge reversal in response to a variety of stimuli. pH-responsive charge reversal surfaces were designed by utilizing the dissociation equilibria of acidic and basic functional groups either in the same molecule^[7] or copolymer.^[4b] Other designs were based on pH-sensitive charge-masking groups^[8] which hydrolyse in response to pH and cause charge reversal. Light responsive charge reversal surfaces were mainly based on the reversible charging of spiropyran^[9] or malachite green^[10] moieties. Another approach was the use of photocleavable linkers^[1a] to deprotect ionisable functional groups to achieve charge reversal. The charge-reversal systems designed so far, often respond to only one type of stimulus. To our knowledge, there are only few systems which are capable of responding to multiple stimuli and therefore, widening the scope of their application in various environments. Systems responding to both pH and biomolecule stimuli are well suited for application in living systems and more specifically for glucose responsive systems^[11] owing to the role of glucose as a ubiquitous fuel for biological systems. Furthermore, if the system responds to the stimulus in a quantitative way, it would help to regulate its response in a controlled fashion.

4.3.2. Scope of the present investigation

A heterogeneously functionalized mesoporous silica system has been used to achieve charge-reversal surfaces which respond to both pH and glucose. Mesoporous silica (MCM-41) was chosen as the scaffold to study charge-reversal due to its large and easily modifiable surface and its wide range of applications in biology. The surface was covalently functionalized with propylamine and phenylboronic acid groups (MCM-B) to impart pH-responsive charge-reversal. At low pH (< 6), the amine groups are mostly protonated and the boronic acid groups are largely in the neutral form, lending a positive charge to the surface. However, at high pH (> 8), the amine groups are sparsely protonated while the boronic acid binds with hydroxyl ion to form a negatively charged tetrahedral boronate ion, leaving the overall surface charge negative (Scheme 1). Additionally, shifting of equilibrium from neutral trigonal form of phenylboronic acid to its negatively charged tetrahedral form on binding to glucose^[12] at pH 7.4, was exploited for glucose responsive charge-reversal (Scheme 1). The glucose driven charge-reversal was a controlled process and exhibited quantitative response to the concentration of glucose.



Scheme 1. Schematic illustrating the dual mode charge reversal of heterogeneously functionalized mesoporous silica surface (MCM-B).

4.3.3. Experimental section

MCM-41

Mesoporous silica nanoparticles (MCM-41) were synthesized according to a reported procedure^[13]. 1.0 g (2.74 mmol) of hexadecyltrimethylammonium bromide (CTAB) and 0.28 g of NaOH was dissolved in 480 mL of millipore water under stirring (600 rpm) and the temperature was slowly raised to 80 °C. 5 mL (22.4 mmol) of tetraethylorthosilicate (TEOS) was added dropwise and the reaction mixture was stirred for 2 h at 80 °C. The white solid product was centrifuged, washed thoroughly with water followed by ethanol, and dried in an oven overnight. The surfactant template (CTAB) was removed from the obtained product by refluxing for 6 h in ethanol solution at pH 1 and washing thoroughly with millipore water and ethanol. The as-synthesized MCM-41 was dried under high vacuum.

MCM-N

1.0 g of surfactant free and degassed MCM-41 (1.0 g) and 1.0 ml (5.67 mmol) of (3-aminopropyl)triethoxysilane (APTES) was added to 80 ml of anhydrous toluene and then

refluxed under stirring for 24 h. The reaction mixture was centrifuged, washed extensively with toluene, hexane followed by ethanol, finally dried under high vacuum at 353 K for 6 h.

MCM-B

0.2 g (1.74 mmol) of N-hydroxysuccinimide (NHS) and 0.4 g (2.08 mmol) of 1-ethyl-3-(3-dimethylaminopropyl)carbodiimide hydrochloride (EDC) were first dissolved in 10 mL of anhydrous DMF and then 0.3 g (1.8 mmol) of 4-carboxyphenylboronic acid (CPBA) was added. This reaction mixture was stirred at room temperature under inert atmosphere for 15 min before adding to a dispersion of MCM-N in 40 ml of anhydrous DMF. The mixture was stirred for another 24 h, followed by centrifugation and washing with DMF, water and finally with methanol. The obtained product was then dried under high vacuum at 353 K for 6 h.

Sample preparation for nitrogen adsorption-desorption

The samples were degassed at 85 °C for 12 h under high vacuum and then nitrogen adsorption-desorption experiments were carried out at 77 K.

Preparation of ninhydrin solution and quantification of amine groups

Standard solutions of n-propylamine were used to obtain a calibration curve for the quantification of amines using the ninhydrin test.^[14] 0.266 g ninhydrin was dissolved in 10 mL dimethyl sulfoxide (DMSO), followed by addition of 0.04 g hydrindantin under nitrogen purge. The mixture was sonicated for 10 min to form a clear solution. 3.3 mL of 4 N lithium hydroxide/acetic acid buffer (pH 5) was added to 10 mL of ninhydrin solution and purged with nitrogen gas for 10 min.

1 mL of ninhydrin solution was added to different n-propylamine standard solutions (each 1 mL), 5 mg MCM-N in 1 mL millipore water and 5 mg MCM-B in 1 mL millipore water. These solutions were placed in screw capped test tubes and heated in a water bath at 80 °C for 30 min. The reaction mixture was immediately allowed to cool in an ice bath, for 5 min. Then, 20 mL of 50 % ethanol was added to each test tube and thoroughly mixed with a vortex mixer. The solutions were further diluted three times in order to obtain good absorption spectra. The absorbance of each reaction mixture was measured at 572 nm.

Alizarin Red S assay for boronic acid groups in MCM-B

The accessibility of boronic acid groups in MCM-B to cis-diols was examined by using the fluorescent reporter alizarin red S (ARS) according to reported literature procedure.^[15] Typically, 10^{-4} M ARS solution was first prepared in 10 mM tris-HCl buffer (pH 7.4). Increasing amounts of MCM-B were added to ARS solution and the fluorescence emission

intensities were measured at the wavelength of 572 nm with an excitation wavelength at 468 nm. A reverse titration was also performed, where increasing amounts of glucose were added to a 5 ml dispersion of MCM-B (0.8 mg/mL) in a solution containing 10^{-4} M of ARS and emission spectra were recorded after each successive addition.

Dye loading

a) For glucose responsive desorption. 5 mg of MCM-B was dispersed in 1 mL of 10 mM HEPES buffer solution (pH = 7.4) containing 1 mM brilliant yellow (BY) or crystal violet (CV) or 1,3,6,8-Pyrenetetrasulfonic acid (PTSA). The suspension was stirred for 12 h at room temperature for dye loading, centrifuged and washed extensively with HEPES buffer solution to remove physisorbed dye. The supernatant solution was collected to quantify the amount of dye loading.

b) For pH responsive desorption. MCM-B (5 mg) was dispersed in 1 mL of either brilliant yellow at pH 4 or crystal violet at pH 8.5. The suspension was stirred for 12 h at room temperature for dye loading, centrifuged, washed extensively either with pH 4 solution or with pH 8.5 solution to remove physisorbed dye. The supernatant solution was collected to quantify the amount of dye loading.

Glucose induced dye desorption

The glucose responsive dye desorption was carried out in three ways – single step cumulative, single step time profile and multiple steps. The single step release was carried out to understand the concentration dependence of desorption and the multiple step release was done to examine response to sequential addition glucose.

a) Single step (cumulative) desorption. The BY loaded MCM-B (3 mg) was dispersed in 4 mL of HEPES buffer (10 mM, pH 7.4) with different concentrations of glucose triggers at room temperature. The suspensions were centrifuged after 24 h and the supernatant was analysed using UV-visible absorption spectroscopy to monitor dye desorption.

b) Time dependent desorption. The dye (BY or CV) loaded MCM-B (5 mg) sample was dispersed in 5 mL of HEPES buffer (10 mM, pH 7.4) at room temperature. To this different amounts of glucose were added and desorption of dye was monitored in time. Aliquots (0.2 mL) were taken at predetermined time intervals to follow desorption of dye and the volume of the sample was adjusted with buffer (containing the same concentration of glucose as being used in the respective desorption study). The amount of dye released was monitored by UV-visible absorption spectroscopy.

c) Stepwise dye desorption. The dye (BY or PTSA) loaded MCM-B (5 mg) sample was dispersed in 5 mL of HEPES buffer (10 mM, pH 7.4) at room temperature. To this increasing amounts of glucose were added at intervals of 3 h. Aliquots (0.2 mL) were taken every hour to monitor the dye desorption and the volume of the sample was adjusted with buffer (containing glucose at the respective concentration in the desorption study). The amount of dye released was monitored by UV-visible absorption spectroscopy.

Saccharide induced dye desorption

a) Interference study at 0.1 mM. The MCM-B (5 mg) loaded with BY was dispersed in 5 mL of HEPES buffer (10 mM, pH 7.4) solution at room temperature. 0.1 mM D-fructose or 0.1 mM D-mannose was added to the suspensions after pre-determined time period. Aliquots (0.2 mL) were taken at pre-determined time intervals from the suspension to monitor BY desorption using UV-visible spectroscopy and the volumes were adjusted with buffer containing 0.1 mM of the respective saccharides.

b) Stepwise desorption. BY loaded MCM-B (5 mg) sample was dispersed in 5 mL of HEPES buffer (10 mM, pH 7.4) at room temperature. To this increasing amounts of mannose/fructose were added at intervals of 3 h. Aliquots (0.2 mL) were taken every hour to monitor the dye desorption and the volume of the sample was adjusted with buffer (containing saccharide at the respective concentration in the desorption study). The amount of dye released was monitored by UV-visible absorption spectroscopy.

pH induced dye desorption

The pH responsive dye desorption was carried out in two ways – single step and multiple steps. The single step experiment was carried out to understand the total extent of desorption and the multiple step experiment was done to examine the kinetics and the discreteness of desorption.

The pH of the solutions was adjusted using 10 mM HCl and NaOH.

a) Single Step desorption. Brilliant yellow or crystal violet loaded MCM-B (5 mg) was dispersed and allowed to soak in 5 mL solution maintained at pH 8.5 or pH 4 for 3h. The suspension was centrifuged and supernatant was analysed using UV-visible absorption spectroscopy to quantify the dye released.

b) Stepwise desorption. Brilliant yellow dye loaded MCM-B (5 mg) was dispersed in 5 mL of pH 4 solution at room temperature. The pH of the solution was gradually increased in small steps to pH 8.5. Aliquots (0.2 mL) were taken at regular intervals of 15 minutes to monitor the

dye desorption and the volume of the sample was adjusted with Millipore water. The amount of dye released was monitored by UV-visible absorption spectroscopy.

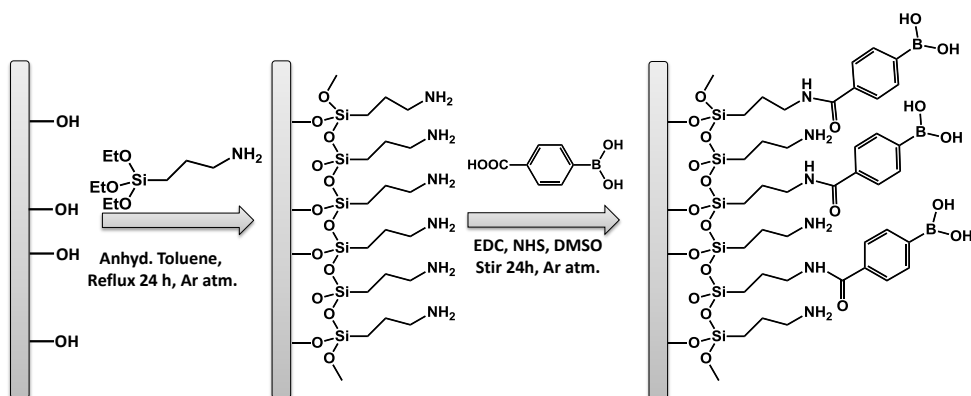
Crystal violet dye loaded MCM-B (5 mg) was dispersed in 5 mL of pH 8.5 solution at room temperature. The pH of the solution was gradually lowered in small steps to pH 4. Aliquots (0.2 mL) were taken at regular intervals of 15 minutes to monitor the dye desorption and the volume of the sample was adjusted with Millipore water. The amount of dye released was monitored by UV-visible absorption spectroscopy.

4.3.4. Characterization

Please refer to the appendix for the instrumental details of UV-visible spectroscopy, fluorescence spectroscopy, infra-red spectroscopy, nitrogen sorption analysis, thermogravimetric analysis, TEM, FESEM, XRD and zeta potential measurements.

4.3.5. Results and discussion

MCM-41 nanoparticles were prepared following a well-known procedure^[13] and the surface was functionalized with (3-aminopropyl)triethoxysilane to form MCM-N. The amine groups were then covalently linked with the COOH group of carboxyphenylboronic acid (CPBA) using EDC (1-Ethyl-3-(3-dimethylaminopropyl)carbodiimide) coupling to form MCM-B (Scheme 2).



Scheme 2. Schematic illustrating the synthetic strategy of MCM-B

The presence of a low angle peak in powder X-ray diffraction pattern of MCM-B confirms the retention of mesostructural ordering on functionalization (Figure 1a) which is further supported by the transmission electron microscopy (TEM) analysis (Figure 2a-b). FESEM images of MCM-B show fairly monodisperse particles of size 100 nm (Figure 2c-d). Thermogravimetric analysis shows an increase in organic content with subsequent functionalization steps indicating successful functionalization (Figure 1b).

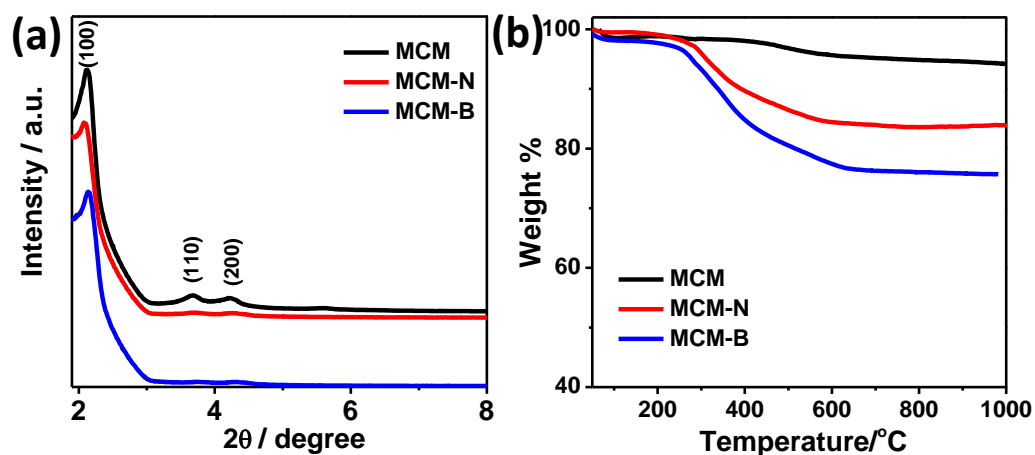


Figure 1. (a) Powder X-ray diffraction patterns of MCM, MCM-N and MCM-B showing retention of mesostructural ordering with the progress of functionalization. The secondary peaks [110] and [200] grow faint with functionalization. (b) Thermogravimetric analysis curves of MCM, MCM-N and MCM-B.

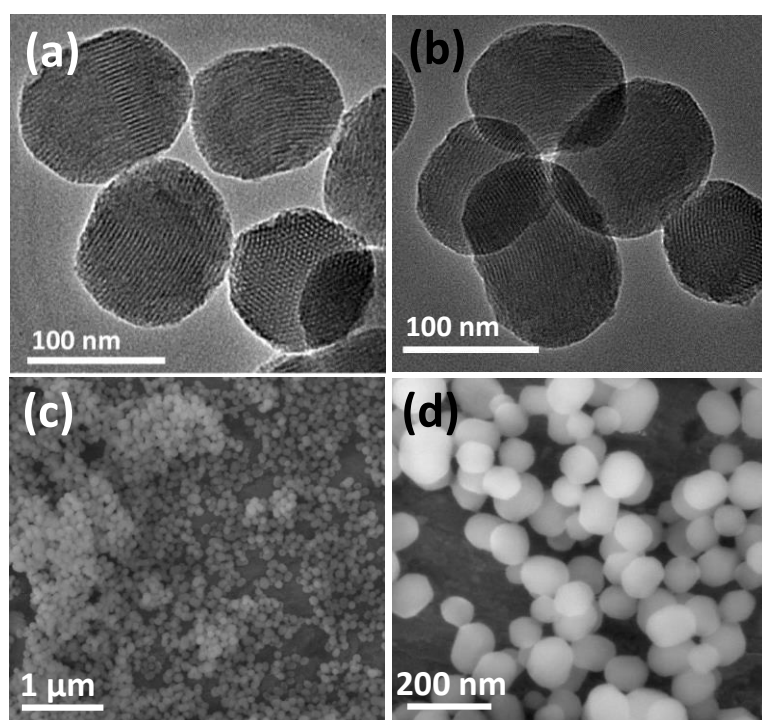


Figure 2. TEM images of (a) MCM and (b) MCM-B showing retention of mesostructural ordering. FESEM images showing MCM-B nanoparticles at (a) low and (b) high magnification.

Ninhydrin test^[14] was used to determine the amount of amine groups in MCM-N and MCM-B. The amount of unreacted amine groups in MCM-N and MCM-B were found to be 1.95 ± 0.07 mmol g⁻¹ and 0.95 ± 0.06 mmol g⁻¹ respectively (Figure 3). Using the data from

thermogravimetric analysis (TGA) and the unreacted amine functionalization density of MCM-B, it is possible to calculate the amount of amine groups coupled to carboxyphenylboronic acid in the following way:

TGA provided the weight of overall organic functionalization of MCM-B (19.8 %) and the ninhydrin test provided the amine content per unit weight of MCM-B (0.95 mmol/g).

Molecular weight of propylamine group = 58 g.

Molecular weight of phenylboronic acid conjugated propylamine = 207 g

In one gram of MCM-B total amount of organic functionalization = 0.198 g

$$\text{So, } (0.95 \times 10^{-3} \times 58) + [207 \times (x)] = 0.198$$

Then, $x = 0.69$ or 0.7 mmol approx.

So, the percentage of amine groups linked to phenylboronic acid in MCM-B = $0.7 / (0.7 + 0.95) \times 100 = 42.4 \%$

Therefore, roughly 40 % of the amine groups are coupled to carboxyphenylboronic acid through an amide bond in MCM-B. It should be noted that a calibration curve was obtained for ninhydrin test using propyl amine solutions (Figure 3) which was then used to quantify the amine groups in MCM-B.

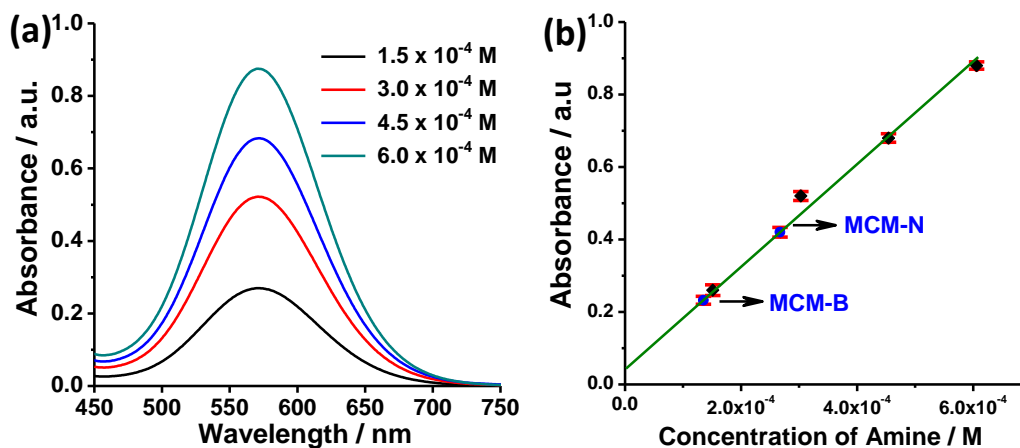


Figure 3. (a) UV-visible spectra of the ninhydrin complex in the calibration solutions. (b) Linear calibration plot showing increase in absorbance with increase in propylamine used in the standard solutions. The absorbance of the ninhydrin complex formed with MCM-N and MCM-B has been placed on the calibration curve to determine the concentration of amine groups. The error bars have been calculated from three replicates.

Nitrogen adsorption-desorption isotherms were recorded at 77 K to follow the progress of functionalization inside the pores (Figure 4a). The Barret-Joyner-Halenda (BJH) pore size distribution showed a gradual decrease in pore size from 2.4 nm (MCM) through 2.2 nm (MCM-N) to 1.8 nm (MCM-B) indicating progressive functionalization inside the pores (Figure 4b). Boronic acid groups are known to bind Alizarin red S (ARS) and turn on its fluorescence.^[15] The amount of active boronic acid groups available for binding to cis diols was estimated to be ~ 0.5 mmol/g by carrying out a binding titration using ARS (Figure 5). The enhancement in fluorescence intensity observed upon successive additions (2 mg) of MCM-B to the ARS solution indicates binding of ARS to boronic acid groups since only ARS bound to boronic acid groups is fluorescent (Figure 6). The quenching of ARS fluorescence on displacement by glucose, allowed us to follow the binding of boronic acid groups in MCM-B with glucose through emission spectra (Figure 7). A significant decrease in fluorescence intensity was observed even at a concentration of 10 mM glucose.

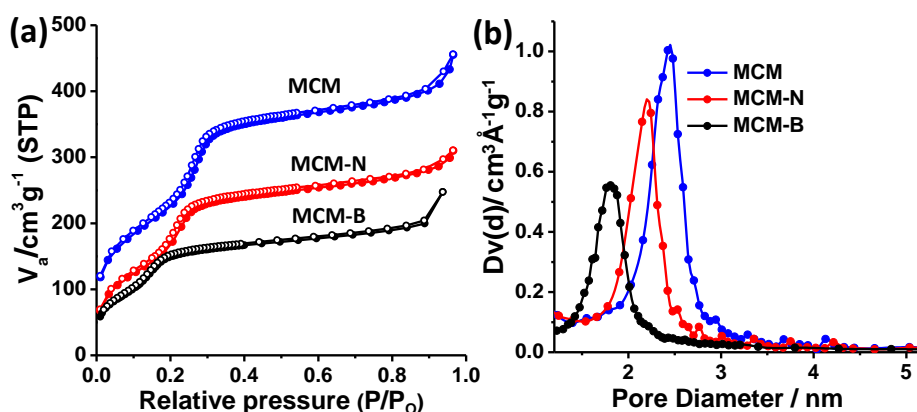


Figure 4. (a) Nitrogen adsorption-desorption isotherms and (b) Barrett-Joyner-Halenda pore size distribution curves of MCM, MCM-N and MCM-B.

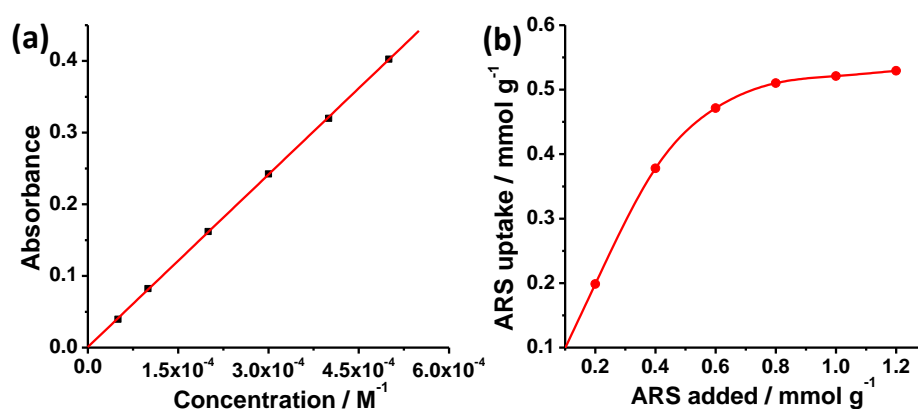


Figure 5. (a) Calibration curve for Alizarin Red S (ARS) in the concentration range $(1 - 5) \times 10^{-4}$ M (pH 7.4, HEPES, 10 mM) to be used for quantification of ARS bound to MCM-B. (b) Binding curve showing the uptake of ARS by MCM-B (pH 7.4, 10 mM HEPES).

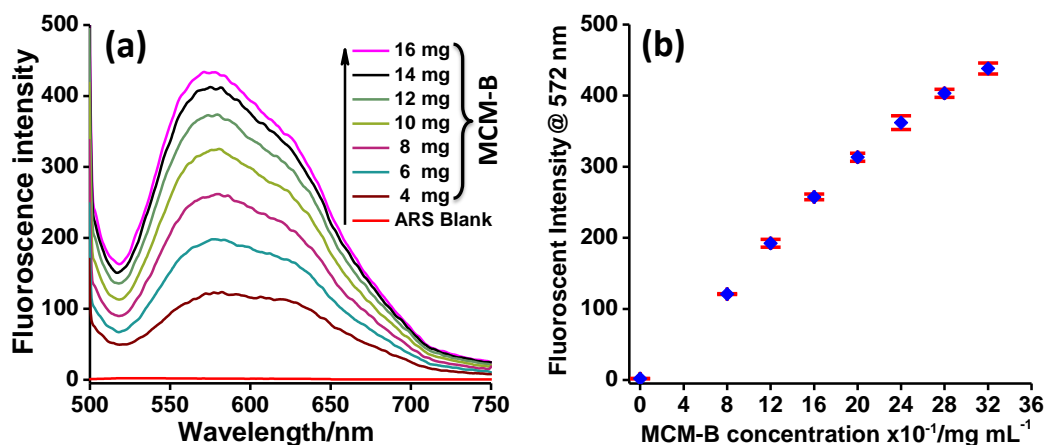


Figure 6. Emission spectra of a solution of ARS ($1 \times 10^{-4}M$, excitation wavelength-468 nm) on addition of MCM-B in increments of 2 mg. (b) Fluorescent intensity at 572 nm plotted against weight of MCM-B added per ml of ARS solution, shows gradual increase with addition of MCM-B. The error bars have been calculated from three replicates.

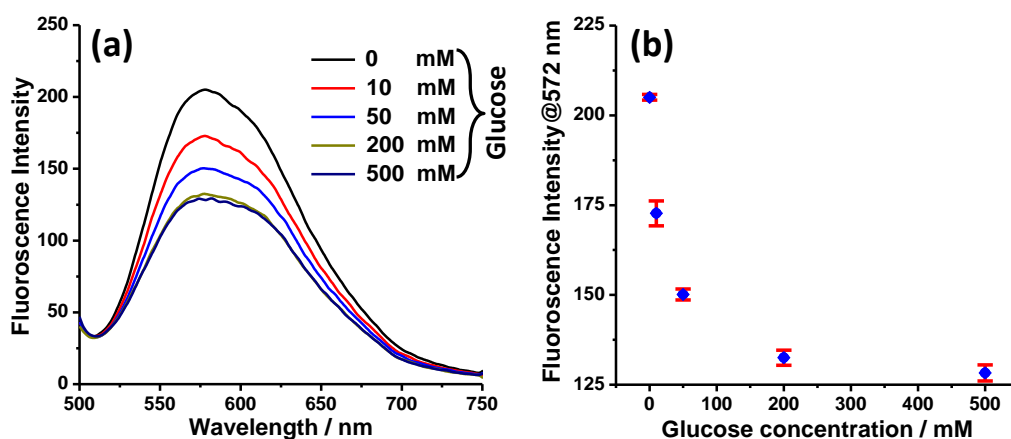


Figure 7. (a) Emission spectra of ARS bound MCM-B with increasing concentration of glucose show decrease in fluorescence indicating competitive displacement of ARS by glucose. (b) The plot of fluorescent intensity against glucose concentration reveals competitive displacement in the concentration range of 0-100 mM. The error bars have been calculated from three replicates.

Zeta potential measurements were used to probe the charge on the surface. The variation of zeta potential was monitored with change in pH in the range of 3-9. Aminopropyl functionalized MCM-N exhibited a zeta potential of +45 mV at pH 3 which decreased to +5 mV at pH 9 without showing any sign of charge reversal (Figure 8). It should be noted that even at pH 3, only less than 50 % of the amine groups in MCM-N would be protonated due to charge crowding.^[16] On the other hand, MCM-B which has both amine as well as phenylboronic acid groups, shows charge reversal on increasing pH from 3 to 9 (Figure 8). At

pH 3, MCM-B is positively charged with +47 mV similar to that of MCM-N which can be understood considering the fact that still a significant amount of amine groups are available for protonation in MCM-B. The zeta potential of MCM-B shows a slow but gradual decrease upto pH 6, beyond which there is a steep drop in the surface charge. The surface charge drops to zero at around pH 7.6 and goes to the negative side as the pH is increased. This suggests that the pK_a of the boronic acid moiety in carboxyphenylboronic acid^[17] ($pK_a = 8.0$) is shifted to lower value in presence of amine groups.^[18] As the pH is increased further the zeta potential goes on decreasing due to the increased formation of negatively charged boronate ions and neutralization of amines (Scheme 1 and Figure 10). The zeta potential decreases to about -30 mV at around pH 9.

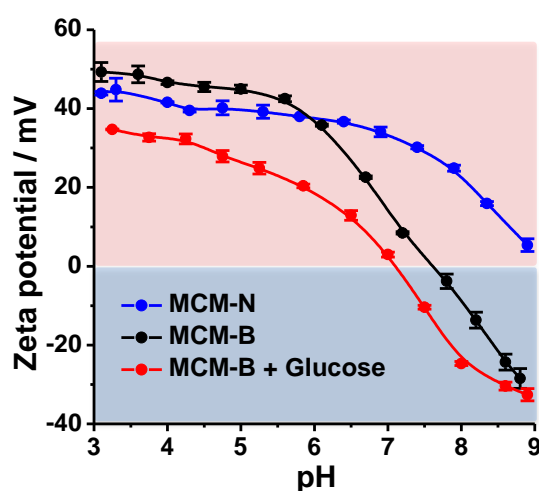


Figure 8. Variation of zeta potential with change in pH for MCM-N, MCM-B and MCM-B bound to glucose (100 mM).

The isoelectric point of MCM-B falls at pH 7.6, whereas for MCM-B bound to glucose (MCM-B-glu) it is at pH 7.2 (Figure 8). At pH 7.4, MCM-B is still positively charged and MCM-B-glu is negatively charged. So, the binding of glucose induces charge reversal of the system at lower pH (Figure 9a). This can be understood by considering the fact that the binding of glucose to boronic acid (boronic acid ester) reduces its pK_a due to which it forms its conjugate base (tetrahedral boronate ester) which is negatively charged thereby causing charge reversal (Figure 10). The reversal of charge at pH 7.4 by glucose was further verified by studying the desorption behaviour of a negatively charged chromophore, brilliant yellow (BY, Figure 9b) with increasing concentration of glucose (Figure 9c). It was observed that desorption of BY showed a concentration dependent response. This was further illustrated by monitoring desorption profile of BY with time at different glucose levels at pH 7.4 (Figure 9d). The desorption profile in the absence of glucose showed marginal release with time in comparison to the desorption in the presence of glucose.

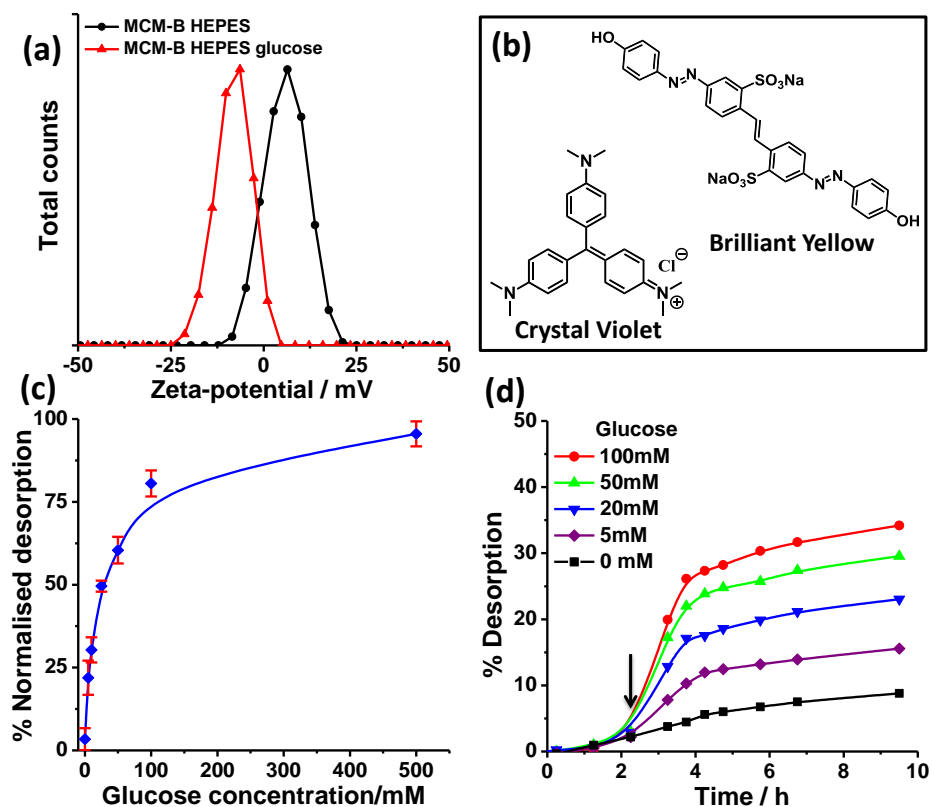


Figure 9. (a) Zeta potential distribution curves of MCM-B and MCM-B with glucose (in HEPES buffer, pH 7.4). (b) Molecular structures of crystal violet and brilliant yellow. (c) Desorption of brilliant yellow (negatively charged) at pH 7.4 showing concentration dependent response to glucose. (d) Desorption profile of brilliant yellow on addition of the glucose at pH 7.4 (HEPES buffer) showing quantitative response to the concentration of glucose (Arrow marks the time of addition of glucose).

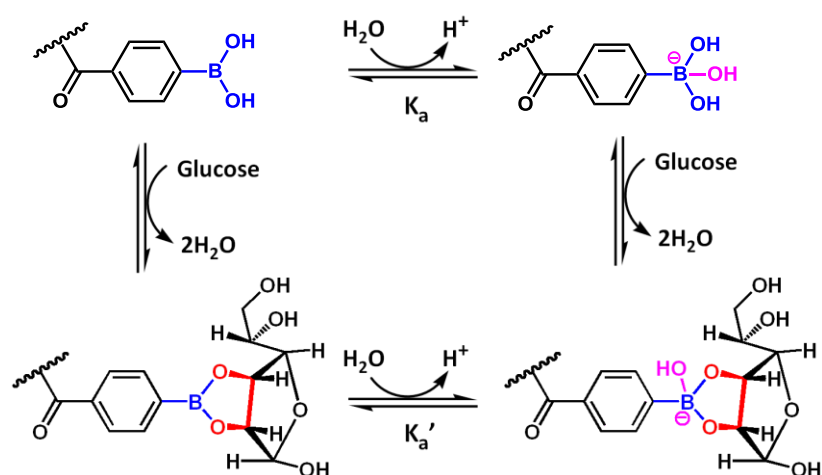


Figure 10. The equilibrium relationships between phenylboronic acid and its glucose ester. Note: $pK_a = 8.0$ and $pK'_a < pK_a$.

The step-like desorption profile for incremental doses of glucose clearly shows the versatility of the system to respond to sequential addition of glucose (Figure 11a). The crystal violet (positively charged chromophore) loaded MCM-B showed no desorption on addition of glucose in contrast to the BY loaded MCM-B which showed a strong desorption response confirming the reversal of charge induced by binding of glucose (Figure 11b).

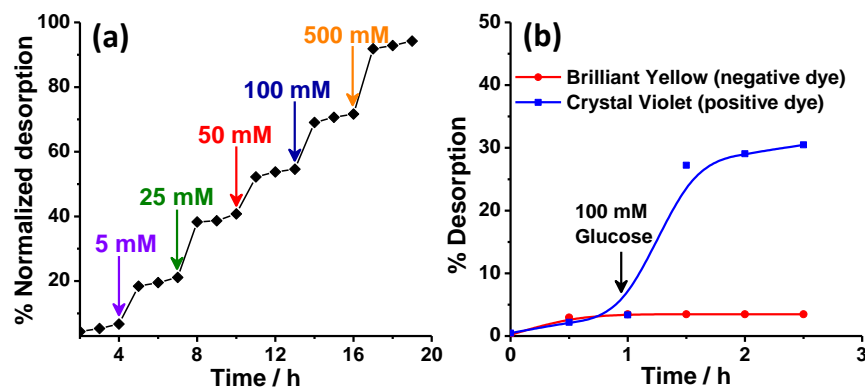


Figure 11. (a) Desorption of brilliant yellow (negatively charged) at pH 7.4 showing step wise response on increasing glucose concentration at fixed intervals. (b) Desorption profile of a positively and negatively charged chromophore on addition of glucose (100 mM) at pH 7.4.

To further prove the glucose induced charge-reversal we studied the desorption of another negatively charged dye, 1,3,6,8-pyrenetetrasulphonic acid, which showed a similar desorption profile as BY (Figure 12). The interference by fructose and mannose was studied to check the selectivity of our system. At their maximum concentration in blood (0.1 mM), no significant interference was found (Figure 13a) but at concentrations equal to that of glucose in blood, fructose exhibited a 40% greater response than glucose while mannose showed similar response as glucose (Figure 13b).

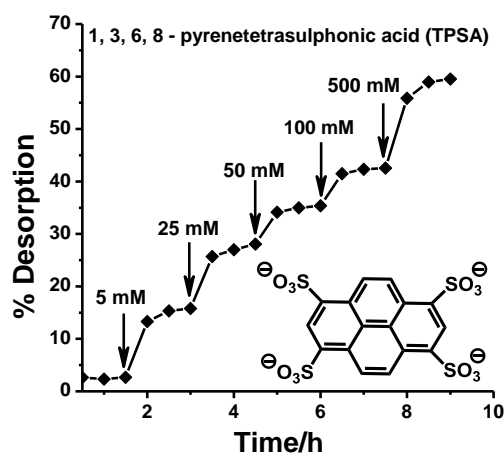


Figure 12. Desorption profile of negatively charged TPSA dye from MCM-B with increasing glucose concentration (pH 7.4) showing the same trend as the desorption profile of BY.

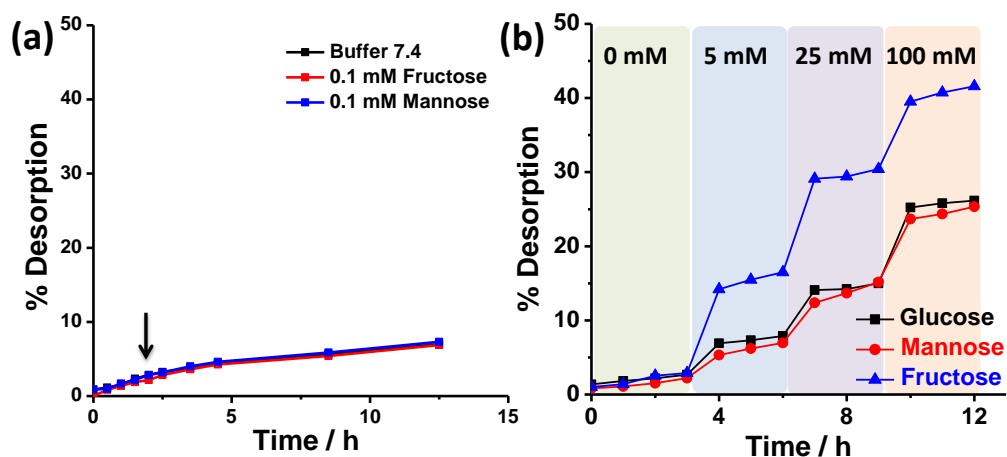


Figure 13. Desorption profile of brilliant yellow (HEPES, pH 7.4) (a) in the presence of 0.1 mM of mannose and fructose showing no significant interference (The arrow marks the point of addition of saccharides) and (b) with increasing concentration of saccharides.

The pH induced charge reversal was studied by monitoring the desorption behavior of BY adsorbed onto MCM-B at pH 4 (Figure 14a). As the pH was gradually increased, we see that there is not much release of BY till pH 7 due to the strong electrostatic interaction of the negatively charged dye with the highly positively charged MCM-B. Moreover, BY bearing two negative charges has strong electrostatic interactions with MCM-B giving a weak desorption response of 7% at pH 7. At pH 8 and 9, the desorption was 20% and 48%, respectively. From the zeta potential data, it can be seen that MCM-B is negatively charged above pH 7.6, so it is to be expected that desorption should be complete at pH 8. Instead, the desorption at pH 9 (48%) is greater than at pH 8 (20%). We can reconcile to this fact by taking into account that MCM-B is a system with heterogeneous functionalization and zeta potential gives us an idea of the overall charge of the system but not its spatial distribution. From the zeta potential data of MCM-N at pH 8, it can be understood that the amine groups would still be protonated in MCM-B. Hence even though the surface as a whole has gained a negative charge, the presence of localized positive charges on the amine groups enable the negatively charged chromophore to bind to the surface. On further increasing the pH to 9, there is an increased desorption of brilliant yellow due to neutralization of amines and negative charging of boronic acid groups. To further verify the pH induced charge reversal, the desorption of positively charged chromophore (crystal violet - CV) was also monitored with respect to pH (Figure 14b). The desorption profile shows maximum response in the pH range 6 to 7. The presence of amine groups adjacent to boronic acid is known to shift its pK_a to smaller values^[18] which in turn increases the desorption response at pH range 6 to 7. The desorption is not complete even after reaching pH 4 where 65% of CV is still adsorbed onto MCM-B. It should be noted that unlike

BY, CV is monopositive and the positive charge is highly delocalized which in turn weakens the electrostatic repulsions.

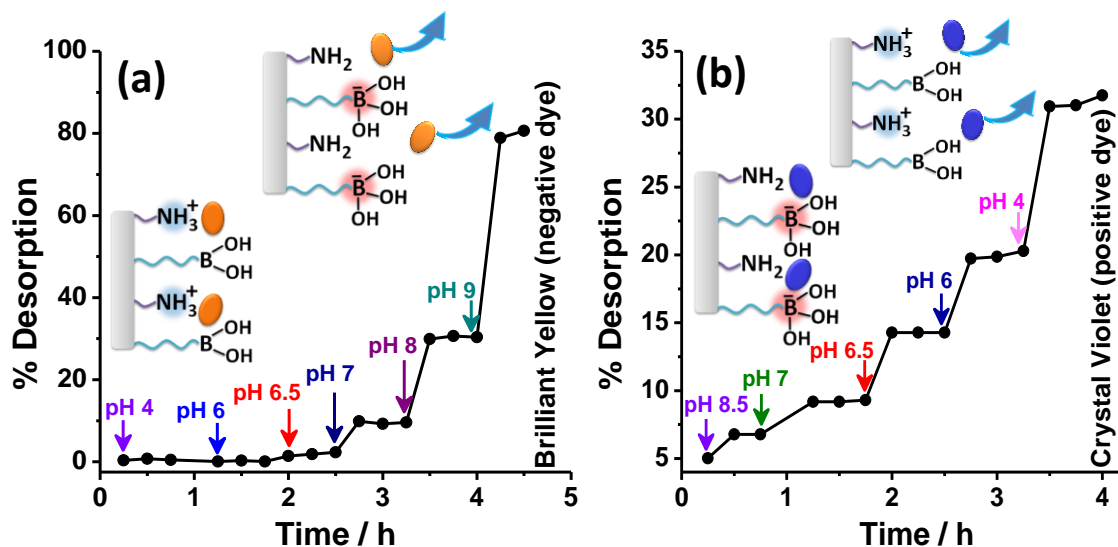


Figure 14. Step wise desorption profiles of (a) negatively charged brilliant yellow with increasing pH and (b) positively charged crystal violet dye with decreasing pH from MCM-B.

4.3.6. Conclusions

In conclusion, we have shown a simple system capable of charge reversal showing response to dual stimuli, pH as well as glucose. The charge reversal was carefully studied using zeta potential measurements as well as desorption of charged chromophores to reveal the heterogeneity in surface charge. The uneven distribution of boronic acid groups on the silica surface gave rise to a range of binding sites for glucose allowing for multiple levels of response.

4.3.7. References

- [1] a) L.-C. Hu, Y. Yonamine, S.-H. Lee, W. E. van der Veer, K. J. Shea, *J. Am. Chem. Soc.* **2012**, *134*, 11072-11075; b) J. Baram, E. Shirman, N. Ben-Shitrit, A. Ustinov, H. Weissman, I. Pinkas, S. G. Wolf, B. Rytchinski, *J. Am. Chem. Soc.* **2008**, *130*, 14966-14967.
- [2] a) M. Yasui, A. Hazama, T.-H. Kwon, S. Nielsen, W. B. Guggino, P. Agre, *Nature (London)* **1999**, *402*, 184-187; b) M. Tagliazucchi, O. Azzaroni, I. Szleifer, *J. Am. Chem. Soc.* **2010**, *132*, 12404-12411; c) B. Yameen, M. Ali, R. Neumann, W. Ensinger, W. Knoll, O. Azzaroni, *J. Am. Chem. Soc.* **2009**, *131*, 2070-2071.
- [3] C. C. A. Ng, A. Magenau, S. H. Ngalm, S. Ciampi, M. Chockalingham, J. B. Harper, K. Gaus, J. J. Gooding, *Angew. Chem. Int. Ed.* **2012**, *51*, 7706-7710.

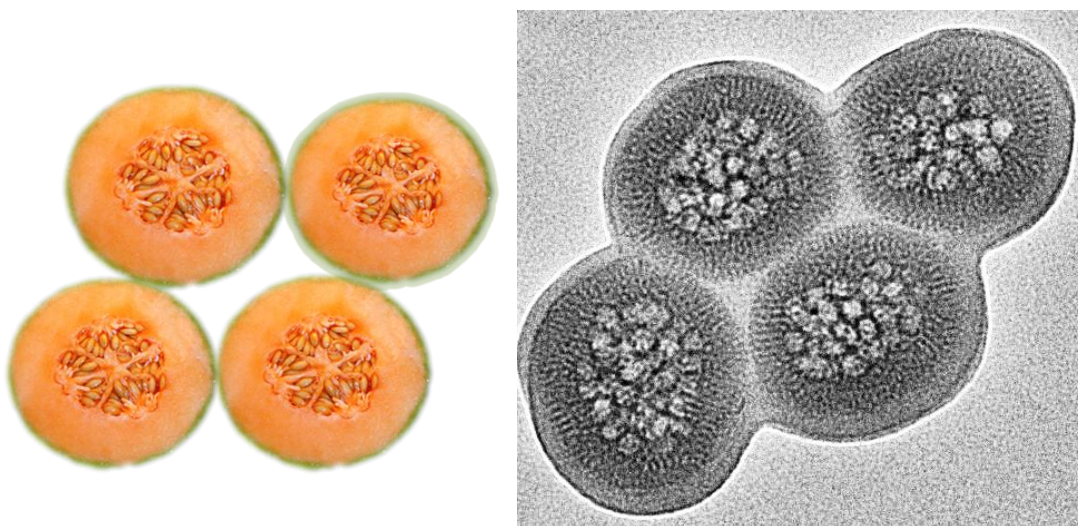
- [4] a) C. M. LaManna, H. Lusic, M. Camplo, T. J. McIntosh, P. Barthélémy, M. W. Grinstaff, *Acc. Chem. Res.* **2012**, *45*, 1026-1038; b) L. Han, J. Zhao, X. Zhang, W. Cao, X. Hu, G. Zou, X. Duan, X.-J. Liang, *ACS Nano* **2012**, *6*, 7340-7351; c) P. Xu, E. A. Van Kirk, Y. Zhan, W. J. Murdoch, M. Radosz, Y. Shen, *Angew. Chem. Int. Ed.* **2007**, *46*, 4999-5002.
- [5] E. Katz, V. Bocharova, M. Privman, *J. Mater. Chem.* **2012**, *22*, 8171-8178.
- [6] a) A. Pranzetti, S. Mieszkin, P. Iqbal, F. J. Rawson, M. E. Callow, J. A. Callow, P. Koelsch, J. A. Preece, P. M. Mendes, *Adv. Mater.* **2013**, *25*, 2181-2185; b) A. F. Radovic-Moreno, T. K. Lu, V. A. Puscasu, C. J. Yoon, R. Langer, O. C. Farokhzad, *ACS Nano* **2012**, *6*, 4279-4287.
- [7] J. R. Matthews, D. Tuncel, R. M. J. Jacobs, C. D. Bain, H. L. Anderson, *J. Am. Chem. Soc.* **2003**, *125*, 6428-6433.
- [8] G. Coué, J. F. J. Engbersen, *J. Controlled Release* **2010**, *148*, e9-e11.
- [9] A. Koçer, M. Walko, W. Meijberg, B. L. Feringa, *Science* **2005**, *309*, 755-758.
- [10] L. Wen, Q. Liu, J. Ma, Y. Tian, C. Li, Z. Bo, L. Jiang, *Adv. Mater.* **2012**, *24*, 6193-6198.
- [11] a) T. Hoare, R. Pelton, *Biomacromolecules* **2008**, *9*, 733-740; b) C. Ancla, V. Lapeyre, I. Gosse, B. Catargi, V. Ravaine, *Langmuir* **2011**, *27*, 12693-12701.
- [12] G. Springsteen, B. Wang, *Tetrahedron* **2002**, *58*, 5291-5300.
- [13] S. Huh, J. W. Wiench, J.-C. Yoo, M. Pruski, V. S. Y. Lin, *Chem. Mater.* **2003**, *15*, 4247-4256.
- [14] S.-W. Sun, Y.-C. Lin, Y.-M. Weng, M.-J. Chen, *Journal of Food Composition and Analysis* **2006**, *19*, 112-117.
- [15] G. Springsteen, B. Wang, *Chem. Commun.* **2001**, 1608-1609.
- [16] A. Walcarius, M. Etienne, B. Lebeau, *Chem. Mater.* **2003**, *15*, 2161-2173.
- [17] J. Yan, G. Springsteen, S. Deeter, B. Wang, *Tetrahedron* **2004**, *60*, 11205-11209.
- [18] a) C. J. Ward, P. Patel, P. R. Ashton, T. D. James, *Chem. Commun.* **2000**, 229-230; b) L. Ren, Z. Liu, Y. Liu, P. Dou, H.-Y. Chen, *Angew. Chem. Int. Ed.* **2009**, *48*, 6704-6707.

Chapter-5

Synthesis of Mesocellular Hollow Spheres using Emulsion Templates with a Volatile Component

Summary

Mesocellular hollow spheres have been synthesized using emulsion templates with a volatile solvent. Use of both octadecene and chloroform (volatile component) gave mesocellular hollow sphere whereas use of octadecene alone gave hollow spheres with no hierarchical structure. In order to enrich the functionality of the synthesized mesocellular hollow spheres, oil soluble magnetite nanoparticles (oleic acid capped) were also incorporated along with the emulsion templates. The obtained mesocellular spheres with magnetite nanoparticles entrapped would find applications in both drug delivery as well as in diagnosis (Magnetic Resonance Imaging). The described strategy can also be applied to incorporate quantum dots and gold nanoparticles to create a multifunctional composite.



Manuscript based on this work is under preparation.

5.1. Introduction

Hollow mesoporous silica (HMS) spheres have attracted significant attention in the last few decades by virtue of their large cavity, low density, high pore volume and permeable mesoporous walls. For example, the large void space/cavity in these structures has been used to load drug molecules.^[1] To further enable their use as smart drug delivery systems, Stoddart et. al. have anchored stimuli responsive pore gates^[2] at the pore openings to control drug release properties. Multifunctional composites can also be fabricated by incorporating magnetic nanoparticles^[3] (Magnetic Resonance Imaging-MRI), noble metal nanoparticles^[4] (catalysis) or quantum dots^[5] (Imaging) into the hollow cavity. Encapsulation of catalytic nanoparticles in hollow mesoporous silica shells can prevent growth and agglomeration of nanoparticles during catalytic reactions thereby increasing the cycle life of these catalysts.^[4a] In addition, a radial orientation of pores in the shell would enable fast diffusion of the reactants and products, thus making HMS an excellent platform for catalytic applications.

The HMS spheres have mainly been synthesized through sol-gel transcription method^[6] using templates wherein at least two steps are indispensable. Firstly, the template must be modified to encourage deposition of silica-surfactant assemblies onto the surface of the template. After the formation of the mesoporous silica shell the templates are eliminated to leave behind a hollow shell. Both hard and soft templates have been used for the synthesis of HMS spheres. The use of hard templates^[7] (silica/carbon/polymer spheres) has advantages of good monodispersity and faithful templating/replication. Nevertheless, the removal of the templates through thermal treatment or chemical etching is energy consuming and tedious. On the other hand, soft templates^[6b, 8] (emulsion, bubbles, bacteria, etc.) are relatively easy to remove but result in poor morphology and monodispersity due to the deformability of the template.

More recently, Yadong Yin et al. have reported the synthesis of mesoporous silica spheres in a single step from silica spheres which they have termed “surface protected etching”.^[9] In this strategy, a protecting layer of polyvinylpyrrolidone is adsorbed onto the surface of silica spheres and then the interior of the silica spheres is selectively or preferentially etched. The absence of pore controlling agents in this strategy leads to formation of disordered pores with a broad pore size distribution. To overcome this disadvantage, Nanfeng Zheng et al. used a cationic surfactant to etch the silica spheres wherein the silica species released by etching reorganize along with the surfactants to form a mesoporous silica shell.^[10]

Partial etching of the template (silica spheres) after the formation of the mesoporous silica shell has been used to fabricate structures with yolk-shell hierarchical morphology.^[11]

Use of dual surfactant approach can also give hierarchically structured mesoporous silica capable of exhibiting a three stage drug release profile.^[12]

5.2. Scope of the present investigation

In the present study, mesocellular hollow spheres have been synthesized using emulsion templates with a volatile component. In this strategy, an emulsion is formed by dispersing chloroform and octadecene in water using a cationic surfactant. The size of the emulsion droplets was allowed to reduce by evaporation of chloroform followed by silica condensation was carried out to give hierarchically structured mesocellular hollow structures. Magnetite nanoparticles could also be integrated into the structure by using oil soluble magnetite nanoparticles (oleic acid capped) in the emulsifying step. This would enable their use in both drug delivery as well as in diagnosis (Magnetic Resonance Imaging). The described strategy can also be applied to incorporate quantum dots and gold nanoparticles to create a multifunctional composite.

5.3. Experimental section

Preparation of emulsion templates

With octadecene and chloroform: 100 μ L of octadecene (OD) and 1.9 mL of chloroform were sonicated in 20 mL of water containing 0.4 g of cetyltrimethylammonium bromide (CTAB) for 5 minutes to form an opaque white microemulsion. The emulsion obtained was stirred at room temperature for 20 minutes before raising the temperature to 60 °C for about 5 minutes to complete the evaporation of chloroform which caused a change in the appearance from opaque white to translucent. The excess CTAB was crystallised out of the solution by reducing the temperature to 4 °C. This process was repeated for three times complete removal of excess CTAB.

Control experiments were carried out where the samples were synthesized using emulsions made from either octadecene or chloroform.

Synthesis of mesocellular hollow spheres (MHS)

14.3 g of ammonia solution (27%) and 0.025 g of CTAB were taken along with 27 mL of water in a round bottom flask and kept stirring for 10 minutes. 4 mL of the emulsion templates was added and the temperature was slowly raised to 85 °C with stirring. After the temperature stabilised, 0.3 mL of 1,2-bis(triethoxysilyl)ethane was added dropwise to the reaction mixture and stirring was continued for two hours. The as-synthesised mesocellular hollow spheres were washed with water and ethanol to remove to emulsion templates.

Synthesis of Fe₃O₄@MHS

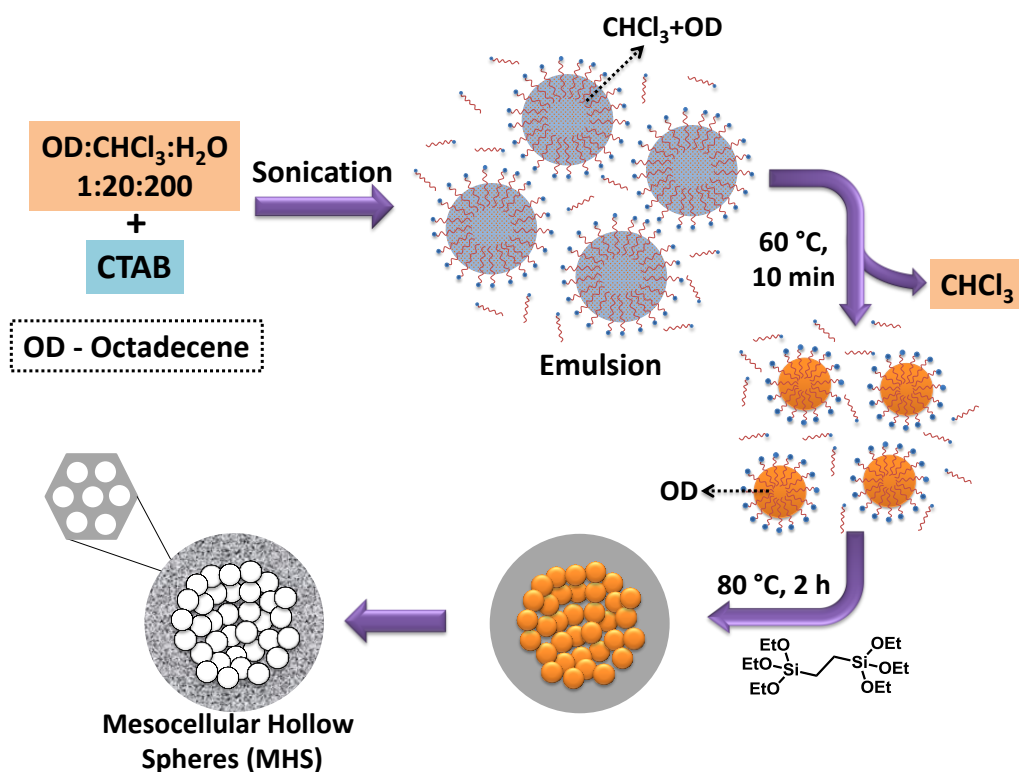
Oleic acid capped Fe₃O₄ nanoparticles (synthesized using a reported procedure^[13]) were taken in 2 mL of chloroform and sonicated in 20 mL of water containing 0.4 g of CTAB. This was then stirred for 10-15 minutes and the temperature was raised to 60 °C for 10 minutes to volatilize chloroform and complete the solubilization of Fe₃O₄ nanoparticles in water. The excess CTAB was crystallized out by reducing the temperature to 4 °C. 1 mL of Fe₃O₄ nanoparticles dispersion was mixed with the same volume of emulsion templates obtained from octadecene and chloroform. The temperature was raised to 85 °C and 0.3 mL of 1,2-bis(triethoxysilyl)ethane was added dropwise to the reaction mixture with stirring. After two hours, mesocellular hollow spheres formed were washed with water and ethanol to remove to emulsion templates.

5.4. Characterization

Please refer to the appendix for the instrumental details of FESEM, TEM, nitrogen sorption analysis and dynamic light scattering measurements.

5.5. Results and discussion

In this chapter, microemulsion templates were used to synthesize hollow mesoporous silica spheres with mesocellular interiors. Chloroform and octadecene were used to form the oil phase of the microemulsion in water using excess CTAB as the stabilizer (Scheme 1). The size of emulsion templates was reduced by evaporating the chloroform at 60 °C. Excess CTAB was then crystallized out of solution by reducing the temperature to 4 °C. This was essential to avoid independent nucleation of the mesoporous silica away from the emulsion templates. The as-synthesized emulsion was then used as a template to form hollow mesoporous organosilica spheres with mesocellular interiors using the sol-gel based transcription method. The FESEM image of the mesocellular hollow spheres (MHS) shows irregular shapes and sizes as expected from a soft templating strategy^[14] (Figure 1a). The TEM image shows uniformly sized, multiple hollow cavities enveloped by a mesoporous shell with radial mesochannels (Figure 1b).



Scheme 1. An illustration depicting the synthetic strategy of mesocellular hollow spheres using emulsion templates.

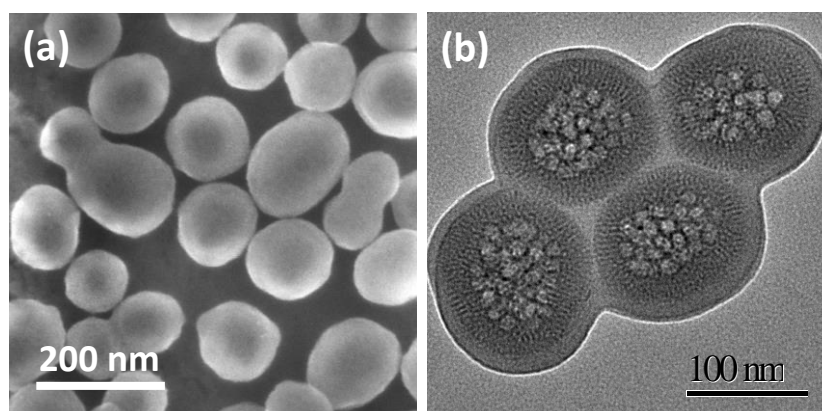


Figure 1. (a) FESEM and (b) TEM images of mesocellular hollow spheres.

To understand the mechanism of formation of MHS, dynamic light scattering (DLS) measurements were carried out to analyse the size of the emulsion templates before silica deposition. A mean droplet size of around 25-30 nm was obtained from the DLS data (Figure 2). This is quite close to the size obtained for the cavities from TEM, considering the fact that the size obtained from DLS is the hydrodynamic size which includes the surfactant layer stabilizing the droplets and the solvent molecules which move with the droplet. The condensation of silica around the emulsion droplets leads to their aggregation resulting in a mesocellular internal structure. The deposition of negatively charged silica species neutralises

the charge of CTAB stabilising the emulsion droplets thus allowing them to aggregate (Scheme 1). Further, as more hydrolyzed silica species formed in the reaction mixture, they self-assembled with the CTAB available in the solution to form radially oriented mesochannels.

Nitrogen adsorption-desorption isotherms (Figure 3a) recorded on MHS showed two inflections, with the first one at 0.3 P/P_0 corresponding to the radial mesopores templated by the CTAB and the second one at 0.8 P/P_0 corresponding to the cavities templated by the soft emulsion droplets. The calculated BJH (Barret-Joyner-Halenda) pore size distribution (Figure 3b) also showed two peaks at 3.1 nm (due to CTAB template) and 11 nm (due to cavities). The appearance of a second peak at 11 nm implies that the cavities are relatively monodisperse in size which is quite unusual to obtain in the absence of a secondary surfactant. Moreover, the isotherms show H2 type hysteresis according to the IUPAC system of nomenclature indicating percolation effects. This implies that the cavities are accessible through the radial mesochannels and can be used to load drug molecules for delivery.

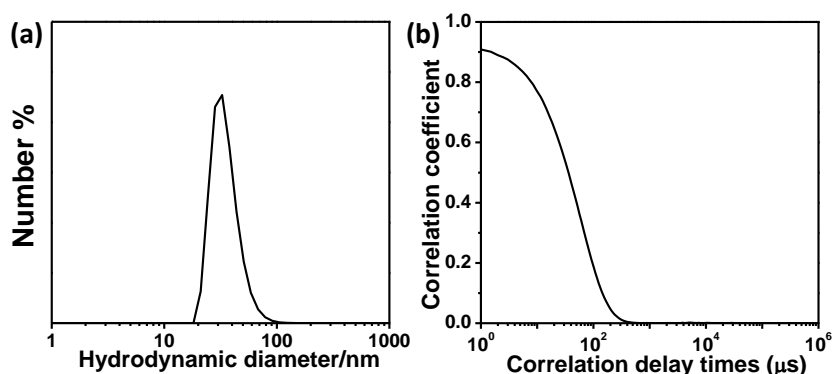


Figure 2. (a) Size distribution of the emulsion templates obtained using octadecene and chloroform. (b) The plot of correlation function used for calculation of the size distribution data.

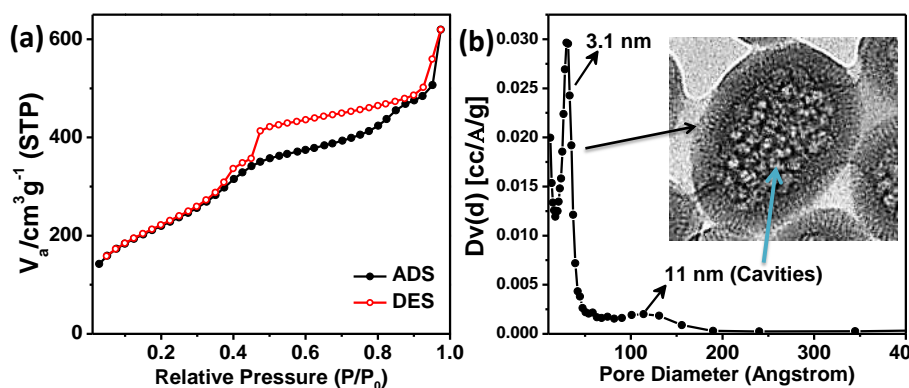


Figure 3. (a) Nitrogen adsorption-desorption isotherms of the mesocellular hollow spheres and (b) their calculated pore size distribution (Barret-Joyner-Halenda) showing two peaks at 3.1 nm and 11 nm for the radial mesochannels and cavities, respectively.

In order to understand the role of chloroform and octadecene in the formation of the mesocellular structure, control experiments were carried out where either only chloroform or octadecene was used to form the emulsion. When octadecene alone (no chloroform) was used, DLS measurements showed a larger mean droplet size of around 80 nm (Figure 4). The deposition of silica on these emulsion templates gave hollow mesoporous organosilica spheres with large cavities and radial mesochannels as seen in the TEM image given in figure 5a. It is also important to note from the FESEM image (Figure 5b) that the cavity sizes are not uniform whereas, in the MHS it was observed that the cavity sizes were fairly monodisperse but the size of the conglomerate of cavities was polydisperse. This is in line with the polydispersity index calculated from the DLS data which gave a higher value of 0.28 for the emulsion formed using octadecene alone in contrast to the smaller value of 0.18 for the emulsion formed from octadecene and chloroform. So, the use of chloroform helped in increasing the monodispersity of the emulsion templates and its removal during the thermal treatment step reduced the size of the emulsion droplets by two to three times. This can be rationalized by considering the fact that addition of chloroform (viscosity - 0.0005 Pa·s) reduces the viscosity of dispersed phase (viscosity of octadecene – 0.004 Pa·s) which lowers the viscosity ratio between the dispersed phase and the dispersion medium (viscosity of water – 0.0009 Pa·s) to below 1 which is known to increase the monodispersity and reduce the size of emulsion droplets.^[15] The nitrogen adsorption-desorption isotherms recorded on these hollow mesoporous spheres showed H2 type hysteresis indicating that the hollow cavity is accessible through the radial mesochannels (Figure 6a). On the other hand when only chloroform and no octadecene was used, mesoporous organosilica sphere with no hollow structure were formed (Figure 5c-d). The nitrogen adsorption-desorption isotherms did not show any significant hysteresis confirming the absence of accessible cavities (Figure 6b). This suggests that no emulsion templates are left after the heat treatment at 60 °C when only chloroform is used. When the emulsion was formed only with chloroform, the dispersed phase is completely removed and hence in the absence of the emulsion templates solid mesoporous organosilica spheres were formed.

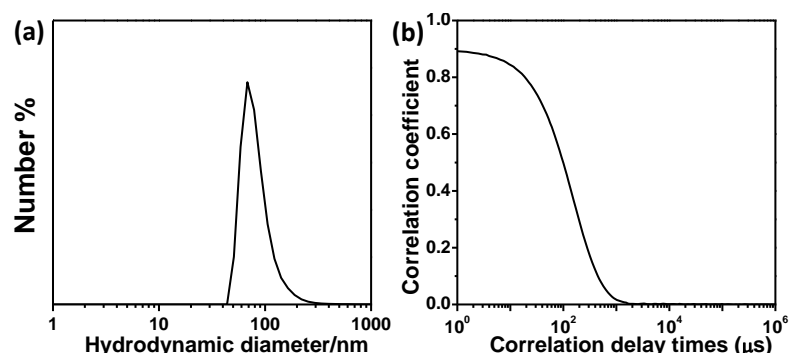


Figure 4. (a) Size distribution of the emulsion templates obtained using octadecene only. (b) The plot of correlation function used for calculation of the size distribution data.

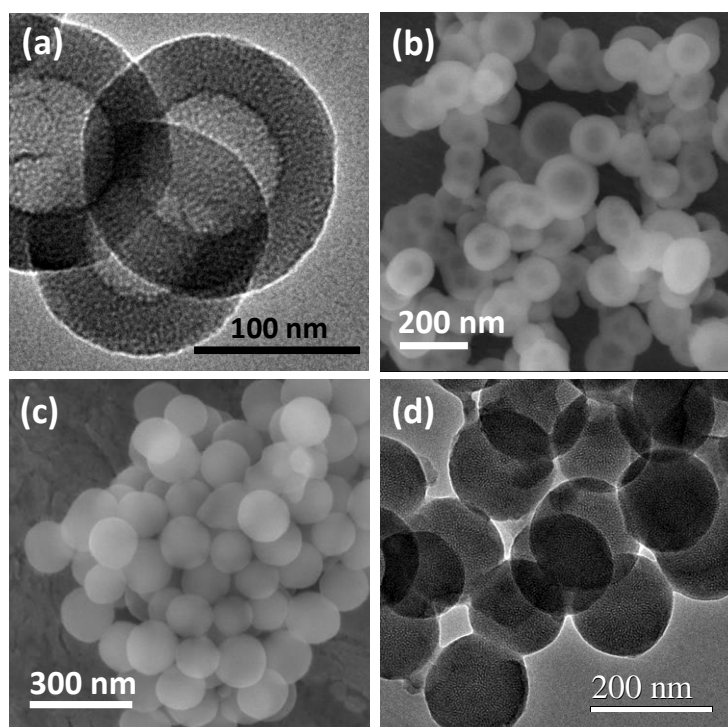


Figure 5. (a) TEM and (b) FESEM images of hollow mesoporous organosilica spheres formed using octadecene only to form the emulsion. (c) FESEM and (d) TEM images of solid mesoporous organosilica spheres formed when only chloroform was used.

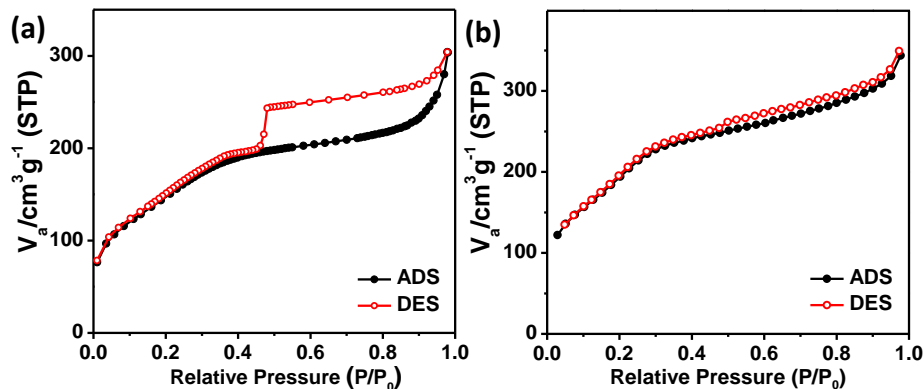


Figure 6. Nitrogen adsorption-desorption isotherms for the (a) hollow mesoporous organosilica spheres and (b) solid mesoporous organosilica spheres synthesized using only octadecene and chloroform, respectively.

The formation of MHS involves aggregation of the emulsion droplets followed by formation of mesoporous silica shell. To increase the functionality of the MHS, the emulsion templates were mixed with water soluble Fe_3O_4 nanoparticles prior to silica condensation to encapsulate Fe_3O_4 into the MHS. The TEM images of the Fe_3O_4 @MHS show presence of Fe_3O_4 nanoparticles in the core of MHS (Figure 7a-b). The incorporation of magnetite nanoparticles into the MHS would enable their use in MRI for diagnostic applications.

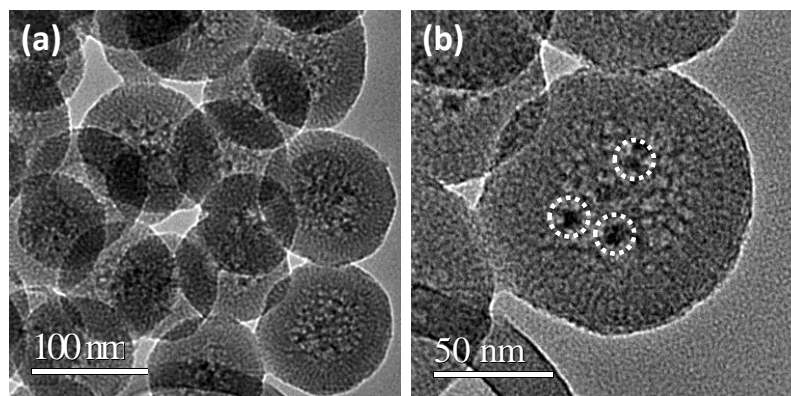


Figure 7. (a) Low magnification and (b) high magnification TEM images of mesocellular hollow spheres containing Fe_3O_4 nanoparticles at their core.

5.6. Conclusions

In conclusion, mesocellular hollow spheres have been synthesized using emulsion templates formed from chloroform and octadecene mixture. The role of chloroform and octadecene was studied and compared with blank experiments where only a single component was used to form the emulsion. Multifunctional composites incorporating Fe_3O_4 nanoparticles were synthesized by simply adding CTAB solubilised (oleic acid capped) nanoparticles to the emulsion prior to silica condensation. Similarly, gold nanoparticles and quantum dots can also be encapsulated to increase the functionality of the composites synthesized.

5.7. References

- [1] a) Z. Luo, X. Ding, Y. Hu, S. Wu, Y. Xiang, Y. Zeng, B. Zhang, H. Yan, H. Zhang, L. Zhu, J. Liu, J. Li, K. Cai, Y. Zhao, *ACS Nano* **2013**, *7*, 10271-10284; b) Y. Zhu, J. Shi, W. Shen, X. Dong, J. Feng, M. Ruan, Y. Li, *Angew. Chem. Int. Ed.* **2005**, *44*, 5083-5087; c) Y. Zhao, L.-N. Lin, Y. Lu, S.-F. Chen, L. Dong, S.-H. Yu, *Adv. Mater.* **2010**, *22*, 5255-5259; d) Y. Gao, Y. Chen, X. Ji, X. He, Q. Yin, Z. Zhang, J. Shi, Y. Li, *ACS Nano* **2011**, *5*, 9788-9798.
- [2] L. Du, S. Liao, H. A. Khatib, J. F. Stoddart, J. I. Zink, *J. Am. Chem. Soc.* **2009**, *131*, 15136-15142.
- [3] a) Y.-K. Hwang, J.-N. Choi, J.-H. Cho, H. Kwon, S. Huh, *Eur. J. Inorg. Chem.* **2012**, *2012*, 3379-3383; b) S. Sahu, N. Sinha, S. K. Bhutia, M. Majhi, S. Mohapatra, *Journal of Materials Chemistry B* **2014**, *2*, 3799-3808; c) M. Zhang, K. Fang, M. Lin, B. Hou,

- L. Zhong, Y. Zhu, W. Wei, Y. Sun, *The Journal of Physical Chemistry C* **2013**, *117*, 21529-21538; d) F. Lu, A. Popa, S. Zhou, J.-J. Zhu, A. C. S. Samia, *Chem. Commun.* **2013**, *49*, 11436-11438.
- [4] a) S. Wang, M. Zhang, W. Zhang, *ACS Catalysis* **2011**, *1*, 207-211; b) J. Niu, M. Liu, P. Wang, Y. Long, M. Xie, R. Li, J. Ma, *New J. Chem.* **2014**, *38*, 1471-1476.
- [5] J. Liu, S. B. Hartono, Y. G. Jin, Z. Li, G. Q. Lu, S. Z. Qiao, *J. Mater. Chem.* **2010**, *20*, 4595-4601.
- [6] a) B. Li, Y. Chen, H. Zhao, X. Pei, L. Bi, K. Hanabusa, Y. Yang, *Chem. Commun.* **2008**, 6366-6368; b) S. Schacht, Q. Huo, I. G. Voigt-Martin, G. D. Stucky, F. Schuth, *Science (Washington, D. C.)* **1996**, *273*, 768-771.
- [7] a) W. Zhao, M. Lang, Y. Li, L. Li, J. Shi, *J. Mater. Chem.* **2009**, *19*, 2778-2783; b) G. Qi, Y. Wang, L. Estevez, A. K. Switzer, X. Duan, X. Yang, E. P. Giannelis, *Chem. Mater.* **2010**, *22*, 2693-2695; c) H. Blas, M. Save, P. Pasetto, C. Boissière, C. Sanchez, B. Charleux, *Langmuir* **2008**, *24*, 13132-13137.
- [8] J. Wang, Q. Xiao, H. Zhou, P. Sun, Z. Yuan, B. Li, D. Ding, A. C. Shi, T. Chen, *Adv. Mater.* **2006**, *18*, 3284-3288.
- [9] a) T. Zhang, J. Ge, Y. Hu, Q. Zhang, S. Aloni, Y. Yin, *Angew. Chem. Int. Ed.* **2008**, *47*, 5806-5811; b) Q. Zhang, T. Zhang, J. Ge, Y. Yin, *Nano Lett.* **2008**, *8*, 2867-2871.
- [10] X. Fang, C. Chen, Z. Liu, P. Liu, N. Zheng, *Nanoscale* **2011**, *3*, 1632-1639.
- [11] Y. Chen, H. Chen, L. Guo, Q. He, F. Chen, J. Zhou, J. Feng, J. Shi, *ACS Nano* **2009**, *4*, 529-539.
- [12] D. Niu, Z. Ma, Y. Li, J. Shi, *J. Am. Chem. Soc.* **2010**, *132*, 15144-15147.
- [13] T. Hyeon, *Chem. Commun.* **2003**, 927-934.
- [14] J. Hu, M. Chen, X. Fang, L. Wu, *Chem. Soc. Rev.* **2011**, *40*, 5472-5491.
- [15] C. Mabille, F. Leal-Calderon, J. Bibette, V. Schmitt, *Europhys. Lett.* **2003**, *61*, 708-714.

Conclusions and Future Outlook

The potential of supramolecular chemistry in pore engineering of mesoporous silica has been explored to modify the pore size, philicity and surface charge. Strong charge-transfer interactions between viologen and various derivatised donors were exploited to enable performance on par with covalent strategies while retaining the advantages of a modular reversible approach.

In chapter 4.2, weak charge-transfer interactions were aided by hydrophobic interactions to enable charge-reversal. It would be a worthwhile attempt to try to attain charge reversal using hydrophobic interactions alone as it would make the design much more simpler and cost effective. Hydrophobic interactions are very effective in creating very strong assemblies especially in aqueous media. The nanochannels can be functionalized with alkyl chains and by using positively and negatively charged surfactants it would be possible to modify the surface charges to induce electrostatic gating of ion transport.

The sensitivity of the ion transport to the surface charge can be used as a tool to probe the nanoconfinement induced perturbation of acid-base equilibria or dissociation equilibria. Various interesting phenomena like cooperative electrostatic adsorption can also be studied.

Comment on the nature of interaction between viologen and pyranine:

Pyranine has three sulfonate groups attached to the pyrene aromatic core which makes it electron deficient. This would reduce the strength of charge-transfer interactions between pyranine and viologen (electron acceptor). Nevertheless, charge-transfer interactions between pyranine and viologen have been reported in literature^[1] to be able to form one dimensional assemblies with a fairly large association constant (10^4 M^{-1}). The extent of contribution of charge transfer interactions in the overall binding has also been studied. It was found that 25% of the Gibbs free energy of binding is due to charge-transfer interactions while a major 75% is contributed by coulombic forces.^[2] It should be noted that the binding strength of SBA-V was much stronger than the solution state analogue possibly due to the hydrophobic environment provided by the iodopropyl groups which strengthens the charge-transfer interactions. This observation was already made in the thesis.

References:

1. de Borba, E. B.; Amaral, C. L. C.; Politi, M. J.; Villalobos, R.; Baptista, M. S. *Langmuir* **2000**, 16, 5900.
2. Wang, C.; Guo, Y.; Wang, Y.; Xu, H.; Wang, R.; Zhang, X. *Angew. Chem. Int. Ed.* **2009**, 48, 8962.

Appendix

Instrumentation and Techniques for characterization

Powder X-ray Diffraction (XRD) – Recorded with Bruker D8 Advance diffractometer using Cu K α radiation.

Dynamic light scattering and zeta potential measurements - were carried out using a NanoZS (Malvern, UK) employing a 532 nm laser at a back scattering angle of 173°.

Infrared spectroscopy- IR spectra were recorded using Bruker IFS 66v/S spectrometer. 1-2 mg of sample was mixed with 100 mg of dry KBr and pelletized for recording spectra. Dry KBr pellets were used to correct for background.

Diffuse Reflectance Infra-red Fourier Transform Spectroscopy (DRIFTS) – DRIFTS spectra were recorded on a Bruker IFS 66v/S spectrometer. Averaged data from 100 scans was used to improve signal to noise ratio.

UV-Vis absorption spectroscopy – Spectra were recorded on Perkin-Elmer Lambda 900 UV/VIS/NIR spectrometer.

Fluorescence spectroscopy – emission spectra were recorded on Perkin Elmer Ls 55 luminescence spectrometer. Emission spectra were recorded in front face geometry using a 1 mm cuvette.

Transmission Electron Microscopy (TEM) - Images obtained with a JEOL JEM 3010 operating at an accelerating voltage of 300 KV. Samples for TEM analysis are

prepared by dispersing the sample in ethanol/water and drying one drop of the dispersion on holey carbon Cu grid.

Field Emission Scanning Electron Microscopy (FESEM) - Images were obtained using a NOVA NANOSEM 600 (FEI, Netherlands). A drop of dispersions of the sample was dried over aluminium stub for imaging. For the mesoporous silica films imaging was carried out in low vacuum mode. Energy dispersive x-ray spectra (EDAX) were recorded on the same instrument.

Thermogravimetric Analysis (TGA) - was carried out on a Mettler-Toledo-TG-850 instrument. 5-10 mg of sample was loaded into a small alumina boat for the analysis.

Nitrogen adsorption-desorption analysis – was performed on a Autosorb-1C (Quantachrome corp.). The samples were outgassed at 80 °C for 12 h under high vacuum before analysis. The specific surface areas were calculated according to the BET method using the Quantachrome software (ASiQwin). Ultrahigh pure gases (99.9995%) were used for all experiments.

Water Sorption analyses - were performed on Belsorp Aqua 3 at 298 K (BEL, Japan).

Voltammetry – Cyclic voltammetry measurements were performed using Autolab PGSTAT101 with ITO slides coated with mesoporous silica films as working electrodes, platinum wire as counter electrode and aqueous Ag/AgCl as reference electrode.

Profilometry - was performed using a Wyko NT9100 Optical Profiling System (Bruker, USA).

CURRICULUM VITAE



B.V.V.S. Pavan kumar was born on April 11, 1987 in Visakhapatnam, Andhra Pradesh (India). He completed his B.Sc. (Chemistry Hons.) from Sri Sathya Sai University, Puttaparthi in 2007, where he continued to finish his M.Sc degree in Chemistry in 2009. Thereafter, he joined Jawaharlal Nehru Centre for Advanced Scientific Research as a Ph.D. student in 2009, under the guidance of Prof. M. Eswaramoorthy. His research work at Nanomaterials and Catalysis Laboratory focused on supramolecular and covalent strategies towards pore engineering in mesoporous silica.

List of Corrections/Modifications incorporated in the thesis

1. A brief note has been included in the thesis (after the Conclusions and Future Outlook) in accordance with the suggestion of referee 1.
2. On the page 56 (Figure 13), the label on the x-axis has been changed from “Charge-transfer” to “Charge-transfer + Electrostatic”.